Technische Universität München

Lehrstuhl für experimentelle Halbleiterphysik E24
Walter Schottky Institut

Electroosmotic Flow and Protein Trapping in Solid-State Nanopores

Matthias Firnkes

Vollständiger Abdruck der von der Fakultät für Physik der Technischen Universität München zur Erlangung des akademischen Grades eines

Doktors der Naturwissenschaften

genehmigten Dissertation.

Vorsitzender: Univ.-Prof. Dr. Martin Zacharias

Prüfer der Dissertation:

1. Univ.-Prof. Dr. Gerhard Abstreiter
2. Univ.-Prof. Dr. Friedrich Simmel

Die Dissertation wurde am 08.11.2012 bei der Technischen Universität München eingereicht und durch die Fakultät für Physik am 13.12.2012 angenommen.

1. Auflage Februar 2013

Titelbild:
Left: Schematic cut-open view of a nanopore containing a spherical particle. Electrophoretic and electroosmotic forces are acting on the particle simultaneously (bold arrows). Thin lines indicate the electroosmotic flow.
Right: Tilted TEM micrograph of conical Si3N4 nanopore, colored for better visibility. On the bottom, a current-time trace of proteasome translocations is shown.

Druck: Printy Digitaldruck, München (http://www.printy.de)

ISBN: 978-3-941650-59-6

Abstract

Protein sensing with solid-state nanopores bears great potential for future bio-analytic applications. Monitoring of the ionic current through a single nanopore over time permits to detect the passage of single proteins or other molecules, leaving a fingerprint in the current-time trace, from which information about the molecule under investigation may be derived. Many ideas for sensing applications came up in recent years, but still some fundamental questions about the forces acting during protein translocation need clarification.

In chapter 2 and 3 of this thesis, the fabrication of silicon nitride nanopores by means of electron beam lithography is presented, the measurement instrumentation is explained and the basic theory necessary for the following experimental chapters is introduced.

In chapter 4, we report on the influence of the electroosmotic flow on protein translocation. We determine the zeta potential of a model protein (avidin) and a silicon nitride nanopore for different pH values. The measurements reveal that electroosmotic flow can enhance or even dominate protein transport over the electrophoretic motion. The resulting translocation direction can be predicted according to the difference between protein and pore zeta potential. Besides electrophoretically or electroosmotically driven transport, we report on a third mechanism when electrophoresis and electroosmosis cancel each other out. In this case, diffusion of proteins through the pore is observed irrespective of the applied potential.

Chapter 5 deals with experiments on a proteolytically active protein complex, the 20S proteasome from *Thermoplasma acidophilum*. First, we show that translocations of the protein through a conical nanopore are characterized by step-like current blockades. This blockade signature can be related to transient adsorption at different positions inside the nanopore and depends on pore size as well as on the applied potential.
In the second part of this chapter, we present trapping of single proteasome molecules in a pit-pore device. This device is fabricated in a two-step process and comprises a conical pit, fabricated by e-beam lithography, and a smaller pore, fabricated by TEM milling. A single molecule may now enter the conical part, but is hindered from translocation by the small pore. Proteasome molecules can be trapped and released reversibly in this device. If a single molecule is trapped, the measured ionic current is sensitive on the occupation state of the proteasome. Experiments at room temperature show that the current is blocked further after the addition of peptide Suc-LLVY-AMC. This strongly suggests incorporation of peptide in the proteasome for degradation.

The last chapter deals with a possibility to block a nanopore for a certain amount of time without applying an external voltage. Therefore, we conjugate nanoparticles with λ-DNA. Under the influence of an external electric field, the DNA is pulled through the pore but the attached nanoparticle stops the motion and blocks the pore. The external potential is now switched off and the nanoparticle pulls the DNA through the pore by thermal motion. Despite a low yield in particle–DNA conjugation, we observe blockade times of 1–2 s in pores of $\sim$15 nm diameter. In contrast, nanoparticles without DNA did not block the pore appreciably.

Zusammenfassung

Die Detektion von Proteinen mittels künstlicher Nanoporen bietet viele Möglichkeiten für zukünftige bioanalytische Anwendungen. Indem man den zeitlichen Verlauf des Ionenstroms durch eine einzelne Pore misst, kann man den Durchgang eines einzelnen Proteins (Translokation) sichtbar machen. Das Protein hinterlässt einen charakteristischen Fingerabdruck im Strom-Zeit Verlauf, anhand dessen man Informationen über das untersuchte Protein ableiten kann. In den letzten Jahren wurden viele Ideen für Sensoranwendungen vorgeschlagen und experimentell untersucht. Trotzdem sind noch immer einige fundamentale Fragen zu klären, was die physikalischen Kräfte, die in der Pore auf das Protein wirken, anbelangt.

In Kapitel 2 und 3 dieser Arbeit wird die Herstellung von Nanoporen in Siliziumnitrid mittels Elektronenstrahllithographie beschrieben, der experimentelle Versuchsaufbau erklärt und die notwendigen theoretischen Grundlagen behandelt, die zum Verständnis der nachfolgenden Kapitel wichtig sind.

In Kapitel 4 wird der Einfluss des elektroosmotischen Flusses auf die Protein-Translokation behandelt. Hierzu bestimmen wir zunächst das Zeta-Potential eines Modell-Proteins (Avidin) und der Nanopore bei verschiedenen pH-Werten der Elektrolytlösung. Unsere Messungen zeigen, dass der elektroosmotische Fluss den Proteintransport durch Elektrophorese verstärken und sogar dominieren kann. Die resultierende Translokationsrichtung in Bezug auf das elektrische Feld kann über den Unterschied der Zeta-Potentiale von Protein und Pore vorhergesagt werden. Außer dem Transport durch Elektrophorese oder Elektroosmose kann auch ein dritter Transportmechanismus auftreten, wenn sich Elektrophorese und Elektroosmose gegenseitig aufheben. Dann lässt sich Diffusion der Proteine durch die Nanopore beobachten, unabhängig von der Polarität des angelegten elektrischen Feldes.

In Kapitel 5 werden Experimente mit einem proteolytisch aktiven Protein, dem 20S Proteasom, vorgestellt und diskutiert. Im ersten Teil des Kapitels zeigen wir Translokationen durch eine konische Nanopore, die durch stufenförmige Stromblockaden charakterisiert sind. Diese Blockadesignatur kann durch transiente Proteinadsorption an verschiedenen Stellen der konischen Pore erklärt werden und ist abhängig von der Porengröße und dem angelegten elektrischen Feld.
Im zweiten Teil dieses Kapitels zeigen wir das Einfangen einzelner Proteasom Moleküle. Hierfür verwenden wir ein “pit-pore device”, das aus einer größeren, konischen Öffnung besteht, und einer daran anschließenden, kleineren Nanopore. Ein Proteasom Molekül kann nun den konischen Teil passieren, nicht jedoch die kleinere Nanopore, und ist deshalb in der Membran gefangen. In Abhängigkeit des elektrischen Feldes können Moleküle in dieser Porengeometrie reversibel gefangen und wieder freigelassen werden. Ist ein Molekül gefangen, so ist der Ionenstrom über die Membran empfindlich auf Änderungen des Proteasom Zustands. Experimente bei Raumtemperatur zeigen, dass die Stromblockade durch das Proteasom noch verstärkt wird, wenn man ein Peptid (Suc-LLVY-AMC) der Lösung zugibt. Diese Beobachtung legt den Schluss nahe, dass das Peptid vom Proteasom aufgenommen wurde, um zersetzt zu werden.

Im letzten Kapitel stellen wir eine Möglichkeit vor, wie man eine Nanopore für eine gewisse Zeit verschließen kann. Hierzu verwenden wir Nanopartikel-DNA Konjugate. Unter dem Einfluss eines elektrischen Feldes wird die DNA durch die Pore gezogen, allerdings nur solange bis das angehängte Nanopartikel die Pore blockiert. Schaltet man nun das elektrische Feld ab, benötigt das Partikel eine gewisse Zeit, um die DNA durch thermische Bewegung wieder zurück durch die Pore zu ziehen, und die Pore so wieder freizugeben. Obwohl bei der Herstellung nur wenige DNA-Nanopartikel Konjugate entstanden sind, konnten wir einige Blockaden mit einer Zeitdauer von 1–2 s beobachten, die auf das Vorhandensein eines Konjugates in der Pore schließen lassen. Nanopartikel ohne DNA haben die Pore dagegen nicht blockiert.

Contents

List of Figures

List of Tables

1. Introduction

Since the first demonstration of fabricating solid-state nanopores[61,108] and experiments to proof feasibility for molecule detection[60,61], nanopores have evolved into powerful devices to study and examine single molecules[15,46,91]. A solid-state nanopore is a defined hole with a diameter of several nanometers, situated on a thin membrane that divides two liquid compartments. The word "membrane" should not be confused with membranes in the common sense of e.g. fuel cells or cell membranes, where some sort of molecules or ions can pass. In the field of single molecule sensing, the membrane is an electrically and physically isolating barrier, which contains exactly one pore. The thickness of this membrane is typically between 20 and 50 nm. Two electrodes, placed on opposing sites of the membrane, generate an ionic current exclusively through the single nanopore. Information about the molecule under investigation (nucleic acids, proteins, small molecules, etc.) is inferred from fluctuations in the trans-pore ionic current which arise when the molecule transiently resides inside the pore while being pulled through the pore by the external electric force or by a flow of ionic solution. In the past, only the external electric field was considered as driving force. This scheme has worked particularly well for DNA; here, it is generally accepted that negatively charged DNA moves along the electric field through the pore towards the positively biased anode, which is defined as electrophoresis (EP)[20,53,116]. Recently, proteins and peptides have become an important focus of nanopore investigations[33,42,75,99,111]. Aside from their biological counterparts, solid-state nanopores are particularly appealing for this purpose, not only because of their mechanical robustness, but especially because of the possibility to engineer the pore with respect to its size, structure, and surface properties[25,45,118,121]. However, understanding the translocation behavior of proteins is a challenging task since proteins are only several nanometers in size and feature diverse chemical compositions and complex structures. Moreover, in contrast to strongly and homogeneously charged biopolymers like DNA, the charge of a protein may be distributed irregularly on its surface and can be positive, vanish, or be negative depending on the solution pH. Thus, a fundamental question in the context of electrically assisted translocation is: what drives proteins into, through, and out of nanopores?
Before the significance of electroosmosis (EO) on protein transport could be revealed by our experiments, "anomalous" translocation behavior through pores in silicon nitride (Si_3N_4) membranes has been reported[42] and was also observed by ourselves: positively (negatively) charged proteins crossed the pore towards the positively (negatively) charged electrode. Clearly, the direction of these translocations cannot be understood by electrophoresis, so we assumed that electroosmotic effects might be involved. Electroosmotic flow (EOF) occurs in micro- and nanochannels with charged sidewalls[95,106]: an electric field applied along the channel sets the electrical double layer (DL), which screens the surface charge, in motion. The DL drags the fluid along and as a result a net flow is created which, if the Debye length is much smaller than the channel width, features a plug-like velocity profile, i.e. constant radial flow velocity.

1. Introduction

EO effects have been observed before in µm to mm long nano-channels[12,55,115], in carbon nanotube membranes[73] and have been discussed in the context of ion current rectification and ion selectivity in nanopores[2,48,119]. Yusko et al. observed EO in long (275 nm), but not in short (10 nm) cylindrical Si_3N_4 nanopores of 30 nm diameter[132]. Wong and Muthukumar theoretically studied EO in nanopores to rationalize enhanced DNA capture rates[129] and Keyser et al. discussed the subject in the context of DNA optical tweezer experiments[53,116]. Changes in the binding of cyclodextrin to a biological pore, α-hemolysin, were attributed to EO flow[38].
In the first part of this thesis, we show that EO flow of sufficient magnitude can develop in extremely short (30 nm) and narrow (20 nm) solid-state channels, which actually facilitates protein transport. This experimental demonstration turned out to be helpful for many other researchers in the field to interpret their results in a coherent way, because electroosmotic effects have been discussed only as insignificant side effects so far.

Besides general questions about transport mechanisms in nanopores, many new and interesting applications of solid-state nanopore sensing are emerging lately. For these applications, nanopores are not only used as a simple detector for the presence of proteins, but as a support layer or trap for biological structures. Such hybrid structures enhance the application of simple nanopores to a new level of specificity and diversity. Mentionable examples in this context are: a combination of solid-state pores with lipid bilayers to enable translocation of sticky molecules[133], a combination of nanopore and nanowire field effect transistor to study DNA transport[131], forming of biomimetic nuclear pore complex structures (NPC) in solid-state pores[49,59], chemical modification of gold nanopores to detect and discriminate antibody classes[124], trapping of DNA-origami nanopore sturctures on solid-state nanopores to add chemical functionality via the origami-pore[9,125], incorporation of Gramicidin-A in polymer pores[7] and trapping of biological α-hemolysin pores in artificial silicon nitride (Si_3N_4) nanopores[40].
Motivated by the opportunities of hybrid structures, we had the idea to trap and investigate a large protein complex in a solid-state nanopore which is not reported in literature so far, namely the 20S proteasome. It is a large (700 kDa) protein complex, located in the nucleus and cytoplasm of each cell in large (10^5–10^6) numbers[89]. It is under steady and intense investigation because it regulates several important cell functions by degrading old, misfolded or excess proteins. Control over proteasome activity has potential applications[10] in anti-cancer therapy, is involved in neurodegeneration processes following an ischemic stroke, shows anti-inflammatory and antiviral effects and has potential to fight the tuberculosis bacterium, to name only a few. In contrast to membrane proteins like α-hemolysin, it is an active channel containing chemically active sites to cleave peptides. Because proteasome molecules cannot be integrated in lipid bilayers, solid-state nanopores open up unique options to study proteasome activity on a single molecule level. Therefore, it has to be trapped in a suitable pore geometry to monitor the ionic current through the proteasome channel.

In preliminary investigations on proteasome translocations, we observed an unreckoned blockade current signature. We explain this signature by protein adsorption, which is an intensely discussed topic in current publications on protein translocation experiments[34,77,83,100,111]. The timescale of most observed protein translocation events is 1–2 orders of magnitude larger than ex-

pected for free translocation, i.e. when only EO and EP forces act on the molecule. Other explanations under discussion for the unexpected long blockade duration are unfolding of molecules under the intense electric field inside the nanopore[111] but also the opposite effect, namely short blockades caused by unfolded proteins and long blockades caused by folded proteins, is observed[83,84]. However, protein unfolding can be tested by measuring the excluded volume[111], and can be excluded for many experiments[77,90,100]. The mobility of the particle may also be decreased inside the pore due to the short distance to the surface[1,65,78,88], but this effect is not expected to increase the translocation time by two orders of magnitude.
With our experiments, we show clearly that protein adsorption is observed for translocation of proteasome through conical nanopores. The observed conductance blockade height can be related to the position of transient adsorption inside the conical pore.

2. Fabrication & Instrumentation

Fabricating pores with nanometer dimensions is the key to a new world of single molecule experiments. When Wallace H. Coulter at the beginning of the 1950's developed the Coulter-Counter[22] as a tool to study small particles and blood cells with a size of about ten micrometers[37], he set the basic idea of single molecule experiments by monitoring the resistive pulses across an artificial pore. It took about 50 years to push the frontier of pore fabrication to sizes similar to single DNA strands[61,108]. Nowadays, solid-state nanopores are widely fabricated by sophisticated electron microscopes or focused ion beam systems.
There are numerous ways of fabricating pores of nanometer dimensions in a variety of solid-state materials. Milling by focused ion beam (FIB)[21,61,74], shrinking of larger pores by electron beam induced deposition (EBID)[24], ion beam induced deposition (IBID)[19], direct milling by a transmission electron microscope (TEM)[54,108,130] and electron beam lithography (EBL)[85] are common techniques to manufacture pores in silicon nitride (Si_3N_4) or silicon dioxide. A more elaborate method which needs a heavy ion accelerator is track etching of silicon nitride after irradiation with heavy ions[118,134], which was originally used to fabricate pores in polymer materials[4,32,101]. Furthermore, by electroless plating[69,102] or electron beam evaporation[126], metal coatings shrink initially larger pores and establish new possibilities for surface chemistry inside the pore[124]. In this thesis, only Si_3N_4 is used as membrane material with a thickness of 30–50 nm. Pores with diameters between 12 and 30 nm are formed by EBL or TEM milling. Smaller pores for proteasome trapping experiments are formed by a combination of EBL and TEM milling.

2.1. E-Beam lithography

The basis of our nanopore chip is a 200 µm thick silicon (100) wafer with low stress LPCVD silicon dioxide (10 nm) and silicon nitride (50 nm) on both sides, as shown in Fig. 2.1 a). The silicon dioxide acts only as an adhesion layer between the silicon and the Si_3N_4. The prerequisite for trans-pore ionic current measurements is a single pore in a Si_3N_4 membrane that is accessible from both sides.
In a first step, we pattern a square opening of $\sim$300–350 µm in the silicon nitride by means of optical lithography and subsequent reactive ion etching (RIE) with Tetrafluoromethane (CF4) on one side of the chip (Fig. 2.1 b)). This side will later on be called "back-side". The exact size of the opening depends on wafer thickness and desired membrane size and can be calculated easily with the angle between the silicon (100) surface and the (111) surface of 54.7°.
The next step is e-beam lithography, where we use ZEP520A positive e-beam resist on the clean top-side of the wafer. With a Zeiss scanning electron microscope and Raith e-line software,

we pattern 5x5 dots in the center of the wafer, where we expect the membrane to form. Due to tolerances in forming the back-side opening, we don't know the precise position of the later membrane on the top-side. By patterning 5x5 dots with a distance slightly larger than the membrane size, the chance of exactly one dot hitting the membrane is high (Fig. 2.1 c)–d)). The later pore size is determined mainly by the goodness of optimizing the electron beam (focus, astigmatism) and the exposure time, i.e. the time the electron beam hits the resist. For a fixed beam current, the exposure time is defined by the dwell time multiplied by the dose factor D. The dwell time is usually adjusted according to the beam current, so exposure can be controlled by the dose factor to get reproducible results even if the beam current changes over time. After lithography, the chip is developed in amylacetate and methylisobutylketone (MIBK), which dissolves the dots formerly hit by the electron beam. A subsequent RIE step etches the pores in the Si_3N_4 surface. After removing residual resist from the chip surface by N-Methyl Pyrrilidone (NMP), it is etched in potassium hydroxide (KOH) to create the freestanding membrane (Fig. 2.1 d)).
Single crystalline silicon has anisotropic etch characteristics in KOH; it shows different etch rates for the different lattice directions[98]. In our (100) wafer, the large square opening on the back-side will produce a pyramidal shaped etch pit when put in 20 wt% potassium hydroxide solution (KOH) at 80 °C. At the given concentration and temperature, KOH etches silicon (100) with 100 µm min^{-1}, but not silicon nitride. The Si_3N_4 membrane on the top-side therefore acts as etch stop and forms the membrane.
By e-beam lithography, pore sizes of 20 nm can be reached, but variation in size is high at the smallest possible diameter. Pores fabricated in the described manner exhibit a conical pore shape as shown in Fig. 2.2, due to thinning of the ZEP mask by the e-beam intensity profile and due to exposure of an annular region around the beam center by backscattered electrons.

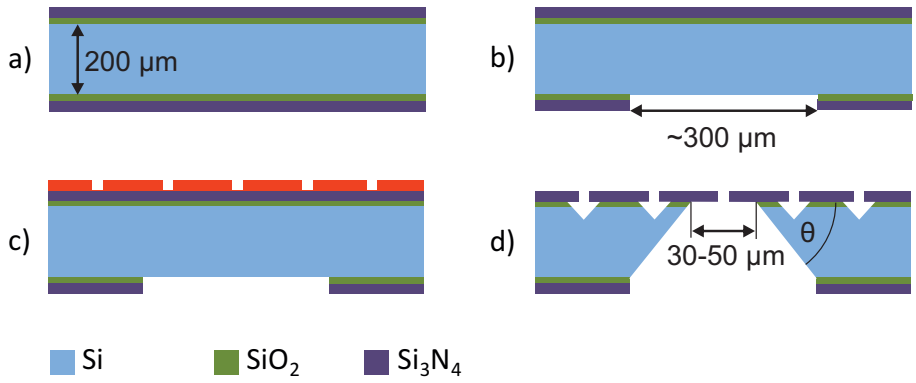

Figure 2.1: Fabrication of nanopore chips by optical and electron beam lithography. **a)** Source material: Si (200 µm) - SiO_2 (10 nm) - Si_3N_4 (50 nm). **b)** Large opening on the back-side by optical lithography and RIE. **c)** Patterning of ZEP resist by e-beam lithography. **d)** After RIE on top-side and KOH wet chemical etching. $\theta = 54.7°$

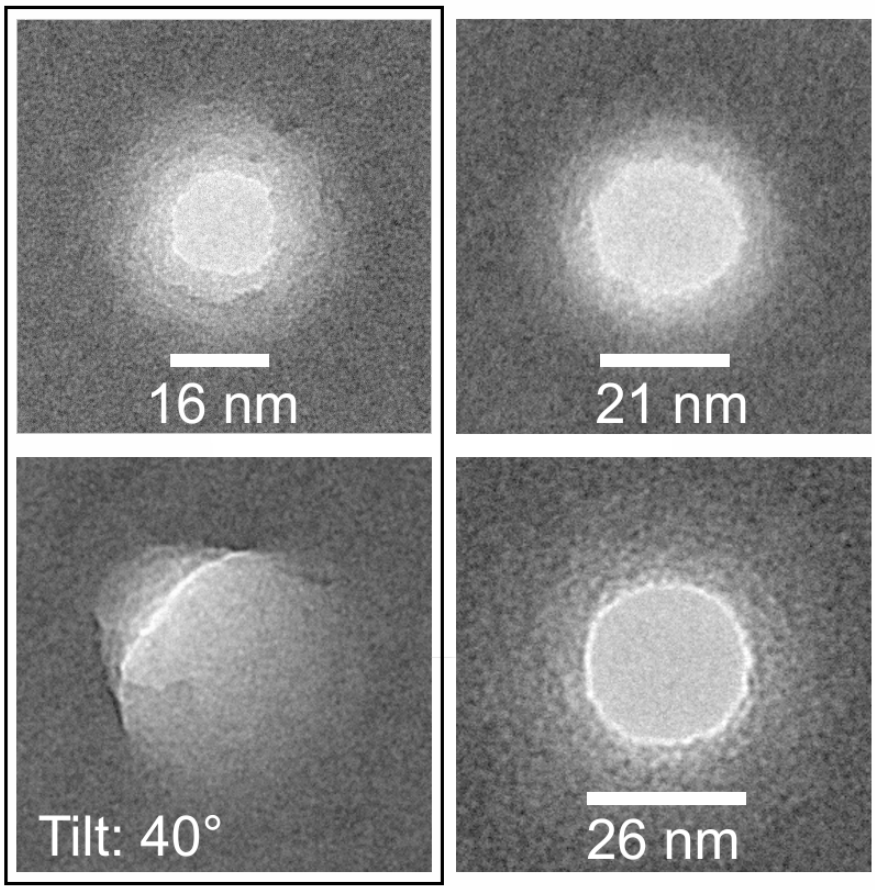

Figure 2.2: TEM micrographs of conical nanopores. The left pictures show the same pore; in the tilted image, the conical pore shape is apparent.

2.1.1. Effect of reduced development temperature

Inspired by articles on the effect of development temperature on feature size by e-beam lithography[80,120], we developed several nanopore chips at temperatures between -5 and -15 °C. This was done by placing a small beaker with amylacetate inside a larger one containg a mixture of glycerol and water (1:1)[1]. The larger beaker was encased by aluminum foil and polystyrene to ensure thermal isolation. The glycerol-water mixture was cooled down in a freezer to -19 °C prior to developing. Temperature of the amylacetate was determined by inserting a thermocouple into it. Temperature was stable within ± 1 °C for more than 3 minutes. Table 2.1 shows mean pore diameters for different e-beam doses, denoted by 'D', and development temperatures. The cooled development seems to reduce the pore diameter by 4–6 nm. The variation of pore diameters is at the same time high, and not all pores were etched completely. From 52 pores that were developed at temperatures below 0 °C, only 25 were open after reactive ion etching. The others showed still a thin layer of Si_3N_4 in TEM. Due to the low yield of open pores, we decided not to use this procedure regularly.

Table 2.1: Influence of development temperature on pore diameter.

Dose	Temp. (°C)	Diameter (nm)	Num. of chips
D18	< -10	–	no open pores
D18	RT	17 ± 1	3
D20	< -10	16 ± 5	10
D20	< 0	14 ± 5	6
D20	RT	19 ± 1.5	2
D23	< -10	14.3 ± 3	4

2.2. TEM milling

Fabrication of pores by TEM was first reported by Storm et al. in 2003[108]. Hereby a tightly focused electron beam of a TEM sputters away atoms in the Si_3N_4 membrane, until a small hole of $\sim$1 nm diameter is formed. Slightly larger pores can be formed by defocusing the electron beam, which works until the electron density is not sufficient anymore for material heating and sputtering. Larger pores of arbitrary diameter and shape can be formed by moving the sample slowly under the focused electron beam. The electron beam then ablates the material like in a milling machine. For this thesis, pores were fabricated with a FEI-Titan 80-300 at 300 keV in nanoprobe mode with $V_{extr.} = 4.5$ kV and a convergence angle of 9.2 mrad. For electroosmosis experiments, pores with diameters of $\sim$20 nm were used. For proteasome experiments, composite pores with a small opening of 4–8 nm were used.

[1] The freezing point of a 56 wt% glycerol-water mixture is -28 °C;
http://www.dow.com/glycerine/resources/table8.htm

2.3. The pit-pore device

To trap proteasome molecules inside a nanopore, composite pores were used consisting of a pit slightly larger than the proteasome dimensions and a pore, whose diameter is smaller than the proteasome diameter. A schematic of this pit-pore device is drawn in Fig. 2.3. We fabricated this device in a two-step process by e-beam lithography and subsequent TEM milling. In a first step, we carried out e-beam lithography as described above to form pits with diameter $D_{pit} = 12$–16 nm. In the subsequent RIE step, the etch time was shortened to stop etching before the membrane was penetrated completely. In doing so, an etch pit with an estimated depth L_{pit} of 20–40 nm formed in the 50 nm thick Si_3N_4 membrane, as can be seen in Fig. 2.4 a). Subsequently, a small hole with diameter D_{pore} between 4 and 8 nm was milled by TEM inside the etch pit. Figure 2.4 b) shows the resulting thickness profile for one pore. The profile was obtained from a line scan of the inset image. This image was recorded in HAADF mode[2], which resembles the material thickness very well. Finally, molecules with diameter between 10 and 20 nm may now enter the etch pit, but cannot pass through the small pore at the bottom of the pit — they are trapped for further investigations.

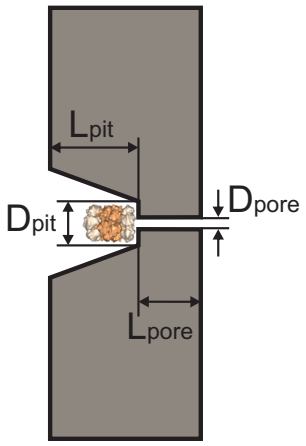

Figure 2.3: Schematic drawing of the pit-pore with a proteasome molecule.

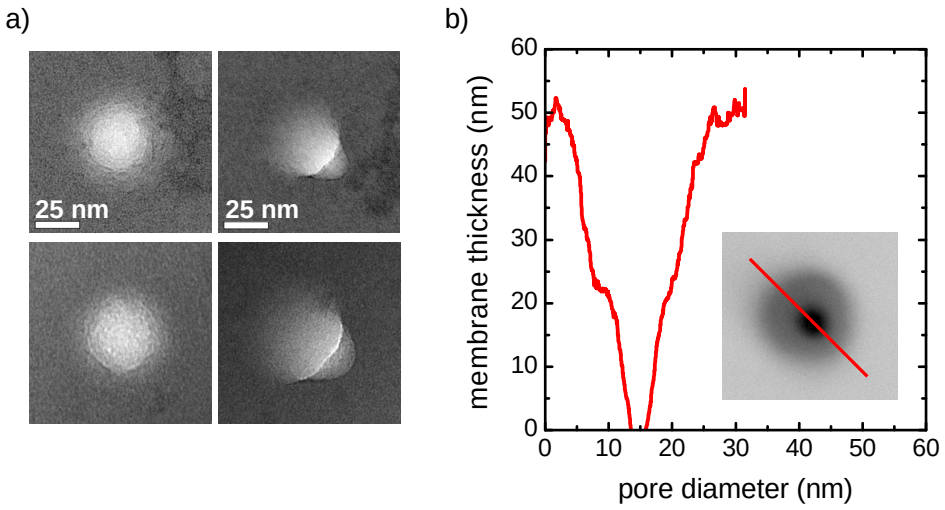

Figure 2.4: a) TEM micrographs of two etch pits in top view and tilted by 39°. **b)** Cross section of a pit-pore. The inset shows a TEM image obtained in HAADF mode and reflects the material thickness. The thickness profile was evaluated along the red line and smoothed for better visibility.

[2]High-Angle Annular Dark-Field; in this mode, contributions from Bragg-scattering are reduced and the scattering intensity depends strongly on the atomistic number.

2.4. Passivation

After successful pore formation, the membrane-side of the nanopore chip is passivated with polydimethylsiloxane (PDMS) in order to reduce the electrical capacitance and thus electrical noise during measurements. As suggested by Tabard-Cossa et al., PDMS was painted with a single looped hair brush around the membrane[110]. It is advisable to partly cure the PDMS beforehand until it shows very high viscosity. Otherwise, PDMS may flow over the membrane after painting before it is cured completely. For curing, we place the chip on a hotplate at 150 °C for 30–45 minutes. As PDMS curing is a temperature activated process, partly cured PDMS can be stored at -20 °C for several days without hardening. Figure 2.5 shows two special examples of passivated membranes (imaged with optical microscopy). As indicated by magenta circles, two pores are situated on the membrane, which would preclude single channel measurements. However, by carefully painting PDMS on part of the membrane, one pore is covered and only one pore remains open.

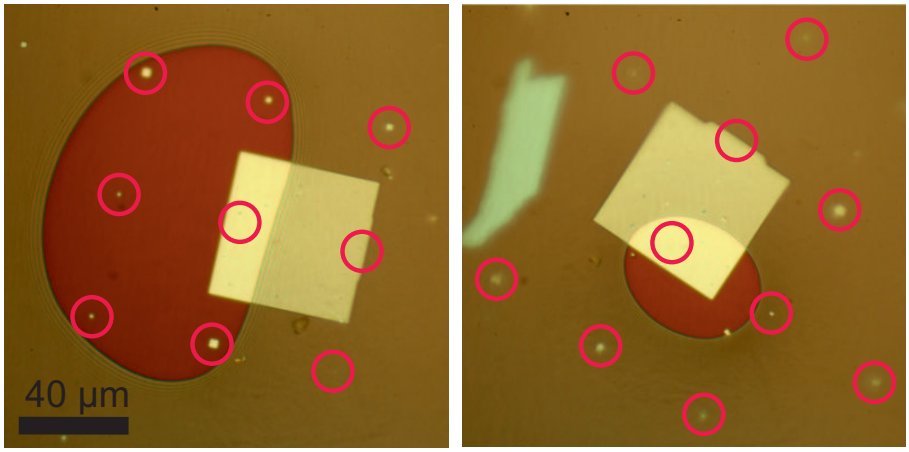

Figure 2.5: Two examples of PDMS passivation, where two pores are situated on the membrane (large, white square). Underetched pores (small, white squares) are indicated by magenta circles. The reddish color is the bare silicon nitride, the yellowish color is PDMS. With some sensitiveness and experience, one pore can be covered with PDMS to enable single channel measurements.

2.5. Instrumentation

Nanopore zeta potential and EOF measurements

A large (20x30 cm) Faraday cage of 1 cm thick iron was suspended vibration free on a granite plate and a small aluminum Faraday cage containing the measurement chamber was placed inside the larger one. The outer cage was connected to the external ground connector of the amplifier, whereas the inner cage was connected to signal ground of the headstage. An EPC-8 patch clamp amplifier and a LIH1600 DAQ interface (both from HEKA, Germany) were used. The internal (7-pole) Bessel filter was typically set to 10 kHz and data was sampled at 200 kHz. Current time traces were exported in binary matlab format for further evaluation. To be able to determine the nanopore zeta potential, we had to develop a measurement chamber, to which a static pressure of several bar could be applied. This polycarbonate measurement chamber consists of two symmetrical parts in between which the chip is placed vertically and sealed by two silicon gaskets (0.7 mm inner diameter). As can be seen in Fig. 2.6, several drilled holes permit exchange of buffer solution, insertion of electrodes and connection to pressurized air. The 400 µl reservoirs are sealed by M8 screws and electrodes are sealed by two gaskets, crimped by a drilled screw bushing. Static pressure up to 3 bar could be applied permanently by a Luer-Lock connector at the end of the reservoir. Pressure could be applied to and released from the chamber by manually opening and closing a Swagelok two-way valve.

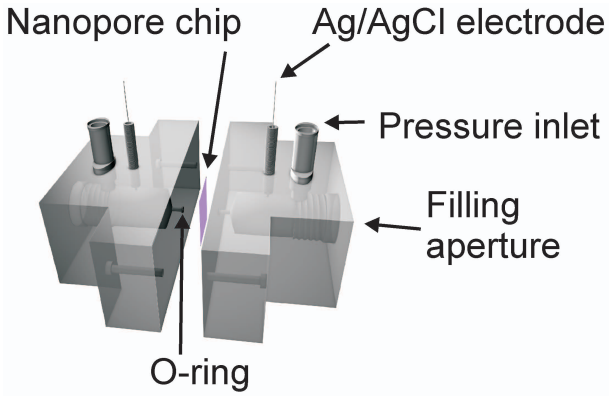

Figure 2.6: 3-d model of the pressure chamber. The length of the mounted chamber is ∼5 cm, the thickness without connectors ∼2 cm.

Proteasome measurements

Proteasome experiments were performed with a different instrumentation. Here, the outer Faraday cage was suspended vibration free in a rack and the small Faraday cage containing the measurement chamber was placed inside the larger one as before, as shown in Fig. 2.7. An Axopatch 200B patch-clamp amplifier was used and the headstage directly connected to one Ag/AgCl electrode. This ensured minimal access resistance and thus minimal electrical noise. The inner Faraday cage was connected to signal ground and the outer cage to the power socket grounding. The full bandwidth signal of the amplifier (100 kHz) was further filtered with an external 8-pole Bessel filter at 20, 50 or 100 kHz, depending on the signal-to-noise ratio. The signal was then fed into a NI-USB 6229 DAQ card and sampled at 250 kHz. The amplifier and data acquisition was controlled by a LabView program developed in our lab and data was stored as binary matlab files for subsequent evaluation.

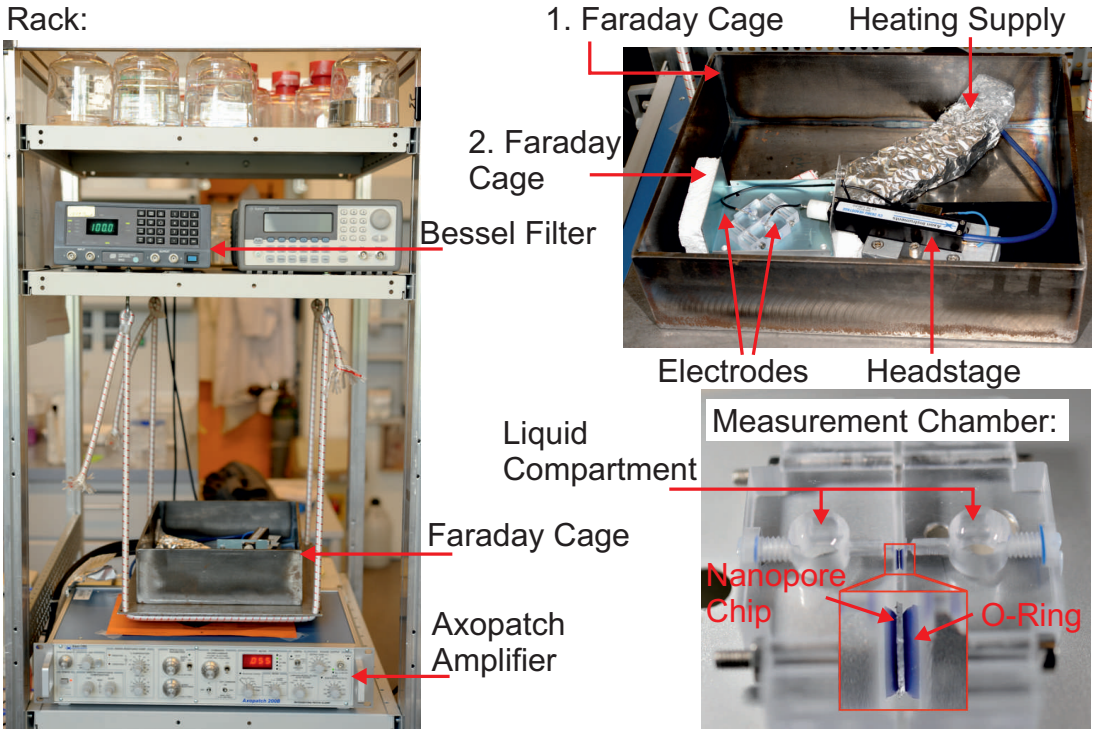

Figure 2.7: Measurement instrumentation.

For all measurements at room temperature, simple polycarbonate chambers with an open access to the ionic solution were used, as shown in the lower right picture of Fig. 2.7. The typical solution volume was 200 µl. In this chamber, protein and analyte can be added without disconnecting the pore from the amplifier and hence continuous current recordings can be carried out.

Measurements at elevated temperatures were carried out in the pressure-chamber, which is tightly sealed and prevents evaporation of solution. For heating, the inner Faraday cage with the measurement chamber was placed on a copper block. The copper block was connected to a Julabo heating circulator, whose supply pipe can be seen in the upper right picture of Fig. 2.7. The drawback of measurements in the pressure chamber is the necessity of disconnecting the electrodes and unscrewing the gasket seal for adding analytes. Continuous current recording is thus not possible. All measurement chambers were typically cleaned in Mucasol® solution by sonication for 15–30 minutes prior to a new experiment. All ionic solutions were filtered with a 200 nm cellulose acetate (CA) syringe filter before adding them to the reservoir.

Electrodes

Ag/AgCl electrodes were made by inserting the two ends of a u-shaped 0.5 mm diameter silver wire 1.5–2 cm deep in 3 M potassium chloride solution and connecting it to the positive terminal of a current source. A second silver wire in solution was grounded and a current of 250 µA was applied for 30–45 minutes. The u-shaped electrode has a dark grey to black color after this treatment and is divided to get two identical Ag/AgCl electrodes. Electrodes could be used for several weeks before slight offset and hysteresis effects could be observed.

3. Theoretical Background

3.1. Electrophoretic motion of proteins

The theory of electro-hydrodynamics and zeta potential is given in detail in the books of Bruus[16] and Hunter[47] and in a review of Schoch[95]. Here, only a collection of the most important aspects will be given. The electrophoretic force, exerted by the externally applied electric field E, is $F_E = qE$, where q is the electric charge of the molecule. If a spherical particle of radius a is moving through the liquid with velocity v_{EP}, the opposing force is the Stokes drag, $F_{drag} = -6\pi\eta a v_{EP}$[16]. Adding both forces equals zero and hence the electrophoretic velocity is

$$v_{EP} = \frac{qE}{6\pi\eta a} = \mu \cdot E\,, \tag{3.1}$$

where η is the solution viscosity and μ is the mobility of the particle.
The charge q can be calculated by integrating over the charge density ρ around a spherical particle. ρ is given by the Poisson equation and for small potentials compared to k_BT the charge is given by

$$q = 4\pi\epsilon a\zeta(1 + \kappa a), \tag{3.2}$$

with the zeta potential ζ defined at the slip plane, the dielectric constant $\epsilon = \epsilon_0\epsilon_r$ and the inverse Debye length κ. As this calculation is based on the Debye-Hueckel approximation, it overestimates the charge if $q \cdot \zeta > \sim$25 meV.
The electrophoretic velocity can now be expressed as:

$$v_{EP} = \frac{2\epsilon}{3\eta}\zeta_{prot} \cdot E(1 + \kappa a). \tag{3.3}$$

Henry (1931) showed that this formula is valid only for $\kappa a \ll 1$, when the applied electric field is not deformed by the particle. He introduced a function $f(\kappa a)$, known as the Henry function, which accounts for the deformation of the electric field around the particle. The velocity is then expressed as:

$$v_{EP} = \frac{2\epsilon}{3\eta}\zeta_{prot} \cdot f(\kappa a) \cdot E, \tag{3.4}$$

with the Henry function

$$f(\kappa a) = \left[1 + \frac{1}{2(1 + (2.5/\kappa a\{1 + 2\,exp(-\kappa a)\}))^3}\right]. \tag{3.5}$$

In the limit $\kappa a \gg 1$, the function f approaches 1.5, leading to the expression

$$v_{EP} = \frac{\epsilon}{\eta}\zeta_{prot} \cdot E, \tag{3.6}$$

which is also known as the Smoluchowski equation. In this thesis we are dealing with ionic concentrations between 0.4 and 1 M. For a particle with radius $a = 5$ nm, we thus get $\kappa a \approx 10$–17 and $f(\kappa a) \approx 1.2$–1.4, which is close to the Smoluchowski limit.

3.2. Electroosmotic flow in solid-state nanopores

The electroosmotic flow originates in an external electric field parallel to a charged surface. The electric field acts on the accumulated Debye layer ions of charge density ρ. The motion of DL ions creates a shear stress $\tau = \eta\partial v_x/\partial r$ which sets the liquid across the whole channel in motion. The flow profile can be calculated by solving the Navier-Stokes equation for a constant zeta potential ζ, homogeneous electric field E, steady state flow $v_x(r)$ and a Debye length κ^{-1} much smaller than the channel diameter a. The result is

$$v_x(r) = \left(1 - \frac{I_0(\kappa r)}{I_0(\kappa a)}\right)\frac{\epsilon\zeta}{\eta}E \tag{3.7}$$

where I_0 are Bessel functions of order 0. If the Debye layer is small compared to the channel diameter, the velocity is approximately constant over the pore cross section. This is shown in Fig. 3.1 together with the space charge density.

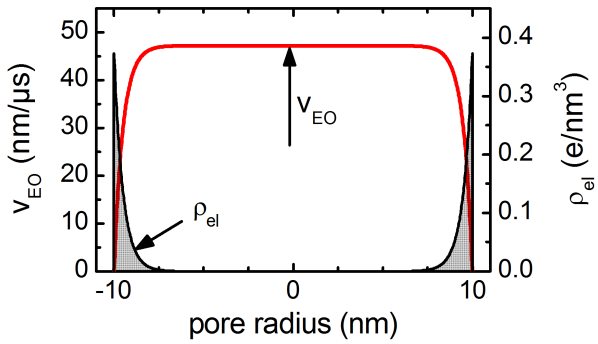

Figure 3.1: Flow profile (red) and charge density (black) in a Si_3N_4 nanopore of 20 nm diameter, 0.4 M KCl, $V_{ext} = 150$ mV, $\zeta = -20$ mV.

Due to the shape of the velocity profile, it is also called “plug flow profile”. In this case, the electroosmotic velocity can be expressed as

$$v_{EO} = \frac{\epsilon\zeta}{\eta} \cdot E, \tag{3.8}$$

which is essentially the same as for the electrophoretic motion of a particle in the Smoluchowski limit. In fact, the physical origin of both effects is essentially the same. In EP, a charged particle moves in a stationary liquid, and in EO the liquid is moving along a stationary and charged wall. Formula 3.8 is also valid for the experiments presented in this thesis, where $\lambda_D \approx 0.5$ nm and $d_{pore} \approx 20$ nm. If we assume a zeta potential of -20 mV and a channel length of 50 nm, an applied voltage of 150 mV would result in a flow velocity of 47 nm/µs.

3.3. Nanopore zeta potential

As we have seen before, the EOF depends on the zeta potential of the wall. Measurement of the zeta potential is possible by changing the driving forces: Instead of the electric field being responsible for a plug flow, we can apply an external pressure, thereby pushing the Debye layer ions along the channel and creating an ionic current. This is also called "streaming current" measurement and is used since decades to determine zeta potential in large (µm sized) parallel plate channels and porous membranes[13,17,44,56,92,95,115,128]. The streaming current can be calculated by integrating the charge density and flow velocity over the channel volume:

$$I_s = \int_V v_z(r)\rho(r)dV. \tag{3.9}$$

A detailed calculation is given by Hunter[47]; it comprises a substitution of ρ from Poisson's equation and partial integration. Furthermore it takes advantage of the fact that only the region at the channel surface ($r \approx r_{pore}$) contributes to the integral. Finally, we get the expression:

$$I_s = \frac{A}{l}\frac{\epsilon\zeta}{\eta}p, \tag{3.10}$$

where A is the cross sectional area, l the pore length and p the externally applied pressure. It would be possible to derive the zeta potential from Eq. 3.10. However, the pore geometry must be known, which could involve an uncertainty in the result. For a cylindrical channel, this problem can be eliminated by applying Ohm's law, $U = \frac{1}{\sigma}\frac{l}{A}I$, where σ is the bulk solution conductivity. Substituting A/l in Eq. 3.10, we get an expression for the streaming potential:

$$\frac{\Delta U}{\Delta p} = \frac{\epsilon\zeta}{\eta\sigma}. \tag{3.11}$$

This expression is valid if surface conduction can be neglected[67,68], which implies $\kappa a \gg 1$ and moderate ($\sim k_B T$) zeta potentials.

3.4. Protein translocation time

3.4.1. Free translocation

For the free translocation of a molecule through a pore, neglecting any protein-pore interaction, different driving forces exist that influence especially the translocation direction and rate of the molecule. Until recently, only electrophoresis was considered as the dominating driving force in nanopore experiments[33,42,43,111]. However, especially electroosmosis and diffusion can influence the translocation dynamics considerably, as will be shown in the experimental section of this thesis.
The translocation time for a molecule passing the pore without surface interactions can be ex-

pressed as $\tau = l_p/v$, where l_p is the pore length and v the velocity of the molecule. Combining the electrophoretic velocity v_{EP} (Eq. 3.6) with the velocity of the electroosmotic flow v_{EO} (Eq. 3.8) gives the effective particle velocity

$$v_{eff} = v_{EP} + v_{EO} = \frac{\epsilon E}{\eta}(\zeta_{prot} - \zeta_{pore}). \tag{3.12}$$

Depending on the value and relative signs of protein and pore zeta potentials, translocation may be dominated by electrophoresis, electroosmosis or diffusion, namely when $\zeta_{prot} = \zeta_{pore}$. In this case, we would observe translocation events independent of the applied voltage. Eq. 3.12 also implies that EO and EP forces may counteract or enhance each other.

Diffusion

The diffusion rate of a molecule through a pore is described by Fick's law: $\frac{dn}{dt} = DA\frac{dC}{dx}$, where D is the diffusion constant, A the cross sectional area, C the concentration and x the coordinate along the pore axis. If the pore is short compared to the diffusion length, dC can be set as the particle concentration on one side of the pore and dx as the pore length l_p. If we are only interested in the time a single particle needs to travel the distance L by Brownian motion, the diffusion time in one dimension can be expressed as $\tau = \frac{L^2}{2D}$. The Diffusion constant D can be approximated as $D = \frac{k_B T}{6\pi\eta r}$ for spherical particles of radius r.
Usually, translocation by diffusion is slower than by EP or EO forces. For a spherical particle of radius 5 nm, diffusion through a 50 nm long channel will take ∼30 µs. The expected time for free translocation of a particle through a pore will thus be in between the diffusion time and the EO or EP translocation time.

3.4.2. Protein adsorption

Sexton et al. proposed a simple model of unspecific protein adsorption for nanopores[100], which can be described by well known reaction kinetics. Herein, adsorption and desorption processes are described by first order reaction rates according to the Arrhenius equation

$$k_d(0) = A \cdot e^{-E_a/k_B T}. \tag{3.13}$$

The translocation time then depends on the number of adsorptions during translocation and the applied voltage, which lowers the energy barrier for desorption[109]. The dissociation constant under the presence of an electric field $E = V/l_p$ can be written as

$$\begin{aligned} k_d(F) &= k_d(0) \cdot e^{F_{el}x/k_B T} \\ &= k_d(0) \cdot e^{q\frac{V}{l_p}x/k_B T}, \end{aligned} \tag{3.14}$$

where x is a small separation in direction of the applied force that has to be overcome for desorption. If translocation is dominated by adsorption processes, we thus expect $\tau \propto e^{-V}$ for the voltage dependence of the translocation time, whereas we would expect $\tau \propto 1/V$ for free

translocation. As we will see in Chap. 5.2.1, both functions can be fitted equally well if the fitting range is small (-150 to -225 mV), which complicates interpretation of the translocation mechanism.
If we also consider EOF to act on the particle during adsorption, the situation gets more complicated. Neglecting hydrodynamic surface effects, the EO force acting on an adsorbed particle can be described by the Stokes drag $F_{EO} = -6\pi\eta a \cdot v_{EO}$. Within the Smoluchowski limit, we use Eq. (3.8) and get

$$F_{EO} = -6\pi a\epsilon\zeta_{pore} \cdot E. \tag{3.15}$$

The force implied by electrophoresis can be derived by using equations (3.1) and (3.6):

$$F_{EP} = q \cdot E = 6\pi\eta a \cdot \frac{q}{6\pi\eta a} \cdot E = 6\pi a\epsilon\zeta_{prot} \cdot E\,. \tag{3.16}$$

For the total pulling force acting on a particle inside a nanopore under an EOF follows

$$F_{tot} = F_{EP} + F_{EO} = 6\pi a\epsilon \cdot E(\zeta_{prot} - \zeta_{pore})\,. \tag{3.17}$$

For the dissociation constant we can thus write

$$k_d(F) = A \cdot e^{-E_a/k_BT} \cdot e^{6\pi a\epsilon\cdot\Delta\zeta\, E\, x/k_BT}. \tag{3.18}$$

An exact determination of the first term in Eq. (3.18), $k_d(0)$, is difficult because not only electrostatic effects are involved, but also hydrophobic and hydrodynamic interactions, as will become clear in the experimental chapter.

3.5. Nanopore resistance

To evaluate current blockades from molecules inside nanopores, it is important to know the pore resistance without any molecule inside. This open pore resistance R_o depends on the pore geometry and surface effects for salt concentrations below 100 mM[104]. For cylindrical pores, it can be described as

$$R = \frac{4l_p}{\pi d_p^2}\left((\mu_{K^+} + \mu_{Cl^-})n_{KCl}e + \mu_{K^+}\frac{4\sigma_s}{d_p}\right)^{-1}\,, \tag{3.19}$$

where μ_{K^+} and μ_{Cl^-} is the mobility of potassium and chloride ions, σ_s is the salt dependent surface charge, l_p the pore length and d_p the pore diameter. As we are typically using 0.4–1 M KCl in our experiments, surface effects may be neglected and the pore resistance is sufficiently described by

$$R = \frac{l_p}{\sigma\pi r_p^2}\,, \tag{3.20}$$

where σ is the bulk conductance of the electrolyte solution. For pores with a diameter similar to the pore length or even bigger, the access resistance R_a has to be taken into account[41].

R_a accounts for the transition of the electric field between its bulk value and the value inside the nanopore. It is given for cylindrical pores as

$$R_a = \frac{1}{4\sigma r_p} \tag{3.21}$$

and has to be taken twice for the pore opening and end.

Because our self fabricated nanopores have a conical shape as described in chapter 2, the equations given for cylindrical pores do not hold anymore. For conical pores, the resistance can be calculated by

$$R = \frac{1}{\sigma} \int_{l_p} \frac{dx}{A(x)} \, , \tag{3.22}$$

where $A(x) = \pi(r_o + \tan\alpha \cdot x)^2$ is the area of the pore depending on the position x on its center line, the opening angle α and the radius of the small pore opening r_o. This expression can be approximated by

$$R_{con} = \frac{l_p}{\sigma \pi r_o r_l} \, , \tag{3.23}$$

where r_l is the radius at the large opening of the conical pore. The validity of this geometric mean approximation was shown by Maxwell[70] and also used by other authors in the nanopore field to calculate the ionic resistance of conical pores[4,26,62]. For numerical simulations of the pore resistance, especially when simulating conductance changes due to protein translocations, the general form (3.22) is used and the area $A(x)$ adapted to the shape of the translocating particle. The access resistance introduced above plays also a crucial role for conical pores. Neglecting deviations which might arise for the conical shape, we calculate the total access resistance as

$$R_{a,con} = \frac{1}{4\sigma r_o} + \frac{1}{4\sigma(l_p \tan\alpha + r_o)} \, . \tag{3.24}$$

Because we can only measure the small diameter of the conical pore in TEM, we prefer the expression $l_p \tan\alpha + r_o$ for the large radius (r_l in Eq. 3.23). The opening angle was determined in our group by TEM tomography[126] to be around $19 \pm 3^\circ$. Fitting of experimental values is very critical on this angle, whereas the pore length plays only a minor role, due to the fact that for increasing length the diameter is also increasing in conical pores with a fixed small pore opening. The total resistance of a conical pore is then

$$R_{con,tot} = R_{a,con} + R_{con} = \frac{1}{4\sigma r_o} + \frac{1}{4\sigma(l_p \tan\alpha + r_o)} + \frac{l_p}{\sigma\pi r_o(l_p \tan\alpha + r_o)} \, . \tag{3.25}$$

3.6. Excluded volume

Many authors give expressions for the excluded volume of a particle when it traverses the nanopore. By calculating the excluded volume from the current blockade height and comparing it to the theoretical expected volume of the protein, one can draw conclusions on the conformation of the protein, i.e. if it is folded or unfolded during translocation[34,83,90,111]. For cylindrical pores, the current blockade height is given by[33]

$$\Delta I = \frac{\sigma V d_m^2 l_m}{H_{eff}^2} \left[1 + f(d_m, D_p, L_m, H_{eff})\right] \ , \tag{3.26}$$

which can be used to estimate the current blockade in dependence of the molecule volume $d_m^2 \cdot l_m$, the effective pore length H_{eff} and the applied potential V.
For conical pores, Eq. (3.26) does not hold anymore, as the current blockade varies with the molecule position inside the nanopore. Here we have to calculate the current blockade height numerically using equation (3.22).

Because we show experimental investigations on a barrel shaped protein in chapter 5 of this thesis, we now present theoretical calculations of the conductance blockade caused by a cylindrical object of radius r_m and length l_m in a conical pore. For this simulation, the cross sectional area of the pore at position x along the pore axis is expressed as $A_o(x) = \pi(r_o + \tan\alpha \cdot x)^2$ for the part without protein and $A_b(x) = A_0(x) - \pi r_m^2$ for the part with the protein. We assume the protein and pore to be oriented uniaxially. The total resistance of the pore with a protein present can thus be calculated as:

$$R_b(x_m) = R_{a,con} + \int_0^{x_m} (\sigma A_o(x))^{-1}\, dx + \int_{x_m}^{x_m+l_m} (\sigma A_b(x))^{-1}\, dx + \int_{x_m+l_m}^{l_p} (\sigma A_o(x))^{-1}\, dx \ , \tag{3.27}$$

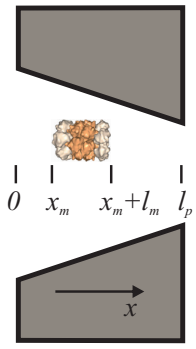

Figure 3.2: Definition of positions in conical pores.

where x_m is the position of the proteasome inside the pore as shown in Fig. 3.2. Per definition, the protein has already entered the pore completely at $x_m = 0$, and at the last value of x_m the molecule begins to exit the pore, thus $x_m(end) = l_p - l_m$. We thereby neglect an influence of the protein on the access resistance.
The relative change in current depending on the position x_m of the molecule inside the pore can be calculated with Eq. 3.25 and 3.27 as:

$$\Delta I(x_m) = (1 - R_{con,tot}/R_b(x_m)) \cdot 100\% \ . \tag{3.28}$$

Three parameters of pore geometry influence the conductance blockade: Diameter, length and opening angle, as shown schematically in Fig. 3.3. The influence of different opening angles is depicted in Fig. 3.4. The different lines belong to different opening angles and for each angle, the

conductance blockade is drawn in dependence of proteasome position along the pore axis. The opening angle is varied from 16° to 22° top down. Even if the opening angle influences the total resistance of the pore considerably, it has only minor influence on the relative conductance blockade. The maximum blockade at the end of the pore decreases by only 1%.

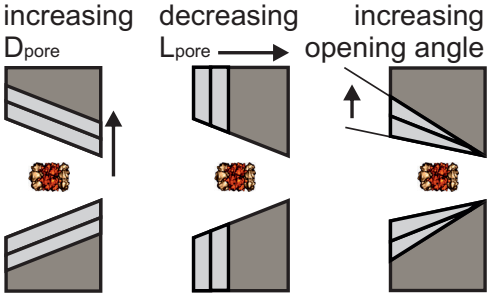

Figure 3.3: Variation of conical pore dimensions as simulated in Fig. 3.4 and Fig. 3.5 a) – b).

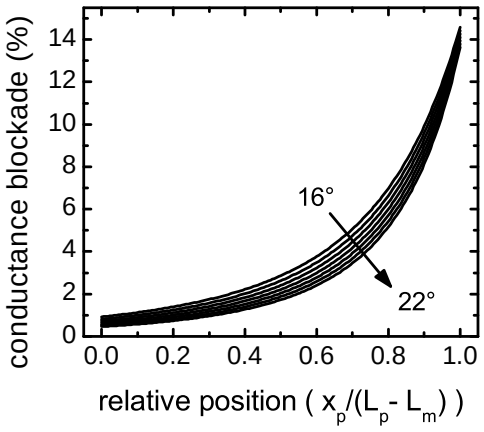

Figure 3.4: Conical pore conductance blockade simulation. Lines top down: 16°–22° opening angle of the pore (Step 1°).

The pore length is varied in Fig. 3.5 a), even if we did not change this parameter systematically in our experiments. The lines from bottom up represent decreasing pore length, from 50 to 20 nm. It is interesting that the maximum current blockade increases by only 2.5%. The most prominent difference between different pore lengths is the generally higher blockade for all protein positions in short pores, which might improve the signal to noise ratio for fast translocating proteins. However, for molecules which tend to adsorb on the pore walls, the membrane thickness in the investigated range plays only a minor role, as conductance blockades in the range of 2–4% for the longest pores are well observable under most experimental conditions.
The strongest effect on conductance blockade can be obtained by variation of the pore diameter. This is shown in Fig. 3.5 b), where the diameter is decreased from 30 nm to 16 nm. Accordingly, the maximum blockade increases from 4 to 20% at the end of the pore.
As will be shown in chapter 5.2, the presented theory for modelling position dependent conductance blockades is in excellent agreement with experiments.

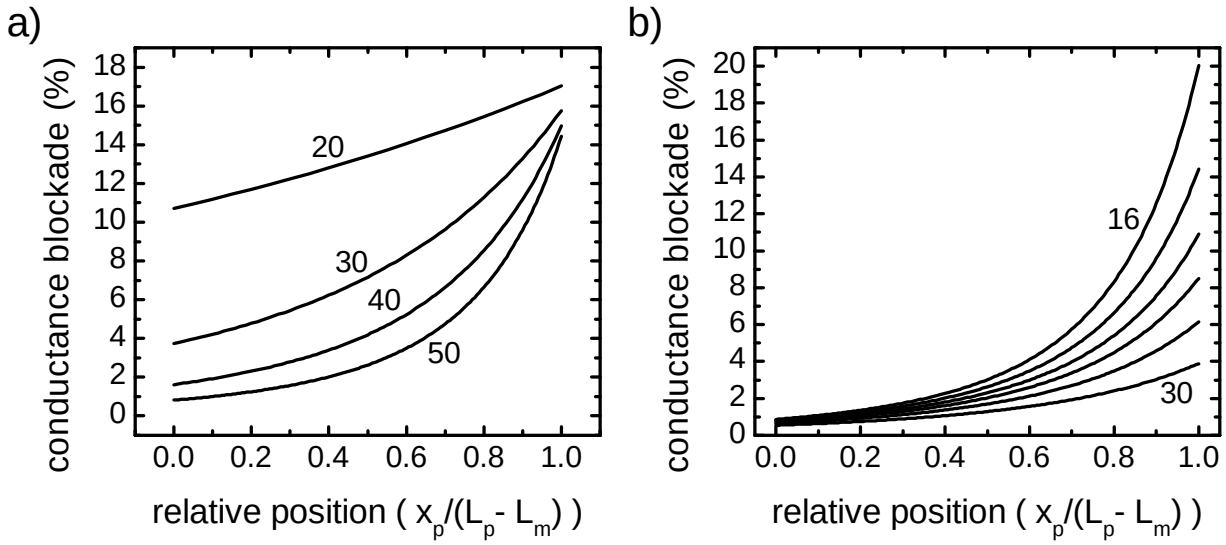

Figure 3.5: Conical pore conductance blockade simulation. **a)** Conductance blockade for different pore length. Lines top down: 20, 30, 40 and 50 nm. **b)** Conductance blockade for different pore diameter. Lines top down: 16, 18, 20, 22, 25 and 30 nm pore diameter.

4. Electroosmotic Flow in Silicon Nitride Nanopores

4.1. Introduction

In this chapter we study the translocation behavior of a model protein, avidin, through a 20 nm wide and 30 nm long nanopore in a Si_3N_4 membrane. We investigate the influence of the protein zeta potential (ζ_{protein}) and the pore wall potential (ζ_{pore}) on the translocation direction and the translocation rate. At first we separately characterize ζ_{protein} and ζ_{pore} in solution as a function of varying pH and salt concentration. Then, we present measurements of the translocation behavior of avidin through the pore at varying pH values and discuss different cases where the protein and the pore are likewise positively or negatively charged, and where the protein and the pore are oppositely charged. We argue that the protein translocation direction and rate is governed by a combined action of electrophoretic (EP) and electroosmotic (EO) forces, and diffusion. This argumentation is supported by measurements with a different protein, streptavidin, which is presented in Appendix A.

4.2. Protein zeta potential

We measured the electrophoretic velocity of avidin in AC electric fields in solution by phase analysis light scattering (PALS laser Doppler electrophoresis) using a Zetasizer Nano instrument (Malvern Ltd., UK). From this velocity, the mobility and thus the zeta potential can be derived for a spherical particle, as described by Eq. (3.4). For a different project in our group, ζ_{protein} was determined in low ionic strength solutions (Hückel-Onsager limit) by J. Knezevic[58] (10 mM Tris, adjusted with HCl or NaOH to the desired pH). For zeta potential measurements in higher ionic strengths, the mobility was corrected with the interpolated Henry function[81] as given in Eq. (3.5) and the mobility is expressed as $\mu = \frac{2\epsilon}{3\eta}\zeta_{prot} \cdot f(\kappa a)$. For very high salt concentration, $f(\kappa a) \to 3/2$, which leads to Smoluchowski's equation, presented in Chap. 3.
Figure 4.1 a) shows the hydrodynamic diameter ($\mathrm{D_h}$) as determined by dynamic light scattering (DLS) and Fig. 4.1 b) shows ζ_{protein} of avidin for different pH values under low salt conditions (blue, filled squares). ζ_{protein} is around +20 mV for pH $\leq$ 8, then drops rapidly, crosses 0 mV between pH 9–9.5, and becomes negative for pH $>$ 9.5. Hence, the pI value is 9.3 ± 0.2. The hydrodynamic diameter $\mathrm{D_h}$ stays approximately constant within 6 ± 1 nm over the investigated pH range, indicating that the protein stays intact, i.e. does not unfold under these conditions, which is in agreement with other reports[36].

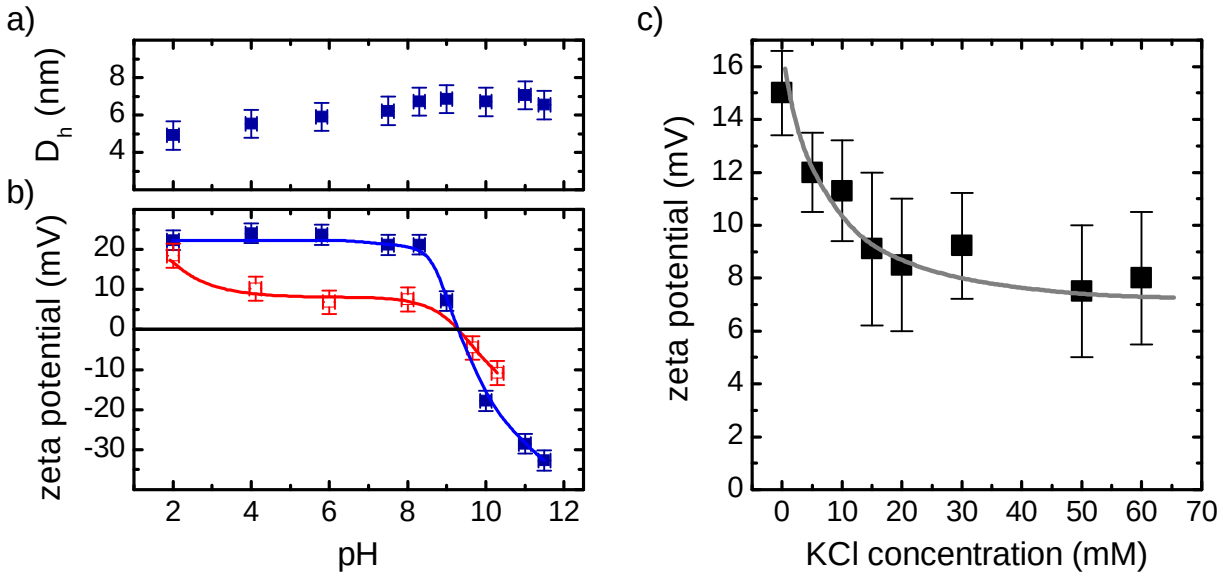

Figure 4.1: a), b) Hydrodynamic diameter and zeta potential of avidin for varying solution pH values. Blue points indicate low salt condition (10 mM Tris), red points indicate measurement at 50 mM KCl. **c)** Zeta potential of avidin in dependence of salt concentration at pH 7.3. Solid lines are guides to the eye.

Because electrical experiments with nanopores are usually performed with solutions of high conductance (high salinity), we studied the salt concentration dependence of ζ_{protein}. The measurement mode of the Zetasizer was set to monomodal[1] with a maximum of 100 runs. Depending on solution conductivity, the applied potential of the AC field was adjusted to keep the current below 1 mA in order to avoid Joule heating of the sample, which would alter protein mobility. Without KCl (buffer only), 150 V could be applied to the capillary cell, but only 20–50 V for a KCl concentration larger than 30 mM. Consequently, the necessity to apply low voltages impaired the signal-to-noise ratio which in turn limited the possibility to conduct measurements in high conductivity solutions. Moreover, the electrode surfaces corroded quickly in high salinity solutions, which required a frequent exchange of the measurement cells. Figure 4.1 c) shows that ζ_{protein} quickly decreases with increasing KCl concentration, in accordance with observations for other biomaterials and minerals[39,79,105,112], and saturates at roughly 50% of the low ionic strength value when [KCl] $\geq$ 50 mM. A determination of the electrophoretic mobility at higher salt concentrations was impeded by the effects mentioned above, but the absence of protein aggregation as evidenced by DLS even at KCl concentrations up to 400 mM, strongly suggests that the proteins retain their charged nature at high ionic strength. This is shown in Fig. 4.2, where the obtained intensity auto-correlation function was fitted with a number-weighted distribution of exponential decays. The inset shows the number (red) and intensity (black) distribution of size classes, which is derived from the exponentials. The intensity distribution gives typically larger

[1] monomodal means that only one type of dispersant is present in solution, i.e. same size and electrical charge for all particles.

size classes than the number distribution, because the intensity of the scattered light depends on the particle diameter to the power of 6 (Rayleigh scattering). However, the number distribution resembles the number fraction of particles and should thus be considered. The measured protein diameter is 6.2 ± 1.2 nm, in accordance to the values found for the low salt measurements (Fig. 4.1 a)). In comparison, protein solutions where the pH value was adjusted close to pI were unstable and gradual protein aggregation was observed.

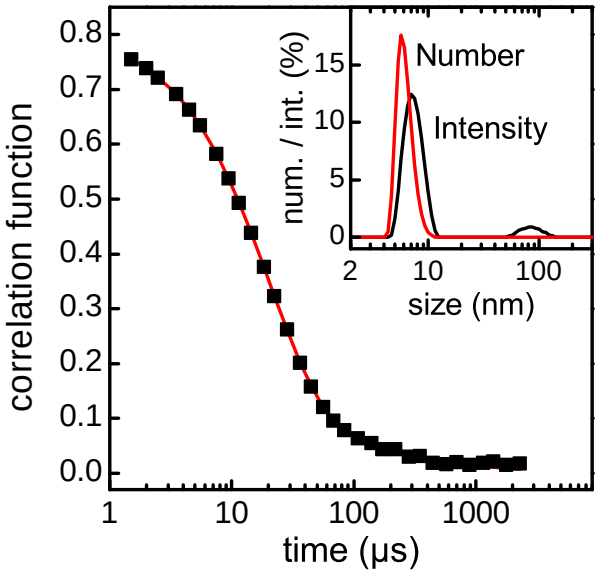

Figure 4.2: Determination of the hydrodynamic diameter of avidin in 400 mM KCl. The correlation function is fitted with a distribution of exponential decays (red line). Inset: Number and intensity distribution of size classes.

The pH dependence of ζ_{protein} representative for the high ionic strength ([KCl] = 50 mM) case is shown as open, red symbols in Fig. 4.1 b). For this measurements, pH was adjusted by adding HCl (pH 2), sodium citrate (pH 4), sodium actetate (pH 6), Tris-HCl (pH 8) or sodium carbonate/bicarbonate (pH 10) in concentrations of 10 mM. These buffer types were also used for the later protein translocation experiments. Except for pH 2, the zeta potential is reduced over the whole pH range by at least 50%. Together with the finding of zeta potential saturation, see Fig. 4.1 c), we assume these values to hold also for comparison with the pore zeta potential at 400 mM KCl.

Similar measurements were also conducted for streptavidin in low conductivity solution[58]. Here, the zeta potential vs. pH dependence is slightly different to avidin. Streptavidin is positively charged at pH 4 (+20 mV), carries no net charge at pH 6 ($\sim$0 mV) and is negatively charged at pH 8 (-13 mV). For interpretation of streptavidin translocations in Appendix A, we use 50% of the just mentioned values as an estimate of ζ_{SA} at high ionic strength.

4.3. Pore zeta potential

Nanopores were fabricated in free-standing 30 nm thick Si_3N_4 membranes by direct milling with a 300 keV electron beam in a TEM[108], as described in chapter 2. The zeta potential of the inner pore walls in the Si_3N_4 membrane was determined by streaming potential measurements[47,56]. For that purpose, the nanopore chip was installed in a homebuilt pressure cell, which is described in chapter 2, where the chip is sandwiched between two liquid compartments to which a differential static pressure of up to 3 bar could be applied. The streaming potential was determined in constant current mode of the EPC 8 amplifier. The potential applied to Ag/AgCl electrodes was adjusted, so that the measured ionic current generated by the pressure driven flow through the pore vanished. The 7-pole Bessel filter was set to 3 kHz and the sampling rate was 20 kHz. The pressure was set by connecting pressurized air via a pressure reduction valve to the measurement chamber and varied between 1 and 2.5 bar in steps of 0.5 bar. For each pressure step, 4 cycles were performed, where the applied pressure was switched between 0 and the designated value. Each of this 8 runs lasted for 2 seconds, and the measured streaming potential was recorded with the patch clamp amplifier. The average value of each run was calculated and the streaming potential difference for the two subsequent runs in each cycle was calculated. This gives four potential values, which were again averaged for each pressure and the dU/dP dependence was obtained for each of the four pressure values. This procedure seems complicated at first sight, but is necessary to improve statistical relevance of the data. As the surface which determines the streaming potential is very small, short term variations in surface chemistry or pressure lead to fluctuations in streaming potential, which have to be averaged out. Figure 4.3 a) shows the differential average values for each cycle between 0 and x bar of a streaming potential measurement in 400 mM KCl (pH 9) for increasing and decreasing pressure; hysteresis effects for decreasing pressure steps were not observed.

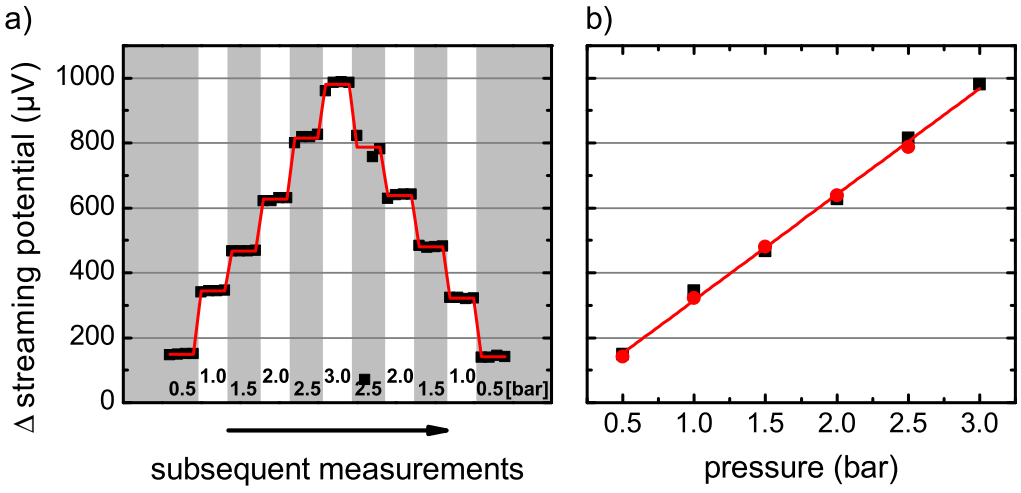

Figure 4.3: a) Streaming potential measurement for varying pressure. The red line depicts average values. **b)** Dependence of streaming potential on the applied pressure. Red line indicates a linear fit.

Figure 4.3 b) shows a linear fit to the mean values of the streaming potential, from which the zeta potential of the nanopore was derived using Eq. 3.11. The inset of Fig. 4.7 also depicts streaming potential values measured for increasing pressure for a different pore. Under the assumption of a cylindrical pore, the analysis of the streaming potential does not require the knowledge of pore diameter and length (as does the analysis of the streaming current), but relies on the conductivity σ_{pore} inside the pore lumen only. Given that the electrical double layer is very thin ($\lambda_{\mathrm{D}} = 0.5$ nm at 400 mM KCl) compared to the dimensions of the pore ($\sim$20 nm diameter), σ_{pore} was approximated by the bulk solution conductivity (see Chap. 3.3 and 3.5), $\sigma_{\mathrm{bulk}} = 4.7$–$5.1$ S/m (depending on pH, measured with a conductometer).
Streaming potential measurements were conducted in solutions of varying pH (2–10) and the obtained zeta potential is presented in Fig. 4.4. ζ_{pore} is slightly positive for acidic pH values ≤ 4, crosses 0 mV at pH $\sim$5, becomes increasingly negative at higher pH, and saturates at roughly -25 mV.

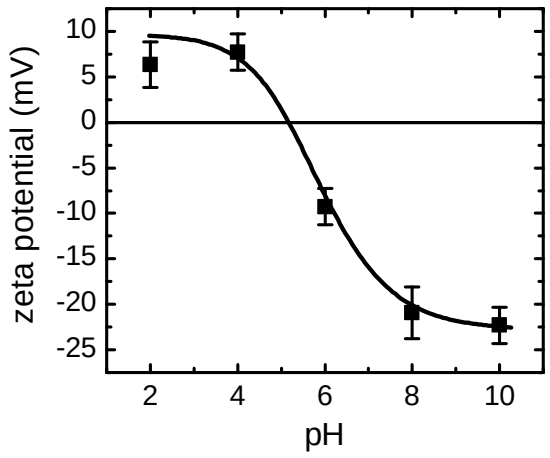

Figure 4.4: pH dependent zeta potential of a Si_3N_4 nanopore in 400 mM KCl. Error bars reflect variations between different pores. The solid line is a guide to the eye.

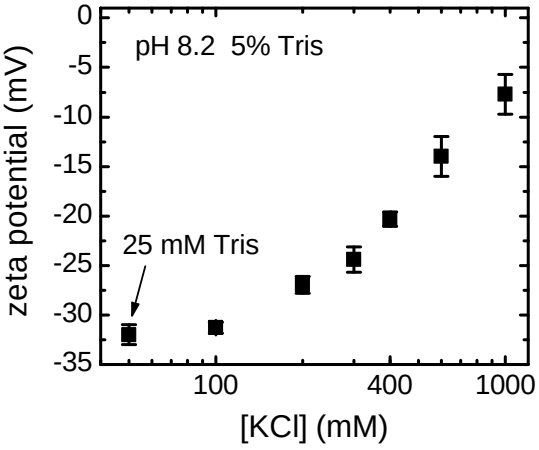

Figure 4.5: Dependence of zeta potential on KCl concentration at pH 8.2, 5% Tris-HCl.

The observed trend of ζ_{pore} reflects the chemistry of the silicon nitride surface which tends to hydrate into a surface containing silanol (SiOH) and primary amine ($SiNH_2$) sites[44]. Silanol sites are amphoteric and may become negatively or positively charged (SiO^- / $SiOH_2^+$) while primary amines can become positively charged (NH_3^+). Harame's two-site model[44] predicts that the point of zero charge ($\mathrm{pH_{pzc}}$) adjusts according to the ratio of silanol and amine groups on the surface, which have $\mathrm{pK_a}$ values of 2 and roughly 10, respectively. For our devices we estimate from $\mathrm{pH_{pzc}} \approx 5$ that 10–30% of the reactive sites are amines, while 70–90% are silanol groups. The result strongly depends on the assumed equilibrium constants for the silanol and

amine reactions and should thus not be overestimated. It is furthermore known that the curve progression depends on the preparation process of the Si_3N_4 surface[44,72]. Even between different pores (drilled on membranes from the same manufacturer), we observed device-to-device variations of ± 2 mV. Despite the extremely small dimensions of the nanopore, the dependence of the obtained zeta potential on the pH value shows reasonable agreement with the literature, where $\mathrm{pH_{pzc}}$ values between 3 and 6 are reported for planar surfaces and long channels[13,14,44]. The fact that our ζ_{pore} values are somewhat smaller in magnitude than other literature reports, can be attributed to the high salinity used here. $|\zeta_{\mathrm{pore}}|$ increases for decreasing salt concentration, an effect which is expected from theory[105] and experiments[39,79,112].
Figure 4.5 shows a measurement for salt concentrations between 50 mM and 1 M KCl. With increasing concentration, the zeta potential gradually decreases from -32 mV to -8 mV. This behavior can be explained by a concentration dependent amount of adsorbed counter ions, shielding the surface charge of the pore[105]. An even bigger influence on zeta potential can be observed for divalent ions, such as $NiCl_2$. As can be seen on Fig. 4.6, addition of only 1 mM $NiCl_2$ to a solution of 600 mM KCl at pH 9.2 decreases the pore zeta potential by 50%. Interestingly, the plateau between 1 µM and 100 µM shows very similar zeta potential (-13 $\pm$ 1 mV) as the measurements without $NiCl_2$, indicated by the red horizontal line (-13.5 $\pm$ 1 mV). One possibility to explain this plateau are contaminations of the KCl salt with divalent ions. The certificate of analysis for the used KCl salt states upper limits for the content of divalent ions like Cu, Ni, Ca, Cd and Zn of 50 mg/kg. In the worst case, this corresponds to concentrations of 20–55 µM for each compound in a 600 mM KCl solution, or a total of 180 µM. It is obvious, if impurities of divalent ions are present in a $\sim$100 µM concentration, addition of 1 or 10 µM Ni_2^+ has negligible effect on the zeta potential. From the onset of the zeta potential decrease, we can thus possibly estimate an impurity content of $\sim$60 µM, caused by divalent ions.

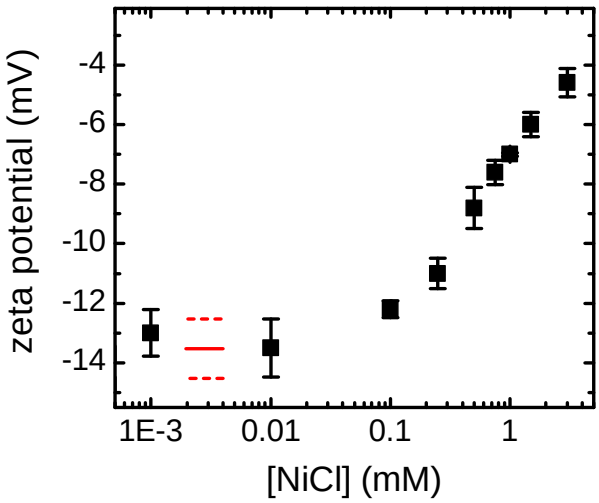

Figure 4.6: Dependence of zeta potential on $NiCl_2$ concentration in 600 mM KCl at pH 9.2.

Another interesting behavior of the zeta potential in nanopores is the time dependence of ζ_{pore} upon changes in solution pH. Figure 4.7 shows the equilibration of ζ_{pore} after the solution pH was changed from 10 to 4. ζ_{pore} changes rapidly from -24 to +5 mV within half an hour; subsequently, a small and slow increase to +8 mV is observed over 27 h. A similar behavior was described by Bousse et al. for planar Si_3N_4 surfaces[11], but no conclusive explanation could be given so far. Because the transport properties of Si_3N_4 pores may depend critically on the equilibration time after wetting the chip with fresh buffer solution, we employed a waiting time of at least 12 h during this work.

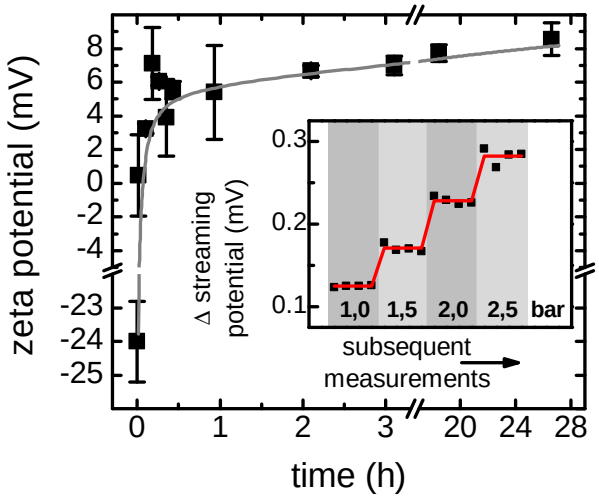

Figure 4.7: Time evolution of the zeta potential after changing the solution pH from 10 (t = 0) to 4 (t > 0). Error bars reflect variation of individual measurements. Inset: Representative streaming potential measurement in 400 mM KCl at pH 4. Red line depicts the mean value.

4.4. Protein translocations at different pH values

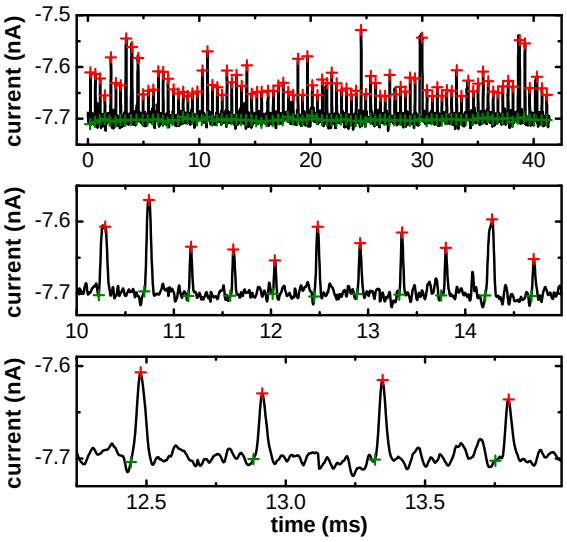

Figure 4.8: Current-time traces of avidin translocation events. Data between current blockades is removed for better visibility. Green and red crosses indicate peak on- and off-set, as evaluated with our custom Matlab routine.

To achieve a direct relation between pore zeta potential and protein translocation behavior, the same chip used for determination of EOF was subsequently employed for translocation experiments. Avidin was added to the measurement chamber on one side of the membrane (cis-side), which was electrically grounded. Positive or negative potentials (± 150 mV) were then applied to the other, trans-side of the membrane and the trans-pore ionic current was monitored over time. Spikes (pulses) in the current traces are attributed to proteins which pass through the pore lumen, thereby transiently blocking the current flow to some degree. Figure 4.8 shows exemplary translocation events with evaluated peak on- and off-set, but the blockade duration and height are not of primary interest in this chapter. A detailed description of peak evaluation is given by Pedone et al.[86]. Figure 4.9 shows avidin translocation experiments at varying solution pH. For pH 2, pH 6 and pH 8, the situation appears as intuitively expected: positively charged avidin molecules pass the pore only when the trans-side is negatively charged. While this behavior could – like in the case of DNA translocation experiments – be interpreted as electrophoretic transport, the situation is in fact more complex. At pH 10, we clearly observe translocations only when the trans-side is negatively biased; however, zeta potential measurements evidently show that at pH 10 avidin is negatively charged (cf. Fig. 4.1). Contrary to electrophoretic transport, the negatively charged proteins move through the pore towards the negatively charged electrode. Another most remarkable behavior is observed at pH 4: irrespective of the applied bias potentials, avidin translocates the pore as if electrokinetic transport was absent.

To explain these phenomena, we propose that the translocation behavior is governed by a conjoint action of electrophoresis, electroosmosis, and diffusion. Combining the equations for electrophoretic and electroosmotic transport (Eq. 3.6 and 3.8) yields an effective velocity v_{eff} of the protein inside the pore:

$$v_{eff} = v_{EP} + v_{EO} = \frac{\epsilon E}{\eta}(\zeta_{prot} - \zeta_{pore}). \tag{4.1}$$

Depending on the signs and relative magnitudes of ζ_{protein} and ζ_{pore}, respectively, electroosmosis may enhance or counteract electrophoresis.

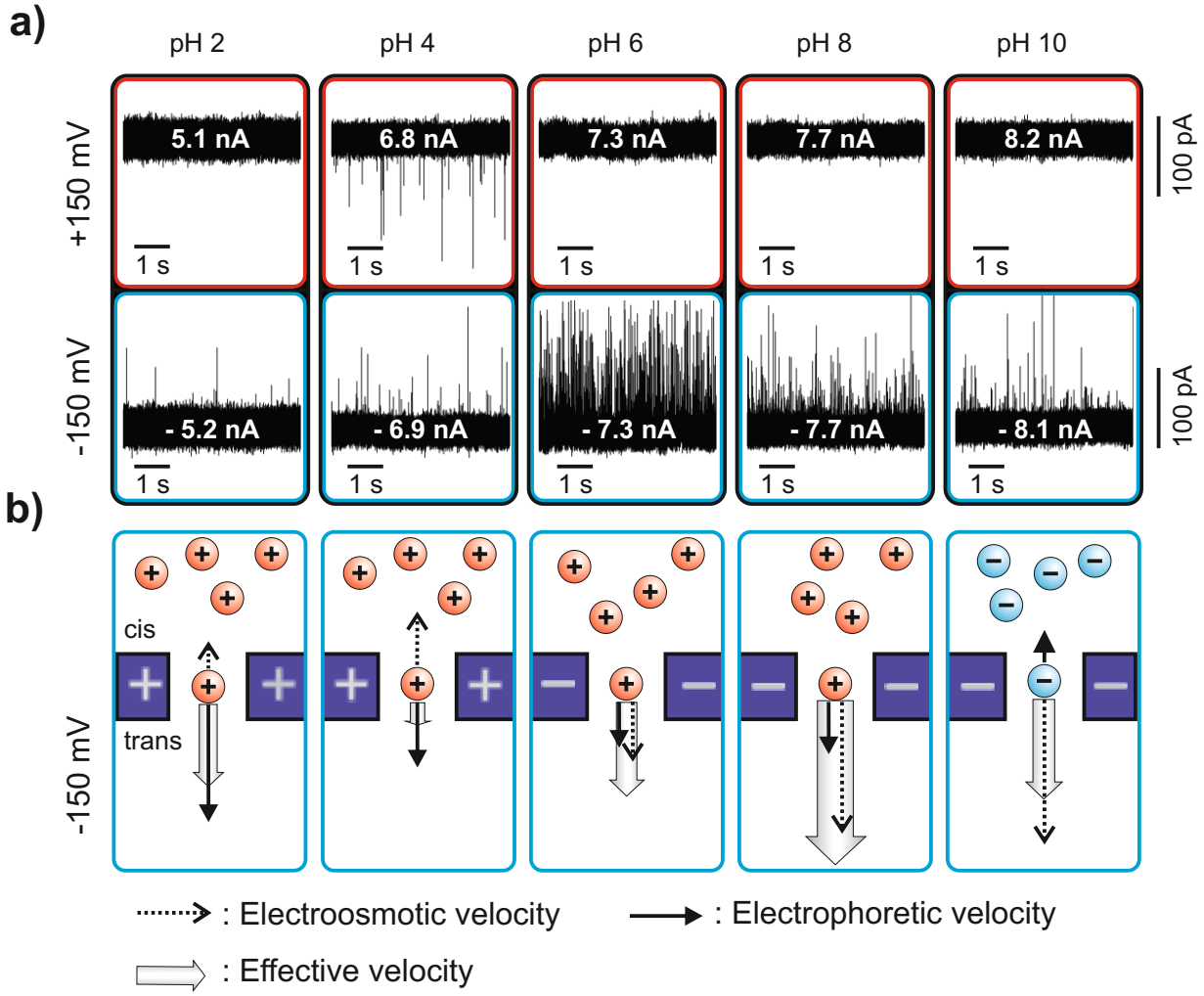

Figure 4.9: a) Current-time traces for positive (upper panel) and negative (lower panel) potential. White inscription indicates average open-pore current. **b)** Schematic illustration of protein and pore charge. The resulting electroosmotic and electrophoretic forces are indicated by arrows.

Table 4.1 summarizes the measured ζ-values and permits to rationalize the experimental observations: For pH 6 and pH 8, EO and EP are unidirectional (parallel) and therefore enhance each other. For pH 2, pH 4, and pH 10, EO-flow is directly opposed to the EP-movement (anti-parallel); yet, the different magnitudes of ζ_{protein} and ζ_{pore} for these pH values give rise to different situations. For pH 2, EO-flow weakens the EP-movement, but EP still dominates. For pH 10, EO clearly dominates over EP ($|\zeta_{\mathrm{pore}}| \gg |\zeta_{\mathrm{protein}}|$) and the resulting translocation direction is electroosmotic (anti-EP). Translocation events are only observed when the direction of the effective protein velocity in the pore is cis $\rightarrow$ trans, which (in case of the Si_3N_4/avidin system at hand) occurs for all the pH values mentioned above when the trans-side is biased negatively.

Table 4.1: Protein and pore zeta potentials and translocation event rates for varying pH.

		pH 2†	pH 4	pH 6	pH 8	pH 10
zeta potentials (at high ionic strength)						
ζ_{protein} (mV)[1]		18 ± 3	10 ± 3	7 ± 3	8 ± 3	-5 ± 3
ζ_{pore} (mV)[2]		4 ± 4	8 ± 2	-9 ± 2	-21 ± 2	-22 ± 2
$\Delta\zeta$ (mV)		$\sim$14	$\sim$2	$\sim$16	$\sim$29	$\sim$17
protein–pore interaction		rep.	rep.	attr.	attr.	rep.
event rate (s^{-1})	trans = -150 mV	2	6	90	40	15
	trans = +150 mV	0	5	0	0	0
τ_1 (µs)			17	23	14	15
τ_2 (µs)			80	81	51	57

[1] Measured in 50 mM KCl solution. [2] Measured in 400 mM KCl solution. † ζ_{pore} and event rates measured with a different Si_3N_4 pore.

In case of the pH value 4, the protein and pore zeta potentials are similar, $\zeta_{\mathrm{pore}} \approx \zeta_{\mathrm{protein}}$. Consequently, it is expected that EO-flow counterbalances EP transport, the effective velocity of the protein in the pore should vanish ($v_{\mathrm{eff}} \approx 0$), and electrically assisted transport of proteins across the pore does not occur. Remarkably though, we do observe translocation events, which notably do not depend on the direction of the applied bias. We attribute these events to diffusion of proteins through the pore, which is driven by the concentration gradient between the cis and the trans chamber.

Comparing the event rates measured at different pH values (see Table 1) we find that the highest event rates are observed at pH values for which EP and EO flow add up (pH 6 and pH 8). Then again we note that for these pH values – in contrast to pH 2, pH 4, and pH 10 – the electrical interaction between the pore walls and the protein is attractive, i.e., ζ_{pore} and ζ_{protein} feature opposite signs. We can only speculate whether this attraction might contribute to the observed high event rates, for instance by providing a "feeding" mechanism facilitating the collection of proteins from the volume close to the pore mouth, or by slowing the protein inside the pore. The latter effect would involve transient protein adsorption and result in longer sojourn times,

which in turn would enhance the detected event rate, as elucidated below. Figures 4.10 and 4.11 show event distribution plots which correlate the pulse width and pulse height. Two datasets are depicted which represent translocations that are driven by a combined action of EP & EO (pH 8) and translocations that are solely driven by EO flow (against EP, pH 10). Despite the different electrokinetic origin of the translocations, the event distributions are similar. In contrast to other reports from literature[33,111], we cannot identify several distinct clusters, but find a single pseudo cluster point instead. This pseudo cluster arises from short current pulses which are attenuated by the employed electronic filters (10 kHz four-pole Bessel). From a previous characterization of the time resolution of our setup[86] we can estimate for the present measurements that current pulses with durations < 20 µs will be attenuated to an extent that they cannot be identified by the pulse analysis routine anymore. However, it is likely that most of the proteins cross the pore very rapidly: assuming electrically driven transport with a net $\Delta\zeta$ of $\sim$10 mV and an applied voltage of 100 mV, v_{eff} becomes > 20 nm/µs in the pore, i.e., proteins pass the pore on a timescale of µs. On the other hand, the characteristic diffusion time of a protein across a nanopore is of the order of 10 µs (see Chap. 3.4, the diffusion coefficient of avidin determined by DLS is 64 $\mu m^2\, s^{-1}$). Hence it must be expected that most of the translocations without protein - pore interactions occur on an extremely short timescale and that only a fraction of the actually occurring events are recorded with adequate fidelity.

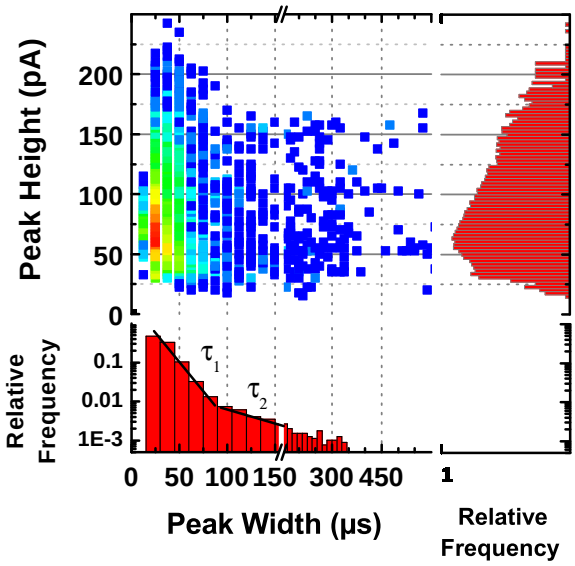

Figure 4.10: Color map plot and histograms of avidin translocation events at pH 8. Black lines in the event duration histogram indicate linear fits with time constants τ_1 and τ_2.

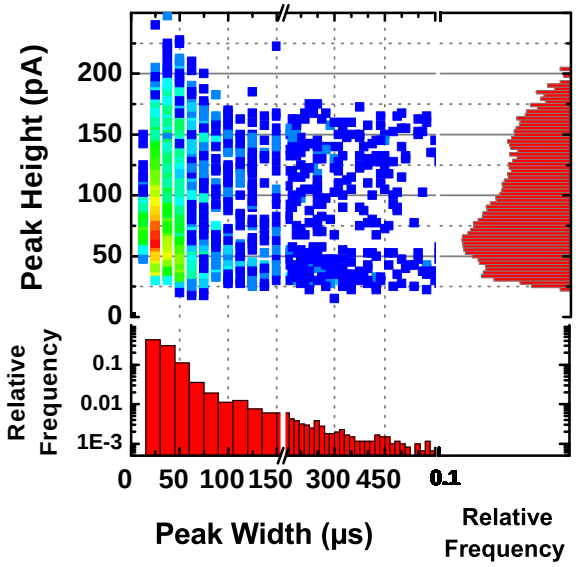

Figure 4.11: Color map plot and histograms of avidin translocation events at pH 10.

Having a closer look on the event duration histogram with a semi-log scale (Fig. 4.12), we clearly observe at least two different regimes to which we can attribute two time constants, τ_1 and τ_2. The vast majority of events is attributed to τ_1, namely 85% (pH 4), 80% (pH 6), 94% (pH 8) and 88% (pH 10). We thus concentrate only on this first regime.

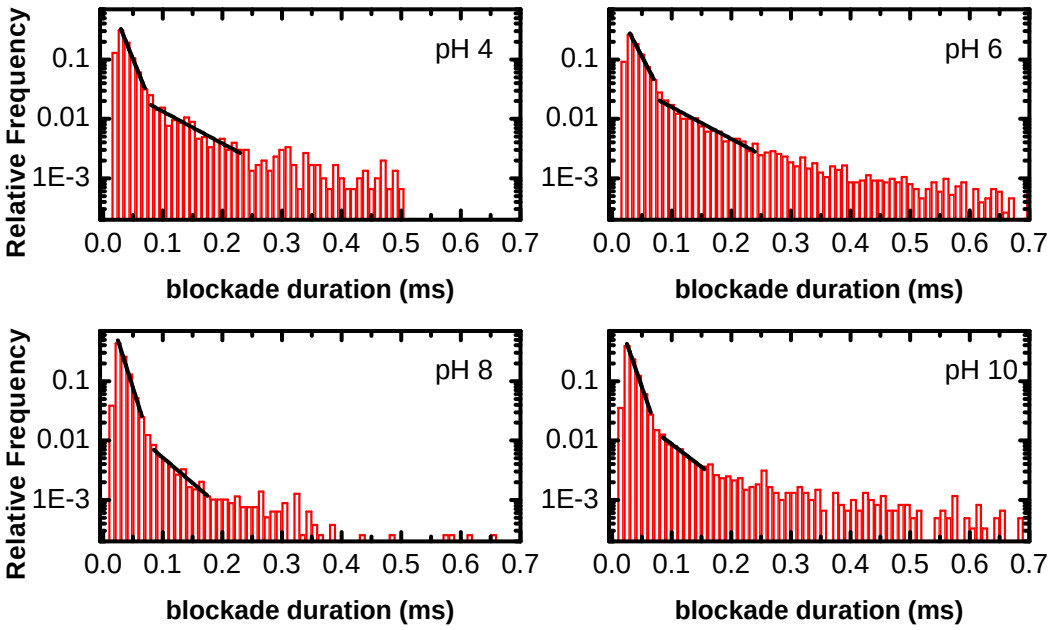

Figure 4.12: Time constants of avidin translocation events for different pH values at -150 mV. Black lines indicate linear fits in semi-log scale. Results are summarized in Tab. 4.1.

Results of linear fits are given in Tab. 4.1. An interesting relation between the time constants of different pH values should be mentioned. Between pH 6 and pH 8, protein and pore are oppositely charged. The translocation time τ_1 decreases from 23 µs (pH 6) to 14 µs (pH 8), a decrease by 40%. This could be explained by an increase of 81% in the effective velocity, represented by $\Delta\zeta$ (Tab. 4.1). If we assume $\tau \propto 1/\Delta\zeta$, as proposed by formula (3.12), the expected decrease in translocation time would be $(\tau_{\mathrm{pH6}} - \tau_{\mathrm{pH8}})/\tau_{\mathrm{pH6}} = 45\%$ – in good agreement with the experiment. However, this assumption is valid only for translocation without protein–pore interaction, where the translocation time is expected to be much faster, in the range of several µs. We therefore consider transient protein adsorption to be the mechanism determining the translocation time.

If the adsorption process would be purely electrostatic, we would expect that the translocation time at pH 8 is approximately twice as large than at pH 6, as calculated with Eq. (3.18). For this calculation, we approximate the attractive electrostatic interaction between protein and Debye layer with the expression given by Adamczyk et al.[1]:

$$F_d = 4\pi\kappa a\epsilon\zeta_{prot} \cdot \zeta_{pore} \cdot \frac{e^{-\kappa a H}}{1 + e^{-\kappa a H}} \tag{4.2}$$

where $H = y/a - 1$ is the dimensionless particle surface separation of a particle with radius a at position y above the surface. Assuming $E_a = F_d x$ for a distance $x = 0.1$ nm and that the pulling force in parallel to the surface has the same effect on desorption than a pulling force that would act perpendicular, the dissociation constant is proportional to the zeta potentials of protein and pore in the following way:

$$k_d(F) \propto e^{-|\zeta_{prot} \cdot \zeta_{pore}|} \cdot e^{|\Delta\zeta|} \tag{4.3}$$

As the product of zeta potentials is usually larger than their difference, adsorption time would always be dominated by the electrostatic interaction. What we observe experimentally is the opposite, namely a translocation time at pH 6 that is almost twice the time at pH 8. This inconsistency shows that electrostatic interaction can not be the dominating adsorption mechanism, yet this finding is not unexpected, because hydrophobic interactions are also likely to be involved, as well as hydrodynamic interactions, once the protein disturbs the Debye layer on the pore surface[1,28,123]. The occurrence of multiple adsorption mechanisms is supported further by the similar translocation times of all pH values, despite the fact that the average electrostatic protein–pore interaction is repulsive at pH 4 and 10. As reported by Arai at al., proteins adsorb on hydrophobic interfaces regardless of the charging state of protein and surface[6].
Because proteins are complicated structures, both chemically and geometrically, we are not able to elucidate details on the adsorption mechanism in the present work. However, from this first example we can already state that adsorption is dominated by other forces than electrostatic interaction, and that the pulling force (in this case the EOF), influences the adsorption time.

The event rate between pH 6 and 8 also shows an interesting behavior. Despite an increase in mass flow through the pore due to the stronger EOF, the event rate is reduced at pH 8 by 55%. This can only be explained by an interplay between the limited time resolution of our setup and the adsorption mechanism. With increasing velocity of translocating proteins, the probability for adsorption will decrease and thus the event rate will decrease. The same effect is observed at fixed pH, once we increase the applied potential. As shown in Fig. 4.13, the event rate at pH 8 and pH 10 decreases linearly from -100 mV on. At pH 6, the decrease starts at -150 mV owing to the smaller $\Delta\zeta$.

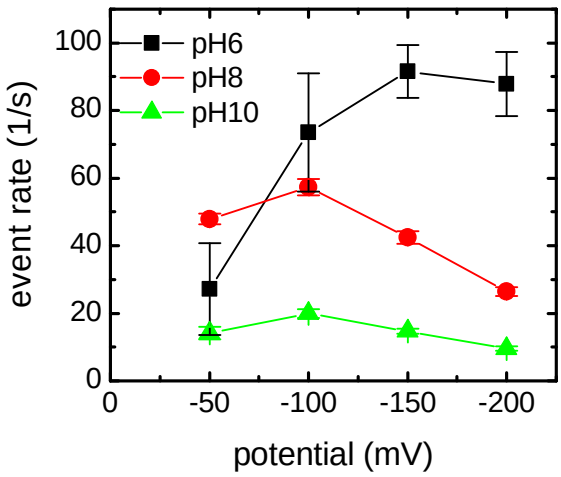

Figure 4.13: Potential dependent event rate of avidin translocation experiments at different pH.

Although electrostatic interaction plays a less significant role in the adsorption process, we can not neglect it completely. This can be seen at pH 10, where the electrostatic interaction is repulsive and the event rate as well as the translocation time is decreased even further, despite the similar effective velocity compared to pH 6. As already mentioned, this finding supports the idea of a feeding mechanism for attractive interaction, but a repelling mechanism for repulsive interaction. We understand this feeding mechanism as a trigger for adsorption. For pH 6 and 10, the protein is attracted towards the pore surface by long range electrostatic interaction, but the adsorption itself also involves hydrophobic and hydrodynamic interactions[1,6,123]. For the other pH values, the overall electrostatic interaction is repulsive, but nevertheless some proteins hit the pore surface at a reduced rate and undergo a similar adsorption mechanism than for pH 6 and 8.

The second regime, τ_2, shows the same qualitative progression with pH as τ_1, but is approximately four times slower. We can only speculate if these events are caused by multiple adsorption processes, or by partly unfolded molecules, leading to higher surface affinity.

4.5. Conclusion

The results clearly show that EO effects have a major influence on the translocation of moderately charged nano-objects through nano-scale orifices. For small globular objects like proteins (as opposed to long DNA molecules which normally do not fit through the pore in a coiled state), diffusion in a concentration gradient can also be an efficient mechanism to facilitate directed translocation, in particular when electrokinetic effects cancel each other out.
The electrically assisted translocation direction and rate of proteins through nanopores is governed by EP and EO forces. Acting in concert, EO can enhance EP transport, but, depending on the zeta potential difference, EO flow may counteract EP and consequently suppress or even reverse EP transport. Our experimental findings were recently supported by theoretical calculations of Jubery et al., where the translocation behavior of high-density lipoprotein and low-density lipoprotein was simulated in dependence of the pore surface charge[50]. Our results further indicate that transient protein adsorption is a necessary effect in short nanopores to detect proteins by slowing them down to a timescale above the time resolution of the measurement system. The translocation time is not only determined by the effective force on a free protein ($\Delta\zeta$), but also on the kind of protein–pore interaction. As a consequence for future nanopore experiments we conclude that the surface charge on the inner pore walls must be carefully controlled when conducting experiments with proteins and that the charging state of protein and pore must be accounted for in the interpretation of protein translocation events.

5. Towards Single Proteasome Trapping

5.1. Introduction

The 20S proteasome is a large (700 kDa) protein complex, located in the nucleus and cytoplasm of each cell in large ($10^5 - 10^6$) numbers[89]. It is under steady and intense investigation because it regulates several important cell functions by degrading old, misfolded or excess proteins. Albeit the individual proteasome structure differs between organisms, they all have in common the barrel shaped structure, composed of two inner rings (each 7 β-subunits) and two outer rings (each 7 α-subunits), as depicted in Fig. 5.1. In the proteasome from archaea *Thermoplasma acidophilum*, which is seen as a kind of "ur-proteasome"[136], all α and β subunits are identical and the four heptameric rings form two antechambers and one central chamber, which are connected by small $\sim$2.2 nm wide constrictions[66]. Upon incorporation of a peptide substrate to the central chamber, it is cleaved unspecifically in smaller peptide fragments of 6–9 amino acids at proteolytically active sites (N-terminal threonine)[66,127].

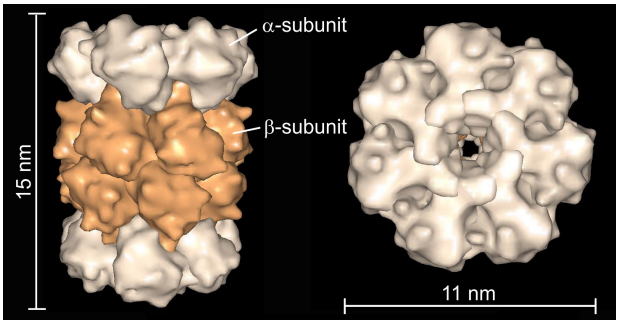

Figure 5.1: Surface plot of 20S proteasome from *T. Acidophilum*. From the RCSB PDB (www.pdb.org) of PDB ID 1PMA (Löwe et al. (1995) Science 268: 533-539).

As summarized in a review by Borissenko and Groll (2007)[10], the proteasome is involved in cell cycle control, apoptosis, induction of heat shock response, transcription activation and inhibition of antigen presentation. It has potential applications in anticancer therapy[18], is involved in neurodegeneration processes following an ischemic stroke[57], shows anti-inflammatory and anti-viral effects[82] and has potential to fight the tuberculosis bacterium[64]. Proteasome function is manipulated by inhibitor substances which can act temporarily or permanently. Usually, large

screenings with different substances have to be carried out in order to find a suitable inhibitor for a certain organism, i.e. to affect bacterial but not human proteasome function or to affect only cancerous cells.

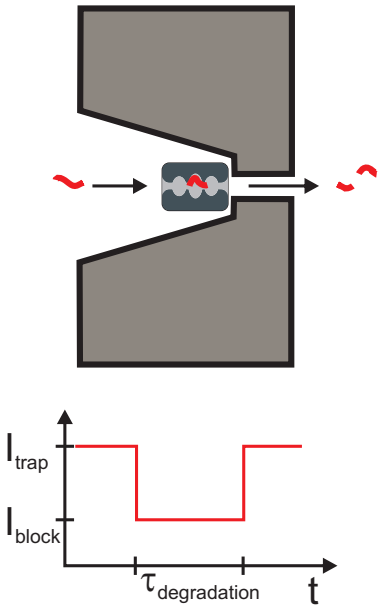

Figure 5.2: Trapping of a proteasome molecule and degradation of a polypeptide.

Solid-state nanopores open up new ways of investigating proteasome function and structure on a single molecule level. Especially the incorporation and degradation of polypeptides may be studied in real-time for a single proteasome as depicted schematically in Fig. 5.2. To this end, a proteasome molecule has to be trapped inside a nanopore and the noise level has to be sufficiently low to observe blockage of the proteasome cavities. In this thesis we develop a proof of concept and show the reversible trapping of proteasome molecules by a pit-pore device as described in Chap. 2.3 and depicted schematically in Fig. 5.2. After trapping of a single proteasome molecule, the ionic current is reduced to I_{trap}. If a polypeptide enters the proteasome cavities, the ionic current is further decreased to I_{block}, where the relative current blockade will depend on the pit-pore geometry. From the duration of the current blockade $\tau_{degradation}$, information of the proteasome–peptide interaction may be derived.

To obtain a complete picture of proteasome behavior in solid-state nanopores, we will study the translocation behavior of proteasome molecules through nanopores without the pit-pore structure in a first step. Afterwards, we show trapping of single proteasome molecules in a pit-pore device and observe promising indications of peptide incorporation in the proteasome.

5.2. Proteasome translocation through solid-state nanopores

In this section, translocations of proteasome molecules through 18–25 nm wide Si_3N_4 nanopores show that the proteins cross the pore in direction of the EO flow and against the electric field, indicating low zeta potential of the molecule. A so far unknown observation are step-like current blockades, which are reported here in detail. We explain this behavior by transient adsorption on the nanopore wall, supported by the conical pore shape and depending on the pore diameter.

5.2.1. Transient proteasome adsorption

Proteasome for all experiments was kindly provided by the group of Prof. Dr. Robert Tampé, Institute of Biochemistry, Frankfurt a. M., Germany. The protein from *Thermoplasma acidophilum* was expressed in E-coli and His_6-tagged on the β-subunits[113]. The buffer solution contained 600 mM KCl, 30 mM Tris-HCl pH 9.1 and 0.4 mM EDTA to prevent proteasome from capturing free divalent ions. The initial diameter[1] of the pore was 22 nm, as determined by the measured ionic resistance and also confirmed by TEM. Fig. 5.3 shows TEM micrographs of three different pores used for translocation experiments. Due to the excellent signal-to-noise ratio, we could set the Bessel-filter to 100 kHz, which gives a filter risetime[93] of 3.3 µs. This is below the sample rate of 250 kHz and gives a reliable time resolution below 10 µs, taking one sample point as uncertainty. A power spectrum of the ionic current at 200 mV is given in Fig. 5.4 together with a TEM image of the pore. For comparison, a second power spectrum from a current-time trace recorded at 50 kHz is shown (red curve).

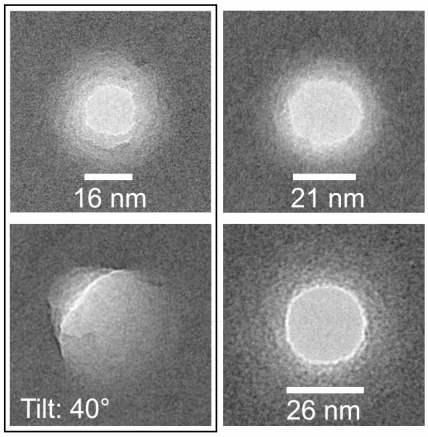

Figure 5.3: Left: TEM image of the 18 nm pore, described in section 5.2.1. Right, top: TEM image of the pore used in section 5.2.1. Right, down: TEM image of the largest pore used for translocation experiments.

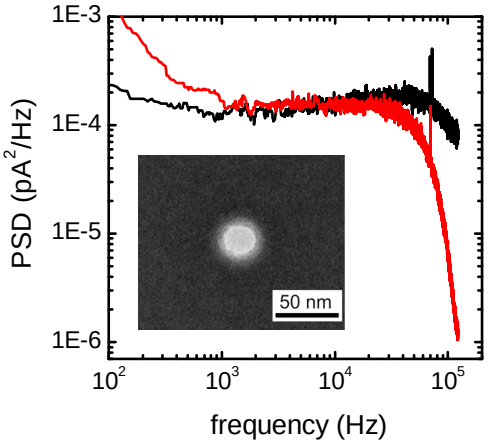

Figure 5.4: Power spectral density of two different nanopores, extracted from a current-time trace of 1 s at an applied voltage of 200 mV. f_c =50 kHz (red curve) and f_c =100 kHz (black curve), f_s = 250 kHz. To improve visibility, the original PSD was downsampled by factor of 5 and smoothed with a 20 points percentile filter. Inset: TEM image of the nanopore corresponding to the black curve, 22 nm diameter, the pale ring indicates the conical pore shape.

After adding proteasome to a final concentration of 5 nM to the cis-side of the measurement chamber, a voltage of -200 mV is applied to the trans-side. Clear current blockade events are observed in the current-time trace, as depicted in Fig. 5.5 a). Upon reversal of the applied voltage (Fig. 5.5 b)), no events are observed. This suggests the electroosmotic flow being the dominat-

[1] We observed in our experiments a slight increase in conductance over a timescale of days. This conductance increase is attributed to ablation of Si_3N_4, leading to an increase in pore diameter of typically 1–3 nm

ing transport mechanism, as proteasome has a pI of 5–6 and is thus negatively charged at our measurement conditions[136]. For simplicity, the term "current blockade event" will be shortened to "blockade event" or "event" further on. Having a closer look on the events in Fig. 5.5 c), we observe a fine structure featuring several levels, which is not reported in literature on protein translocations so far.

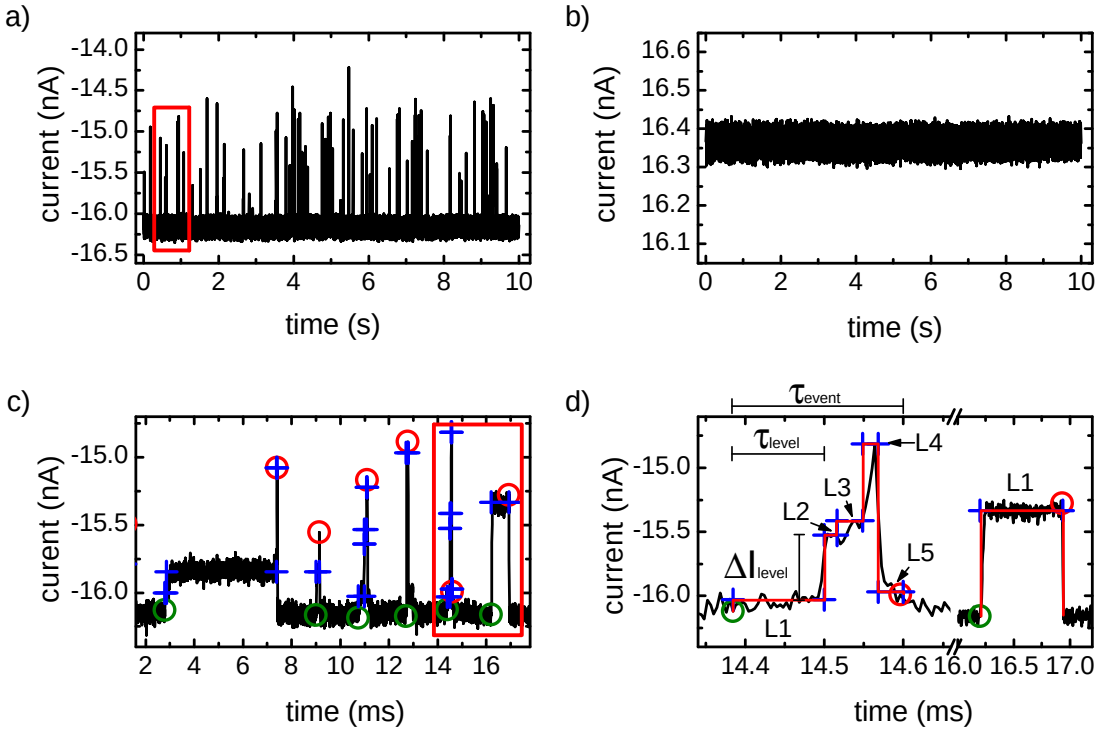

Figure 5.5: a) Current-time trace of 5 nM proteasome, -200 mV, $f_c = 100$ kHz. **b)** Reference measurement at +200 mV. **c)** Zoom of the marked area in a), baseline between the peaks is removed for better visibility. Green and red circles mark peak-on and -off, blue crosses mark level-on and -off. **d)** Zoom of the marked area in c). Solid lines represent evaluation of current levels by a matlab routine. Green and red circle are peak-on and -off. L1, L2, ... denotes the level number. It should be noted that modelling of the conductance blockades is limited to the employed filter and sample rate. Especially for L4 of the first event the duration is probably overestimated[85,86].

In contrast to the avidin translocations reported in Chap. 4, where the blockade events could be described by duration and height, the detailed structure of proteasome translocation events gives rise to additional parameters. With these parameters, we describe the level structure of each event individually, as depicted in Fig. 5.5 d). Each of the levels L1 to L5 for the first event is characterized by a constant current blockade ΔI_{level} which refers to the baseline and lasts for a time τ_{level}. The second event consists of only one level, L1. Usually, the blockade height as well as the number of levels varies between different events. As will become clear later, they are statistically distributed on a range determined by the pore geometry. For a complete characteri-

zation of proteasome translocation events, we analyze the blockade events by a custom Matlab routine and evaluate the event duration τ_{event} and mean blockade height $\Delta\bar{I}_{event}$, as well as the level duration τ_{level} and level height ΔI_{level} for all levels of each event. (Details on event evaluation can be found in Appendix B). From this information, further characteristic figures can be derived: The number of levels in an event, the distribution of level durations and level heights, the sequence of blockades and the position of the maximum current blockade in the event level structure. Current blockades are usually evaluated as change in current compared to the open pore current, i.e. % current blockade, which is equal to a relative conductance blockade and independent of the applied voltage. To emphasize the voltage independence, we usually use the expression conductance blockade further on.

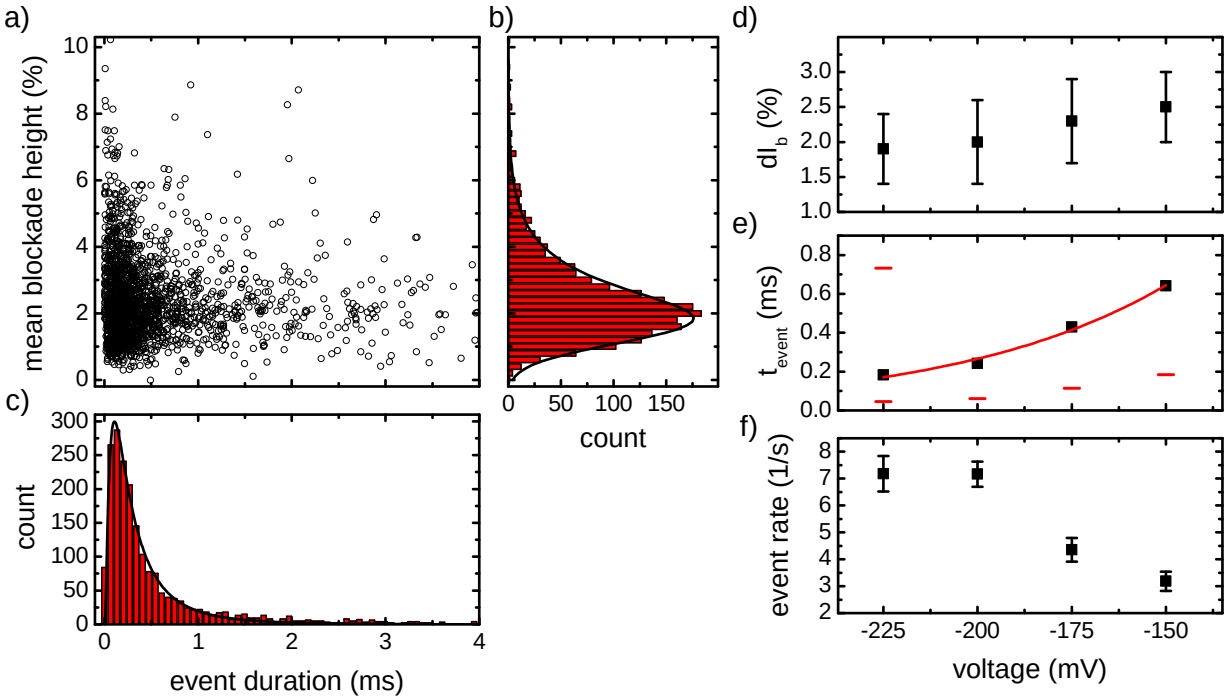

Figure 5.6: a) Scatter plot of proteasome translocations, pH 9.1, -200 mV. **b)** Histogram of mean conductance blockade height. The solid line represents a modified Gaussian fit to the data. **c)** Histogram of event duration. The solid line represents a lognormal distribution fit to the data. **d)** Mean conductance blockade for different voltages. **e)** Median event duration. Red bars indicate the standard deviation. **f)** Event rate of 5 nM proteasome.

We begin our analysis of translocation events with properties of the whole event: duration, mean conductance blockade and event rate. Due to the multi-level structure, averaging over all levels of an event is an appropriate method for its characterization. Figure 5.6 a) shows a scatter plot of the event duration and mean conductance blockade at -200 mV. The mean conductance blockade is calculated by dividing the area of blocked current by the event duration. The majority of events

blocks an average of 1–3% for a duration of 100–500 µs. The histogram of the average blockade height in Fig. 5.6 b) shows a modified Gaussian distribution with a mean current blockade of 2%. For cylindrical pores, the blockade height is usually Gaussian distributed. In our case, as will be explained in more detail in this chapter, the conical pore shape gives rise to a position dependent blockade height, which modifies the statistical, Gaussian behavior and leads to a skew of the Gaussian distribution towards smaller blockade values.
The event duration shown in Fig. 5.6 c) also shows a skew towards smaller blockade times. In this case, however, the total blockade time consists of several subsequent adsorption processes and thus the final probability distribution depends in a multiplicative way on the sub processes. The result is a logarithmic normal distribution, which is also described in more detail by Limpert et al.[63]. The event duration has a median duration of 242 $\cdot/$ 3.9 µs. The symbol $\cdot/$ is spoken "times divided" and $\sigma = 3.9$ represents the multiplicative standard deviation or variance of the system. This means that 68.3% of the values are in the interval 62–944 µs. For fitting the data to the probability distribution, the formula

$$P(\tau) = \frac{A}{\sqrt{2\,\pi}\,s\,\tau}\,e^{\frac{-(ln\tau - m)^2}{2\,s^2}} \tag{5.1}$$

was used. The median value μ and the multiplicative standard deviation σ are then defined by $\mu = e^m$ and $\sigma = e^s$.
Upon changing the applied potential, the step-like blockade behavior is preserved, but the blockade duration gets shorter. The blockade height increases with increasing potential as expected according to Ohm's law. After dividing the blockade height by the applied voltage, the resulting conductance should be independent of the applied voltage. This is confirmed by the data shown in Fig. 5.6 d), where the mean conductance blockade for different applied voltages is depicted. It decreases only slightly with increasing potential and is at $2.2 \pm 0.3\%$ for all voltages.
Figure 5.6 e) shows the median event duration. It decreases non-linear between -150 and -225 mV from 640 to 183 µs. The red bars display the range of σ, which does not fit the scale for all points, but is given in Tab. 5.1 together with other event data from the 22 nm chip. The red line depicts an exponential fit for an adsorption dominated translocation process, as mentioned in Chap. 3.4.2. The fit parameters of the function $\mathrm{f(V)} = \mathrm{A} \cdot \exp(\mathrm{V}/\mathrm{V_c})$ are $\mathrm{A} = 9.2 \pm 2$ ms and $\mathrm{V_c} = 56 \pm 4$ mV.
The event rate is given in Fig. 5.6 f) and increases with the applied potential between -150 and -200 mV. The saturation between -200 and -225 mV is difficult to explain. One possibility is the limited time resolution: if the level duration decreases towards the time resolution of the system, a fraction of the events will be too short and thus missed by the detection routine[86]. However, the average level duration at -225 mV is 36 µs, which can be resolved with the employed filter. Another possibility related to time resolution is the probability for adsorption. This probability will decrease with increasing driving force inside the pore[109]. Obviously, if the adsorption time is shifted below the time resolution – or if the combination of pore length, drift velocity (free translocation) and diffusion towards the pore wall is impeding protein adsorption at all – the event rate will be decreased. The third possibility is a diffusion limited capture process. This was investigated by Wanunu et al. for DNA molecules[122]. In this model, the rate has a linear

dependence on the applied voltage, because the electric field expands on a hemisphere around the pore entrance and capturing of molecules is governed by the drift velocity in this hemisphere. In our case, however, the driving force is not of EP nature. The molecules are forced through the pore by the EO flow, and the observed limiting effect on the event rate might therefore be explained by a limited EO flow due to hydrodynamic effects on the nanometer scale at high electric field.

As mentioned at the beginning, the surprising feature of the observed proteasome translocations is the level structure, which we attribute to multiple transient adsorption processes of proteasome molecules on the nanopore wall. This is shown schematically in Fig. 5.7 together with the expected current-time signal. Depending on the position of adsorption, the molecule blocks a certain ionic current, resulting in a characteristic step profile of the current blockade.

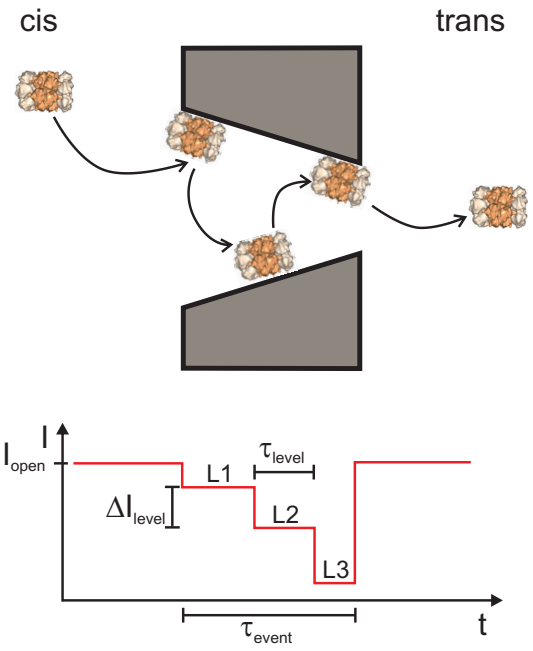

Figure 5.7: Proteasome translocation process with transient adsorption steps.

In the following paragraphs we will analyze the proteasome blockade data in more detail and argue for the plausibility of the transient adsorption hypothesis. Having a closer look on the current blockades, we can evaluate the level structure for the level duration and height as shown in Fig. 5.5 d) and Fig. 5.7. A colormap plot of the data obtained at -200 mV is shown in Fig. 5.8 a) together with histograms of level duration and blockade height. A uniform lognormal distribution of the level duration is observed, comparable to the event duration but with shorter times, Fig. 5.8 b). The blockade height histogram in Fig. 5.8 c) shows a clear peak at 1% and a second broad one and not very pronounced at 8%. In between these peaks, the distribution decreases almost linearly. The relation between level height and duration is indicated by the grey line in the scatter plot. It shows the average level duration in dependence of the conductance blockade (the shown curve is a 9-point adjacent averaging of the original data). Obviously, the average duration is largest around 2% (∼200 µs) and then decreases for increasing blockade heights to 35 µs. As will become evident in the course of this chapter, the short and large conductance blockades correspond to adsorption points at the small end of the conical pore, whereas the small and long lasting levels correspond to adsorption points near the pore entrance.

Figure 5.8 d) shows blockade height histograms for different voltages, which are normalized to the number of events recorded at each voltage. Only at -150 mV, two more pronounced peaks at 3.3 and 4.7% are visible. The distribution at 8% flattens out with increasing voltage, which we attribute to an increased drag on the molecule at the narrow end of the pore, thus decreasing the

probability of adsorption. The large peak at small blockade values as well as the largest observed blockades are similar for all voltages as expected for conductance values.
Figure 5.8 e) shows the median value of a lognormal fit to the level duration data. Between -150 and -225 mV, the level duration decreases from 87 to 36 µs and shows a broad distribution between very small and large blockade times (∼10–800 µs) . In Fact, if transient protein adsorption is considered to be the time determining mechanism of the translocation process, broad time distributions are also observed and reported by others[83,90,111,124].

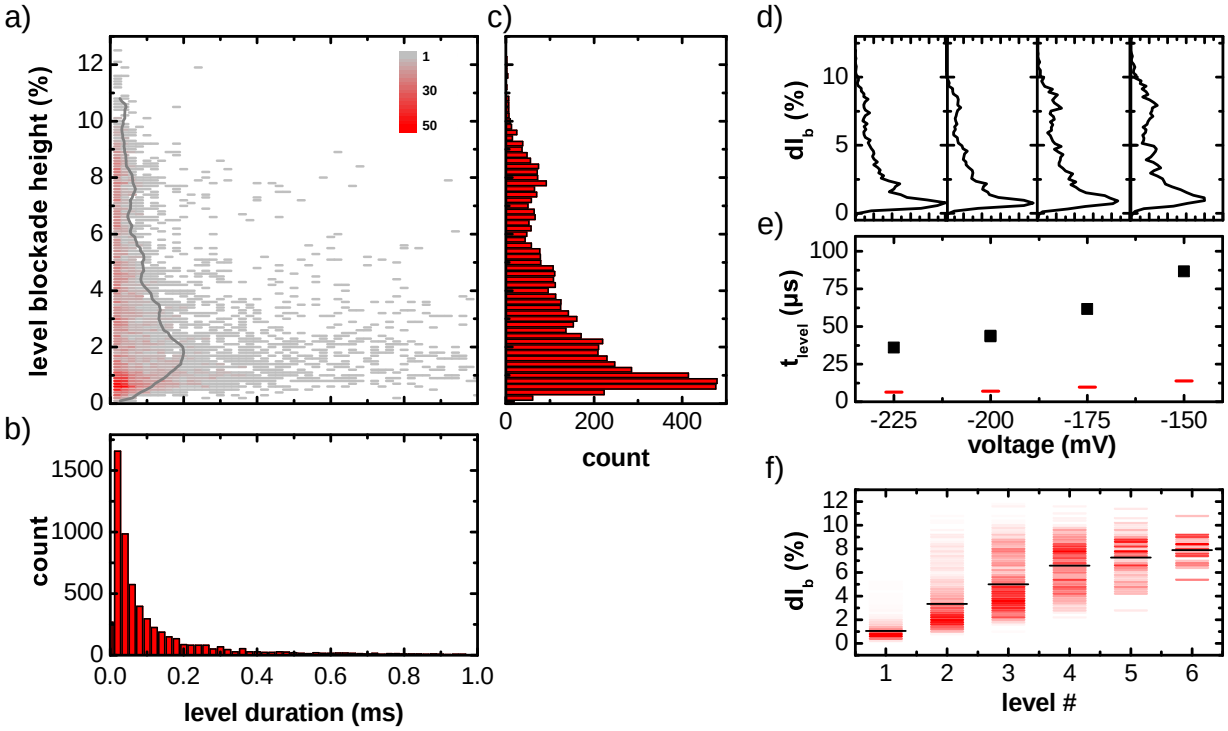

Figure 5.8: a) Color map plot of proteasome translocations, pH 9.1, -200 mV. Red color represents 55 counts. **b)** Histogram of level conductance blockades. Binning of 0.2% corresponds to 33 pA. **c)** Histogram of event duration. **d)** Conductance blockade histograms for different voltages. **e)** Median level duration. Red bars indicate the standard deviation. **f)** Distribution of conductance blockades separated for subsequent levels in an event.

Figure 5.8 f) shows a color mapped distribution of blockade heights according to the level number within a single event (see Fig. 5.5 d)) – not to be confused with the number of levels – for all events recorded at -200 mV. It can thus be interpreted as an average blockade shape. The highest plotted level number is 6, as there are only two events with more than 6 levels. Even the number of 6-level-events is very low (30). Black bars give the average conductance blockade at the respective level. It shows that successive blockade levels block an increasing amount of current, which we attribute to the conical pore shape. This explanation is justified by a simulation of the position dependent proteasome conductance blockade, presented in Fig. 5.9.

For this simulation, we first determine the exact pore diameter by fitting the diameter to the open pore resistance according to Eq. (3.25).
A TEM micrograph of the pore agrees very well with the so calculated pore geometry, see Fig. 5.3 and Tab. 5.2. In the second step, the current blockade of a cylindrical particle is calculated for different positions inside the conical pore, as explained in the theory section 3.6. For better comparison with the experimental data, we plotted the independent variable on the vertical axis in Fig. 5.9. Obviously, the largest theoretically expected conductance blockade is around 9%, which agrees very well with the experimental observation. This finding is a strong evidence that the observed level structure is caused by transient protein adsorption.

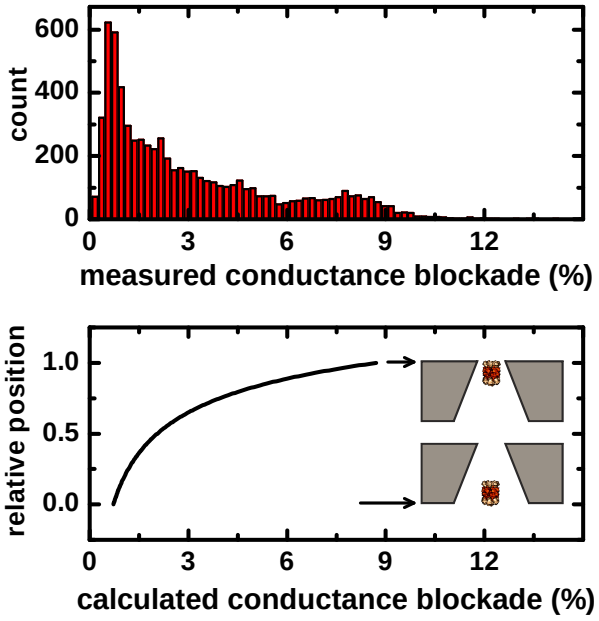

Figure 5.9: Top: Histogram of experimental conductance blockade for all events at -200 mV. Bottom: Calculated conductance blockade in dependence of the proteasome position inside the nanopore.

To complete the characterization of proteasome translocation events, we investigate statistical properties of the level structure. The left side of Fig. 5.10 shows the probability of the number of levels per event for different applied potentials. All distributions are quite similar with a most probable number of 2–4 levels per event. For increasing potential, the distribution shifts slightly to the left, i.e. from an average of 3.3 levels/event (-150 mV) to 2.7 levels/event (-200 mV) as determined by Gaussian fits. This is expected if we consider protein adsorption; the probability for adsorption decreases with increasing external potential. On the right side of Fig. 5.10, the conductance blockade distribution for the first three levels of the events is shown for different voltages. Here, only events with increasing blockade levels are considered. We do this, because one might argue that the protein does not translocate, but diffuses out of the pore again, if an event shows also decreasing blockade levels. Even if we know that the average blockade shape shows increasing blockade levels (Fig. 5.8 f)), we see no possibility to clearly decide about this problem. We therefore state that events with increasing levels only are most likely due to successful translocations through the pore. The fraction of this kind of events on the total evaluated events is 71% for -150 and -175 mV, 78% for -200 mV and 80% for -225 mV. The black lines on the right side of Fig. 5.10 correspond to the first blockade level with a clear maximum between 0.5 and 1% conductance blockade. Almost no first level is found above 2%. The second level, represented by red lines, is shifted to the right with a maximum frequency at 2% and a broad distribution towards larger blockades of up to 9%. The third level is represented by blue lines and is broadly distributed between 2 and 10%. It dominates the second level from 4% on. Compared

to the theoretical curve of adsorption position and conductance blockade shown in Fig. 5.9, we can interpret the first level as an adsorption within the first quarter of pore length. The second level corresponds to an adsorption within two thirds of the pore length with a maximum at half the pore length and the third level corresponds to an adsorption point within the second half of the pore length.

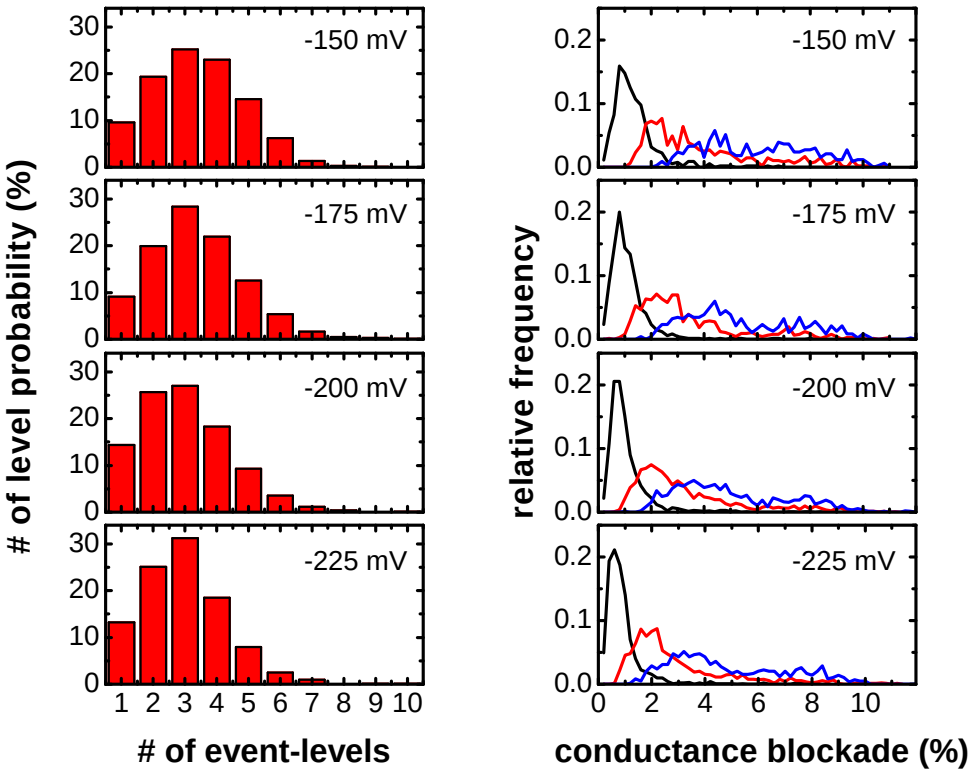

Figure 5.10: Left: Probability for a certain number of levels inside an event. Right: Histograms of conductance blockades for the first three levels. Black, red and blue lines correspond to the first, second and third level.

Similar results as the ones shown above are also found for other nanopores with different dimensions. All pores exhibit the step-like conductance blockades, whereas for the largest one (28 nm diameter) and also for the smallest one (17 nm diameter) the number of levels per event is significantly decreased compared to the intermediate pores (18–22 nm), as shown in Fig. 5.11. Furthermore, the probability for one-level events is increased from 5–15% for the smaller pores to 35% for the largest pore. We attribute this increase in one-level-events to a decreasing probability for adsorption if the pore diameter is enlarged.
All pores have in common the most probable blockade height, in the range between 0.3–0.6% with a decreasing frequency for higher blockades as shown on the left side of Fig. 5.12. A slight and broad peak is found at higher blockade values of 9% ($D_p = 17$ nm), 8% ($D_p = 22$ nm) and 2% ($D_p = 28$ nm). The number of recorded events used for this evaluation is smallest for the chip with 17 nm (394 events), in contrast to to the chip with 18 nm (1050 events), with 22 nm (2047 events) and with 28 nm (1864 events). The 18 nm chip shows distinct blockade levels, which we attribute to a contaminant at the pore entrance, favoring adsorption at distinct positions. The measurement of this effect will be explained in a separate section on page 53 in more detail.

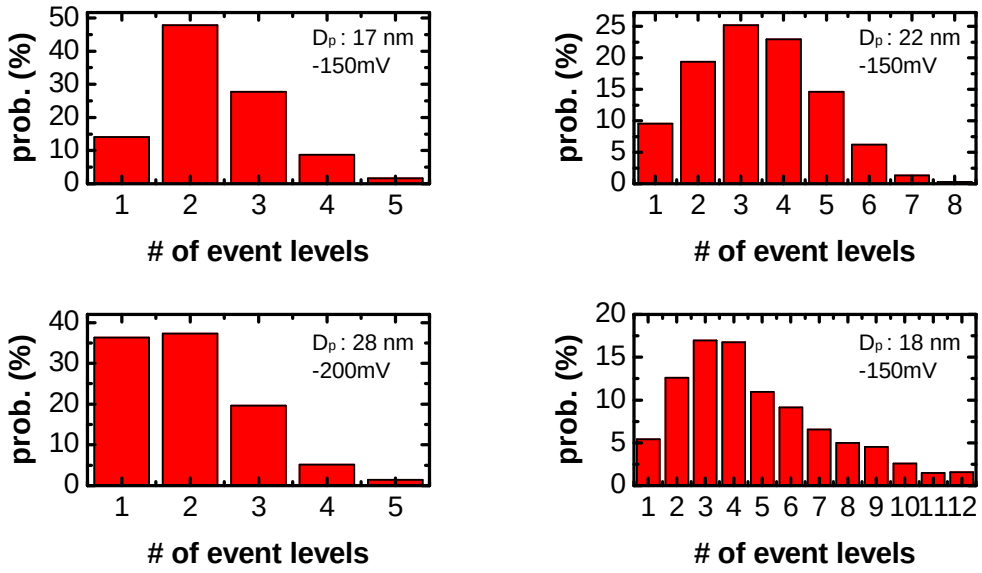

Figure 5.11: Level probability histograms for different nanopores, as denominated in the particular graph.

The differences in the maximum conductance blockade might look strange at first sight. It can, however, be excellently explained by the pore geometry, as we show by calculating the conductance blockade of a proteasome molecule for the different pore geometries. As already mentioned before, the pore diameter used in the calculation is determined by fitting the diameter to the open pore resistance, which is in accordance with TEM micrographs (Fig. 5.3 and Tab. 5.2). The results of these calculations are in excellent agreement with the observed values. As shown on the right side of Fig. 5.12, we expect a blockade range of 0.8–16% for the 17 nm chip and we

observe blockades up to around 15%. For the 22 nm chip, we expect blockades between 0.7 and 9% and the observed values reach up to 10%. For the 28 nm chip, blockades between 0.6 and 5% are expected and we observe events up to 5%. Also for the 18 nm chip, we expect blockades up to 15%, which is essentially what we measure.

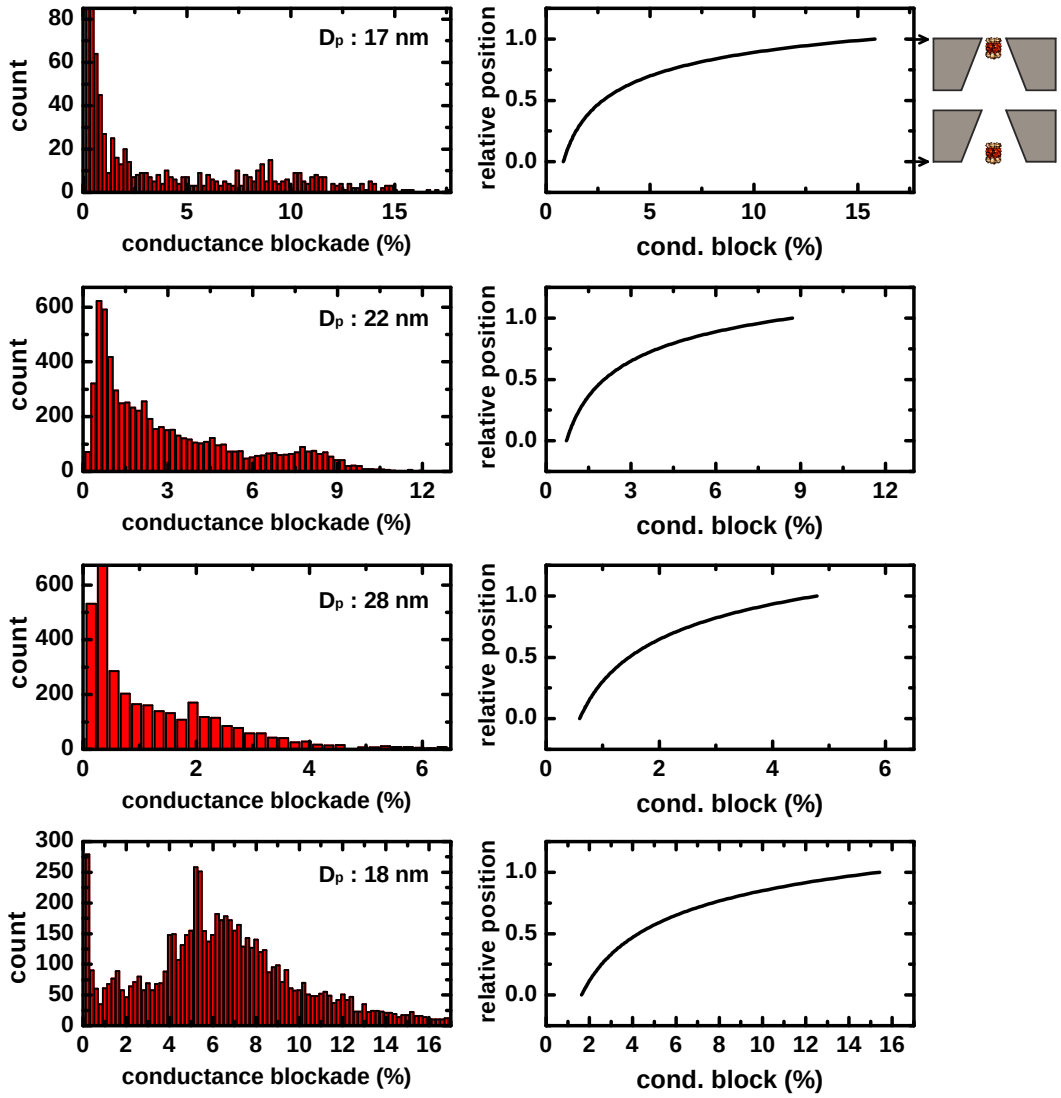

Figure 5.12: Left: Conductance blockade level histograms of pores with different diameters, as indicated. Right: The respective simulation of proteasome position dependent conductance blockade. According to the pore geometry, the expected range of conductance blockades differs between the pores, which is well resembled by the experimental data on the left.

Finally, we compare all event and level durations as shown in Fig. 5.13 on a semi-logarithmic scale. Only the 22 nm chip shows a continuous exponential relationship between event / level duration and the applied voltage (black squares). The 28 nm chip has an event duration on a similar timescale as the aforementioned, but only between -200 and -300 mV. The decreased duration at -150 mV can not be explained (red pale circle). The only difference is the few recorded events in contrast to the other voltages, see Tab. 5.1. An interesting difference between the 22 nm and the 28 nm chip is found in the level duration. The level duration of the 28 nm chip is approximately doubled compared to the 22 nm chip. We explain this effect by the decreased external forces acting during adsorption in the larger pore. For the event duration, however, the increased level duration cancels out with the smaller number of adsorptions per event; also an effect of the larger pore diameter. Both effects lead to similar event durations for both pores.
The single value obtained for the level duration and also for the event duration of the 17 nm chip (green triangle) is much smaller than all the others. In this case, it is likely that the 17 nm chip is too small for proteasome translocations. The proteasome molecule is barrel shaped with a diameter of 11 nm and a length of 15 nm. Thus, the diagonal distance is 18.6 nm. For translocation, the molecule would have to be aligned uniaxially with the nanopore. The probability distribution of the molecule orientation in front of the pore entrance therefore determines if it translocates, or if it is repelled. In the last case, we would observe short bumping events[90], which would explain the short observed event and level duration.
The 18 nm chip, despite the unusual translocation behavior, fits also in the regime of the 22 and 28 nm chip for -50 to -150 mV (blue downward triangles). From -150 to -200 mV, the event duration increases by 225%, which can only be explained partly by the increase of 23% in level duration. The most striking difference is the increasing number of levels, accounting for the larger event duration, as will be presented in the following paragraph.

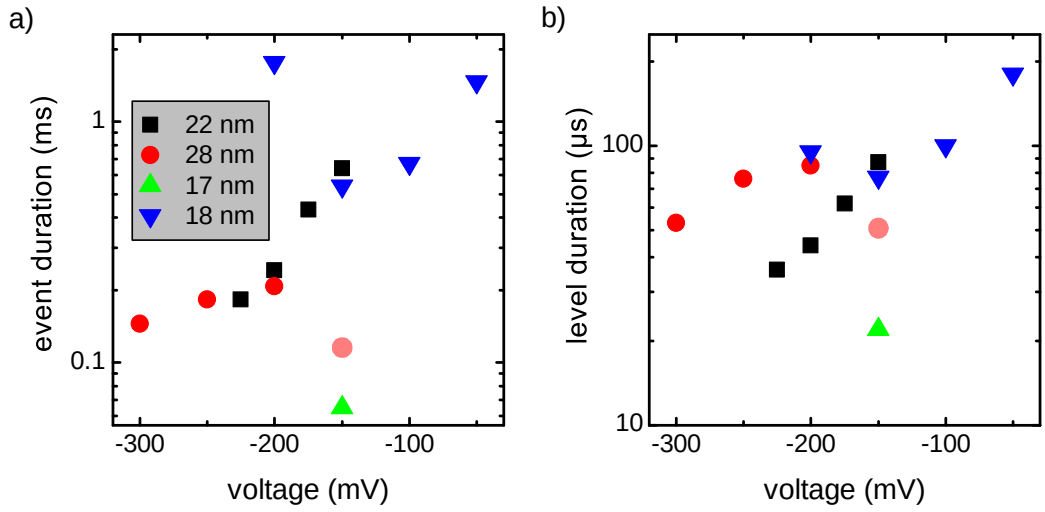

Figure 5.13: a) Event duration for different voltages and pores. Each symbol corresponds to a different pore, as indicated by the inset in the upper left graph. **b)** Level duration, same symbols as on the left.

Table 5.1: Event evaluation of proteasome translocations.

Chip D_p/L_p (nm)	V_{bias} (mV)	# of events / good peaks (%)	$\Delta\bar{I}\cdot/\sigma$ (%)†	$\tau^{\mathrm{fit}}_{\mathrm{event}}\cdot/\sigma$ (µs)	$\tau^{\mathrm{fit}}_{\mathrm{lvl}}\cdot/\sigma$ (µs)
22 / 50	-150	811 / 93	2.0·/1.6	641·/3.5	87·/6.2
	-175	1127 / 91	1.9·/1.6	430·/3.8	62·/6.4
	-200	2437 / 84	1.7·/1.6	242·/4.0	44·/6.2
	-225	1575 / 81	1.6·/1.6	183·/4.0	36·/5.7
	+200	37 / 95	1.2·/1.5	283·/3.5	43·/6.4
28 / 50	-150	275 / 73	1.0±0.7	115·/5.0	51·/5.6
	-200	1800 / 78	1.0±0.7	207·/4.2	85·/6.0
	-250	987 / 77	0.6±0.6	183·/4.3	76·/5.2
	-300	2765 / 74	0.6±0.4	145·/4.5	53·/4.9
17 / 50	-150	637 / 59	2.1·/1.8	65·/2.4	22·/2.6
18 / 40	-50	697 / 73	3.76·/2.4	1460·/3.3	180±10
	-100	903 / 78	4.12·/3.2	670·/3.0	100±10
	-150	1680 / 77	5.00·/3.2	540·/2.6	77±10
	-200	1418 / 74	5.00·/1.6	1760·/3.6	95±10

†: Calculated average values from conductance blockade simulation: 22 nm: 2.8±2.1%, 28 nm: 1.8±1.1%, 18 nm: 5.6±3.7%, 17 nm: 4.3±3.8%. Calculation is based on constant adsorption probability along the pore and adsorption on the edge of the pore was neglected.

Table 5.2: Pore diameter as determined by TEM and pore conductance measurements. The calculated diameter is based on 50 nm pore length.

D_{TEM} (nm)	$R_p\cdot\sigma$ ($\cdot 10^6$ m^{-1})	$D_{\mathrm{Calc.}}$ (nm)
16	115	17.4
16	108	17.8*
21	88	21.8
26	66	27.6

* Calculated for 40 nm pore length.

Explanation for the discrete conductance blockade distribution of the 18 nm chip.

Discrete blockade levels were found for the 18 nm pore, which contradicts the expectation of a random location of proteasome adsorption inside the pore. The most explicit differences to the measurements shown above is the increased number of levels per event and the effect of increasing event duration for increasing applied potential, starting from -200 mV on up to -260 mV. Higher potentials could not be evaluated anymore due the long lasting and very noisy blockade events with a level-rich blockade structure.

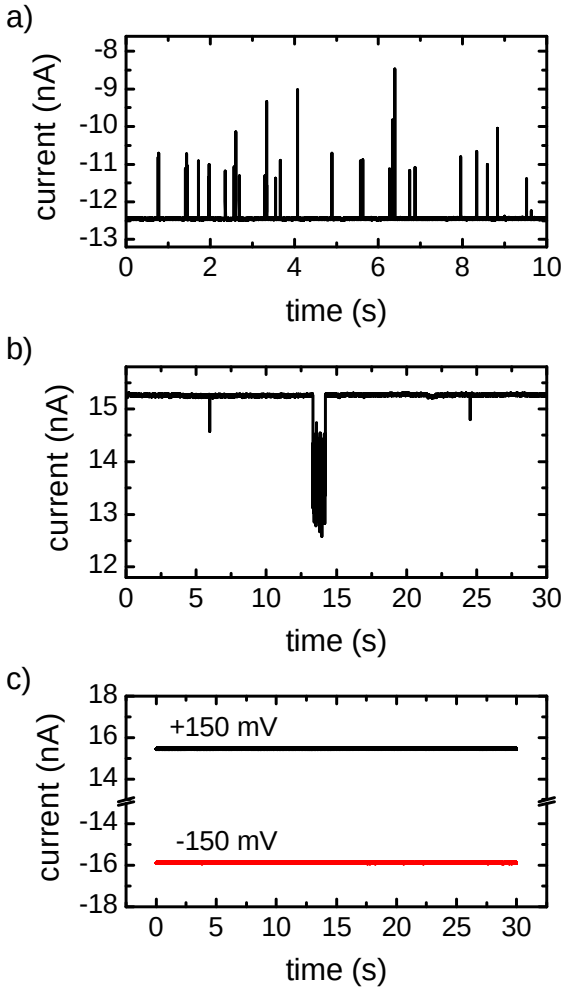

Figure 5.14: a) Current-time trace of 120 nM proteasome translocations at -150 mV, pH 7.3, 1 M KCl. **b)** After reversing the voltage to +150 mV, only few events are observed. **c)** Reference measurement without proteasome at +150 mV (upper curve) and -150 mV (lower curve).

Proteasome molecules where added to a final concentration of 120 nM to the cis-side of the measurement chamber and a voltage of -150 mV was applied to the trans-side. The 1 M KCl solution was adjusted to pH 7.3 by 20 mM Tris-HCl buffer. The initial diameter of the pore was 18 nm, as determined by TEM.

After evaluation of the measurement data, we recognized a small shift in the ionic current baseline upon reversing the applied voltage, which is usually not observed in clean solid-state nanopores of this size. Figure 5.14 a) and b) show current traces for -150 mV and +150 mV applied voltage. For -150 mV, the baseline is decreased by 2.8 nA or 18%. Because the pore showed no rectifying behavior beforehand (Figure 5.14 c)), we attribute this effect to some protein fraction or other contaminant which adsorbed strongly in the vicinity of the pore entrance. Upon application of a negative voltage, the EOF drags the contaminant inside the pore, thereby decreasing the effective diameter permanently. Upon reversing the voltage, it is pushed out of the pore and hence does not influence the pore resistance. Similar effects were also observed in other measurements but usually not evaluated.

Figure 5.15 a) shows a scatter plot of the mean current blockade and event duration at -150 mV. The majority of events blocks an average of 100–200 pA for a duration of 200–1500 µs. The histogram in Fig. 5.15 b) shows a Gaussian distribution with a mean current blockade of

156 ± 98 pA, in contrast to the other measurements, where we observed modified Gaussian distribution of the mean blockade height. The event duration is lognormal distributed and has a median duration of 694 ·/ 2.4 µs. Figure 5.15 d) shows the potential dependent mean current blockade. As expected, the blockade height increases linearly with increasing potential. The same data is shown in Fig. 5.15 e) as relative values. Here, the mean blockade height is around 4.5% for all applied voltages. Figure 5.15 f) shows the median event duration. It decreases non-linear between -20 and -150 mV and increases for -200 mV, which is the unique feature of this chip. For a measurement at pH 8.2, this unexpected behavior is even more pronounced for voltages up to -260 mV. The event data is given in more detail in Tab. 5.1.

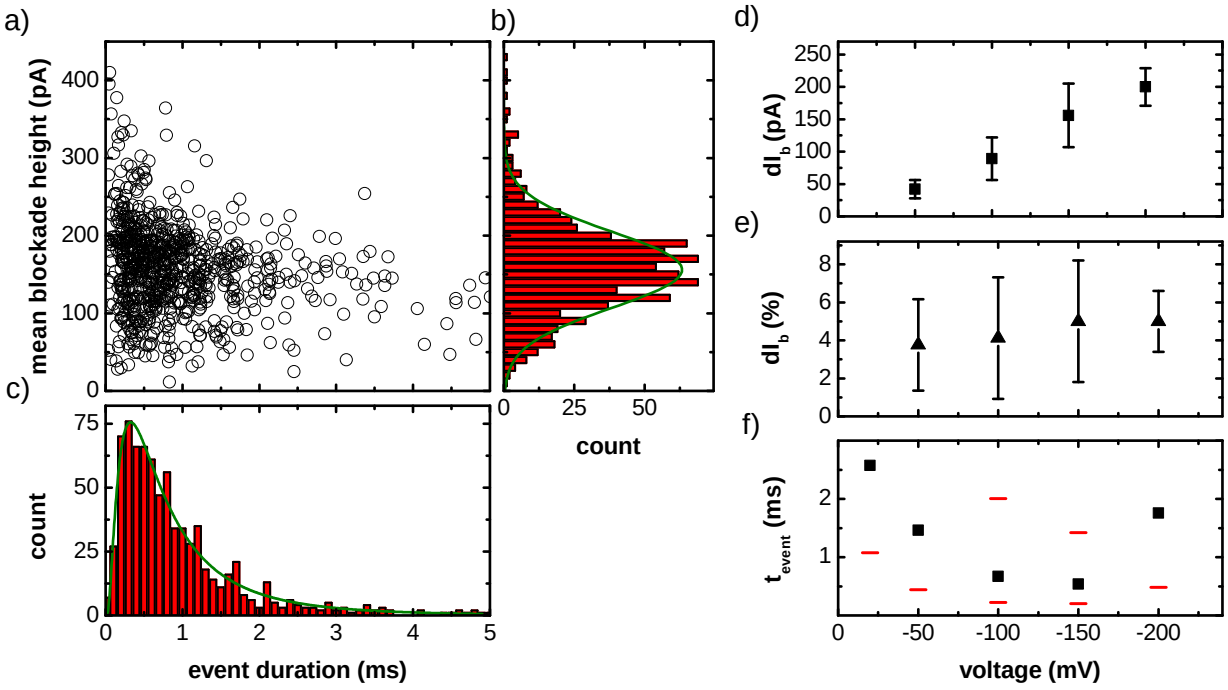

Figure 5.15: a) Scatter plot of proteasome translocations, 18 nm pore, pH 7.3, -150mV. **b)** Histogram of mean current blockade height. Solid line represents a Gaussian fit to the data. **c)** Histogram of event duration. Solid line represents a lognormal distribution fit to the data. **d)** Mean current blockade for different voltages. **e)** Relative mean current blockade. **f)** Median event duration. Red bars depict the standard deviation.

Having a closer look on the current blockades, we can extract only the parts of the current-time trace containing blockade events. This is shown in Fig. 5.16 a) for 810 events of the -150 mV measurement, which are normalized to eliminate the influence of a drifting baseline. Only a small fraction of the original data points is drawn for better visibility. Gaps like the one at 0.7–0.8 s stem from excluded long-lasting events, which would dominate the histogram of the many short events. As can be seen by the black bars in the histogram of Fig. 5.16 b), a broad distribution of current levels exists between 0.5 and 12% current blockade. Besides the two dominating levels at

4.0 and 5.2%, several smaller levels are visible. Similar level spacings are also found for different applied voltages as summarized in Tab. 5.3. All voltages show the same levels at $1.3 \pm 0.1\%$, $2.2 \pm 0.1\%$, $4.0 \pm 0.1\%$, $5.3 \pm 0.04\%$ and $6.4 \pm 0.04\%$. However, the all-points histogram of a current-time trace from a measurement presented in the previous section (the 22 nm diameter pore) also shows some peaks, even though not as pronounced as for the 18 nm chip. This histogram is shown in the inset of Fig. 5.16 b). Because we did not observe noticeable discrete level spacing for this chip, the all-points histogram is obviously not meaningful enough to characterize the translocation behavior. This is because it overestimates the relevance of long lasting levels with respect to the short ones. Only a few levels lasting for several tens of milliseconds will dominate the majority of short levels which last around 100 µs.

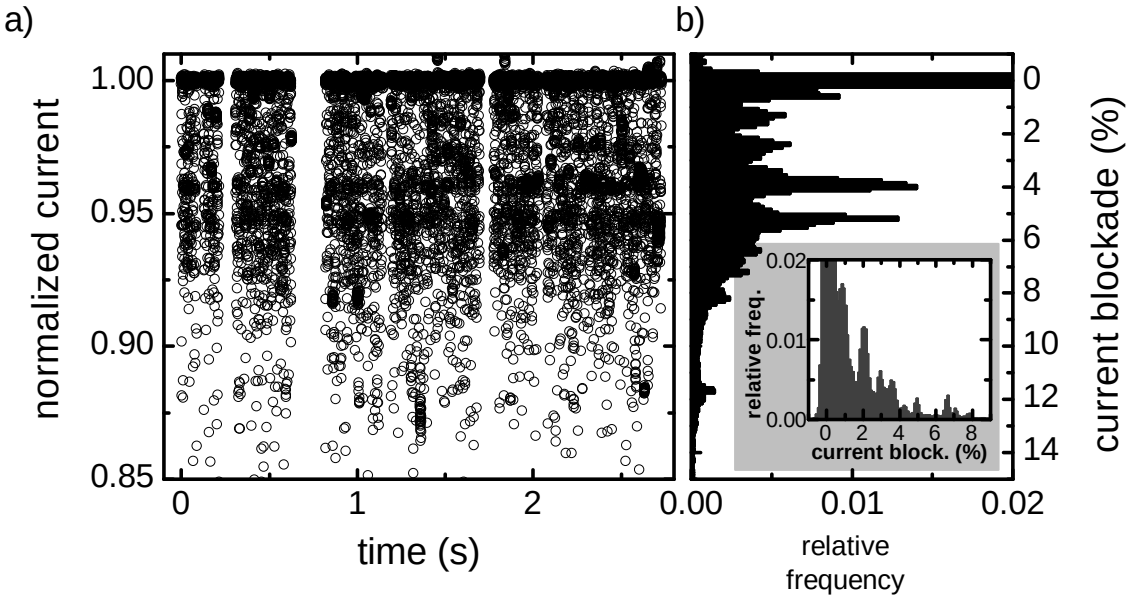

Figure 5.16: a) Normalized current blockades, -150mV, pH7. **b)** All-points histogram of current blockades. Inset: all-points histogram of the 22 nm chip, which showed random blockade heights.

Table 5.3: Evaluation of distinct blockade levels, 18 nm chip.

V_{bias} (mV)	current blockade level ΔI_l (%)										
-50	–	1.1	2.2	–	3.8	–	5.3	6.4	–	–	
-100	0.5	1.4	2.1	–	4.0	5.0	5.4	6.4	–	–	
-150	0.6	1.3	2.4	–	4.0	–	5.2	6.4	7.2	8.2	11.7
-200	–	1.3-1.5	2.2	2.8	4.1	4.8	5.3	6.5	7.0	9.5	11.9

To count each blockade level only once, no matter how long it is, we have to evaluate the level structure and hence create the histogram of the level blockade height, as we did also in the preceding section. This is shown in Fig. 5.17 b), where the red line depicts the scaled all-points histogram and the black bars the result of the automated evaluation of the level heights. Here, we also notice the difference in histograms at small blockade values between this and all other chips (Fig. 5.12). Whereas for the other chips we observe the highest rates at the smallest blockade value, we now observe a decreased rate for small values and a maximum at around 5%.

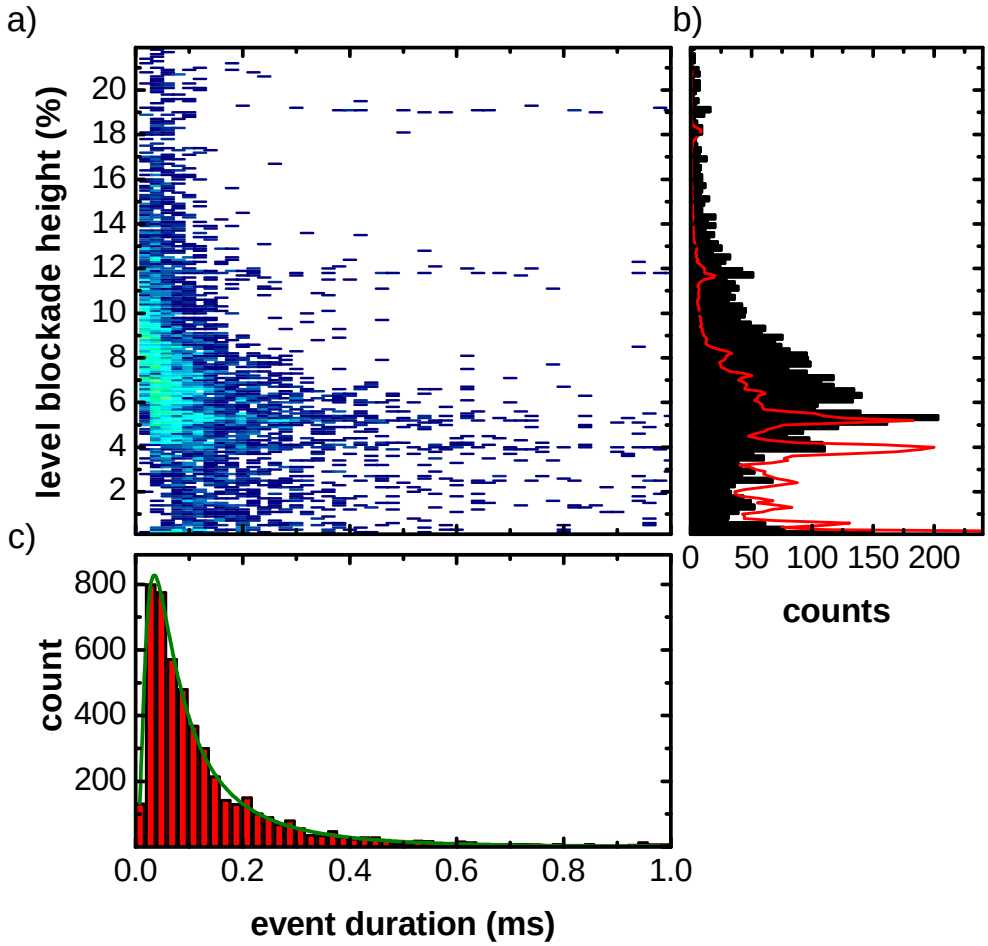

Figure 5.17: a) Color plot of blockade levels at -150mV. **b)** Black bars: Histogram of level blockades. Red line: All-points histogram of current-time trace. **c)** Histogram of level duration. Green line: lognormal distribution fit to the data.

In contrast to the discrete level spacing, the duration of the blockade levels is uniformly distributed, Figure 5.17 c) and 5.18. For -150 and -200 mV, the level duration can be described with a single lognormal distribution. For -50 and -100 mV, the single distribution describes the data

only up to ∼250 µs. However, fitting the data with two lognormal distributions is difficult, as the dependencies between the parameters are very high (> 0.99). This means different values of the parameter give the same or similar results, which precludes a meaningful interpretation. Due to the problems with fitting, we derive the median blockade duration from a graphical representation of the cumulative histograms. The inset of Fig. 5.18 shows the distributions for different voltages. The median level durations extracted from this graph are given in Tab. 5.1 and shown graphically in Figure 5.19 in dependence of the applied voltage. The level duration gets shorter for increasing voltage up to -150 mV, as expected. For -200 mV, the level duration increases, which can not be explained coherently.

As mentioned at the beginning, we attribute this effect to some unidentified protein contaminant, which adsorbed in the vicinity of the pore entrance. The gap in the blockade histogram between 1 and 5% could thus be explained by a contaminant at the pore opening which prevents the proteasome from adsorption in this area. The long-lasting events in this range might be caused by interactions with proteasome subunits, i.e. lysine residues at the protein surface. A correlation of the conductance blockade values with the proteasome position inside the pore gives approximate distances of the adsorption sites of 4, 7, 3 and 2 nm for the blockade levels at 1.2, 2.2, 4.0, 5.3 and 6.4%. However, these values might be misleading, as we did not consider any adsorbed particle in the simulation of conductance blockade. We therefore would like to conclude that care must be taken to ensure a clean pore for protein translocation experiments. As this example shows, the experimental observations might otherwise lead to conclusions which are only valid in this special case.

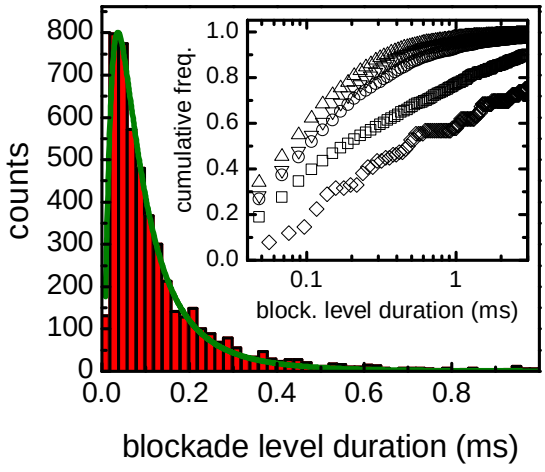

Figure 5.18: Distribution of blockade level duration. Inset: Cumulative distribution for -20 mV (◇), -50 mV (□), -100 mV (○), -150 mV (△), -200 mV (▽).

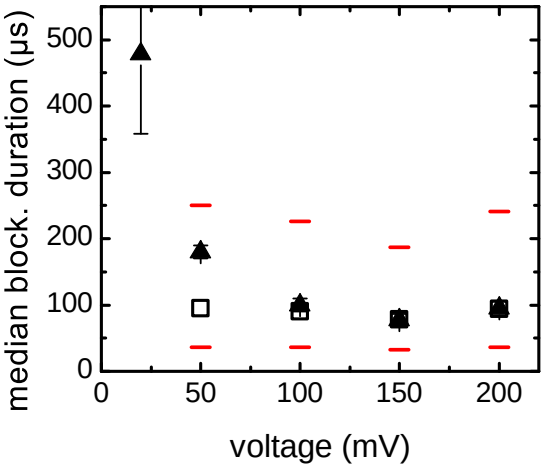

Figure 5.19: Voltage dependent level blockade duration, median values derived from lognormal fit (□) and from the inset in figure 5.18 (▲). Red bars depict the 2σ range of the lognormal distribution.

5.2.2. Discussion

The most interesting feature of the proteasome translocation experiments is the blockade level structure appearing in most of the events. This contradicts the expectation of a current blockade for a freely translocating, barrel shaped particle like the proteasome. The constant current of each level implies a stopped motion of the particle at different positions in the conical nanopore under the assumption of a folded protein. This assumption is supported by a simulation of the expected, position dependent current blockade caused by a cylindrical particle, which is in good agreement with the experimentally observed current blockades. We therefore suggest transient adsorption of the proteasome on the pore wall. This effect is also discussed by Sexton et al. for long polymer pores. They don't observe single current levels, but an apparently linear decrease in current as the molecule translocates the pore. However, the opening angle of polymeric pores is much smaller (1.2°[100]) and the length of the active region much larger (∼1 µm) as in Si_3N_4 pores. Thus, the difference between the subsequent blockade levels is smaller than the signal to noise ratio, which gives the impression of a linear decrease. In our case, the short pore length (40–50 nm) together with the large opening angle (17–19°) leads to detectable changes in current for small changes in the position of the molecule inside the pore. The decreasing frequency of adsorption for increasing blockade height resembles the probability of hitting the surface. The increased blockade rate between 0.3 and 0.8% in Fig. 5.12 for all pores corresponds to the point of first adsorption. This is equivalently shown in Fig. 5.10 for the 22 nm pore, where the most probable adsorption point is at 0 ± 8 nm, according to the maximum at $0.7 \pm 0.3\%$ for the first level and the simulated curve in Fig. 5.12. Here, a negative position means that the molecules hit the edge of the pore entrance or the membrane surface in striking distance to the pore, thereby affecting the access resistance. We have to point out that these events are no bumping events! As shown in Fig. 5.10 and explained in the text, several larger blockade levels follow this first adsorption point, indicating translocation of the protein. We conclude that most of the molecules first adsorb in the vicinity of the pore entrance before being pulled further through the pore, where additional adsorption events may occur.

The expected translocation time is another indication for protein adsorption. As shown in the theory section, the expected velocity for free translocation of a particle can be estimated as $v_{free} = \frac{\epsilon_0 \epsilon_r}{\eta} \cdot E \cdot (\zeta_{prot} - \zeta_{pore})$. We therefore would have to measure the zeta potential of proteasome to give a precise estimation of the resulting velocity of free translocation. However, approximately 1 mg of protein is needed for a single zeta potential measurement, which was not available for this purpose. We can though give an upper value of the zeta potential, because we know its sign[27,136] and we know that it translocates in direction of the electroosmotic flow. If EO flow dominates protein transport and both potentials have equal sign, ζ_{prot} has to be smaller than ζ_{pore}, i.e. $\zeta_{\mathrm{prot}} <$ -20 mV because we know the pore zeta potential from measurements[30]. We can therefore conclude that the free translocation time of the proteasome has to be in between the extremes of zero zeta potential ($\tau = \mathrm{l_p}/\mathrm{v_{EO}} \approx 1.2$ µs) and diffusion ($\zeta_{\mathrm{prot}} = \zeta_{\mathrm{pore}},\ \tau = \mathrm{t_{diff}} = \mathrm{l_p^2}/2\mathrm{D} \approx 100$ µs). The last point can be excluded, because we observe proteasome translocations only for one polarity and not for both polarities, as for avidin at pH 4. Even a small difference in zeta potential of only 5 mV would result in a translocation time of 4 µs. This is much smaller than what we observe in our experiments, where $\tau =$ 100–2000 µs.

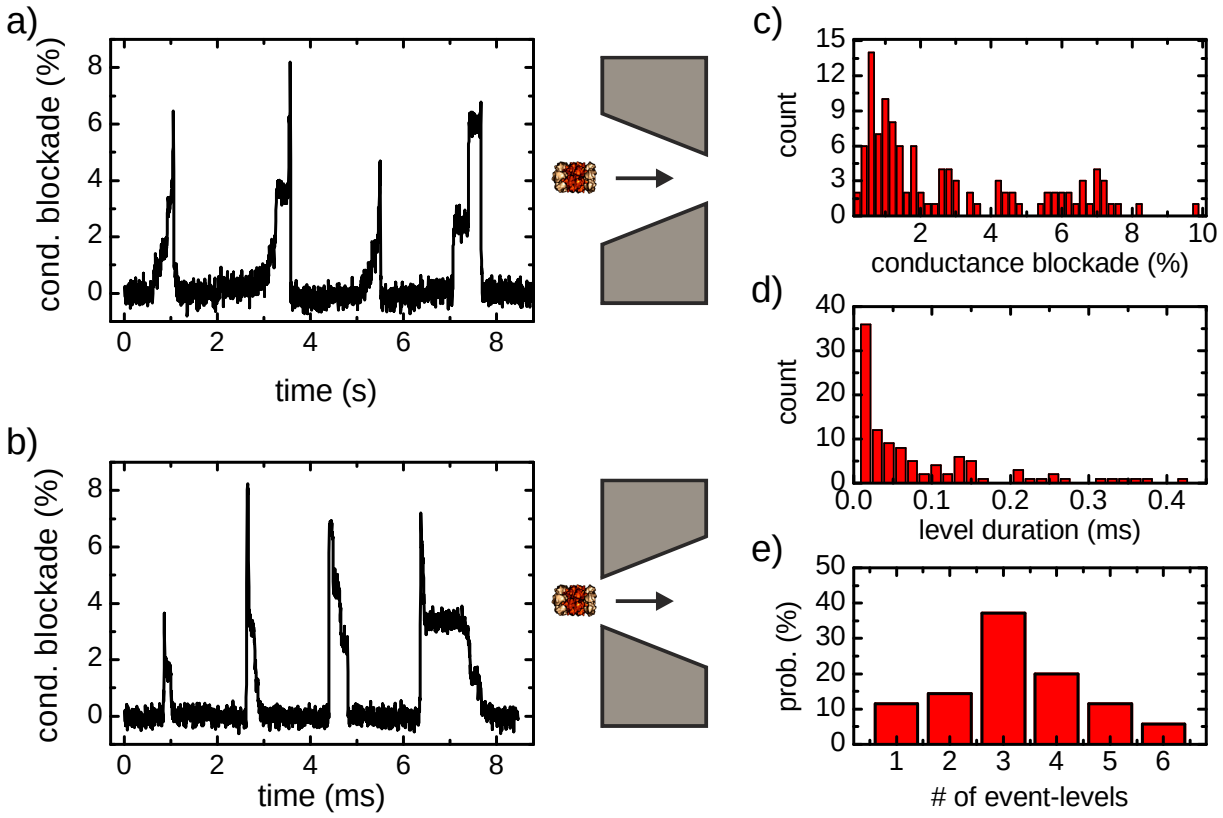

Figure 5.20: a) Selected blockade events at -200 mV. Proteasome translocates the pore from the large to the small opening. **b)** Selected blockade events at +200 mV. Proteasome translocates the pore from the small to the large opening. **c)** Conductance blockade histogram at +200 mV. **d)** Level duration histogram at +200 mV. **e)** Level probability at +200 mV.

Evidence that the observed level structure is caused by the conical pore shape and not by partly unfolded proteasome is shown in Fig. 5.20. Here, we reversed the voltage from -200 mV to +200 mV after 30 minutes of translocating molecules. In contrast to the reference measurement shown in Fig. 5.5 b), we now observe blockade events at positive voltage. Reversing the voltage has the effect that formerly translocated molecules enter the pore at the small opening. Having a closer look on the event structure, we observe primarily events with a large conductance blockade at the beginning and decreasing blockades in subsequent levels. We evaluated the fraction of events which show only increasing blockades and the fraction of events which has the largest blockade in the first or second level. It turns out that for -200 mV, 78% of the observed events show exclusively increasing blockades and 19% have their maximum in the first or second level. For +200 mV, 71% have their maximum in the first or second level and only 25% show increasing level blockades. The range of the observed conductance blockades as evaluated in the histogram in Fig. 5.20 c) is similar to the range obtained at -200 mV, and the same is observed for the level duration. Only the number-of-levels probability is decreased for one- and two-level events. We

attribute this effect to an increased probability for hitting the pore rim if the translocation is directed from the small to the large pore opening and to a decreasing pulling force if the molecule traverses towards the large exit of the pore, thus favoring multiple adsorption.
Besides the transient adsorption of the protein, we also suggest that the drag on the adsorbed molecule increases from the large pore entrance to the small end of the conical pore. This could be caused by retardation or electroviscous effects or an increase in flow velocity by a decreasing channel diameter and a simultaneously increasing electric field. The electroosmotic force on the particle might thus increase stronger than the electrophoretic force, leading to a reduced adsorption probability near the tip region. Even if these effects are difficult to evaluate in detail, due to the complicated geometrical and chemical structure of the molecule and the pore, this assumption is supported by the experimentally observed decrease of the level blockade rate at the end of the pore upon increasing the applied potential, as shown in Fig. 5.8 d). The average level duration depending on the conductance blockade, shown in Fig. 5.8 a) also shows that the large level blockades, which are associated with an adsorption position at the small end of the pore, correspond to very short levels.

5.2.3. Conclusion

We showed that proteasome molecules translocate Si_3N_4 nanopores in direction of the electroosmotic flow at pH 7–9. Translocation events show a detailed blockade level structure, indicating multiple (1–6) adsorption events during translocation. The observed blockade heights correspond to the position inside the pore, where the protein adsorbs transiently between 30 and 80 µs, depending on the applied voltage and pore geometry. A larger pore diameter increases the adsorption time which can be explained by a decreasing pulling force on the molecule due to the decrease in electric field and electroosmotic flow. At the same time, the larger pore diameter leads to a smaller number of adsorption processes, owing to the interplay between the fast ($\sim$µs) electroosmotic transport parallel to and the slow diffusion towards the pore wall.

5.3. Proteasome trapping in small nanopores

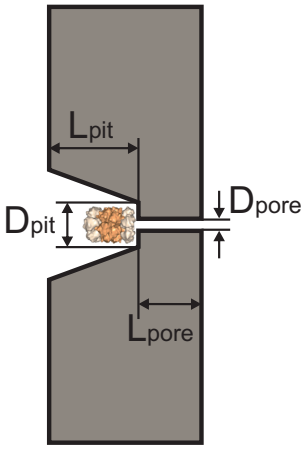

Figure 5.21: The pit-pore device.

Trapping of single proteasome molecules in a nanopore is a challenging task. In contrast to membrane proteins, which incorporate themselves in lipid bilayers and build a perfect seal against ionic leakage currents, we have to tailor the solid-state pore in a way that it not only traps the molecule, but also minimizes leakage currents. The initial idea of trapping the molecule was to use the His-tags at the side of the molecule. One could make a self-assembled monolayer with Tris-NTA headgroups, which would grab the molecule, once it passes through the pore. The difficulty in this approach lies in the necessity of very high accuracy concerning the pore diameter. Furthermore, if the pore would be cylindrical, it is very unlikely that the proteasome enters a pore which has almost the same diameter than the molecule itself. If it would be conical, as are the e-beam lithographically fabricated pores, it could enter the pore at the large opening, but bind to the sidewall somewhere near the orifice, thus not sealing the pore properly. Because of these concerns, we invented the spot-drilled pit pore drawn schematically in Fig. 5.21 and described in the fabrication section in detail. Here, the proteasome can enter the conical part of the pore, and might adsorb transiently on the Si_3N_4 sidewall, as shown in the section before. It can, however, move down to the bottom of the spot-drilled pit and is thus trapped. A frequent and expected problem in this device is the signal-to-noise ratio. Thermal fluctuations of the proteasome inside the pore increase electrical noise considerably. However, the timescale of peptide residence in the central proteasome chamber (substrate processing) is usually much larger than the observed thermal current fluctuations, which permits to use a small electronic filter frequency or to smooth the signal for evaluation.

5.3.1. Reversible trapping of single proteasome molecules

The first experiment shows reversible trapping of proteasome molecules. The molecule is dragged towards and inside the pore by the EOF and can be released by reversing the applied potential. Proteasome was added to a final concentration of 0.5 nM in 600 mM KCl and 30 mM Tris-HCl at pH 9.3. Upon application of -200 mV at the trans-side, a permanent decrease of the open pore current from -12.8 nA to -10.5 $\pm$ 1 nA is observed. Reversing the potential leads to an immediate conductance increase to the open pore level of +13.8 nA (Fig. 5.22, left side). The open pore current is 7% smaller at negative voltages due to a slightly rectifying behavior of the pore. This is shown by a current–voltage measurement presented in Fig. 5.23. Similar rectification is also observed for other pit-pore chips and attributed to the small diameter in combination with the conical pore shape[5,101]. The normalized histogram on the right side of Fig. 5.22 compares the ionic current at positive and negative voltage. The black line shows the conductance blockade at positive voltage (+200 mV), i.e. after releasing a trapped proteasome.

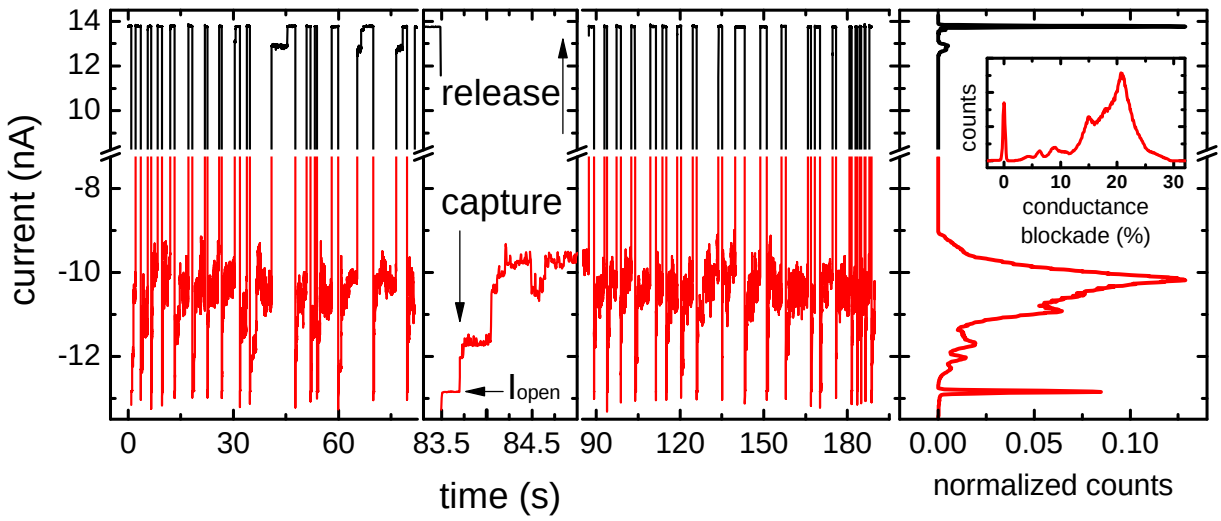

Figure 5.22: Left: Reversible proteasome trapping. The applied potential is switched between +200 mV (black) and -200 mV (red) during continuous current recording. The middle part shows a single capture event with the characteristic steps due to adsorption. Data is down-sampled to 250 Hz for better visibility. Right: Normalized histograms of the reversible trapping events on the left, split in positive (black) and negative (red) currents. The inset shows the same histogram at negative potential in units of relative conductance blockade.

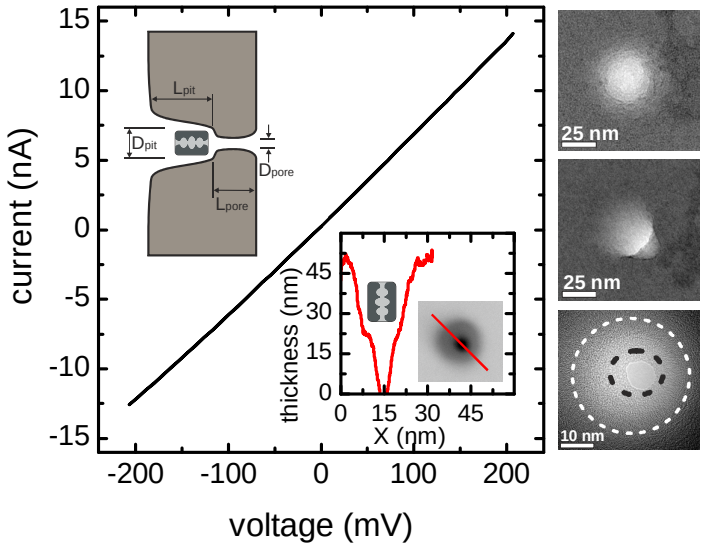

Figure 5.23: Current-voltage characteristics of a pit-pore device, drawn schematically in the upper left corner. Inset: Thickness profile of the pit-pore and corresponding TEM image, acquired in HAADF mode. Right, top down: TEM image of the pit before TEM drilling of the small pore. The same image tilted by 30°. TEM image after TEM drilling. The pit can be slightly seen as a brighter circle around the pore.

Besides the open pore current at 13.8 nA (0% conductance blockade) only a small fraction at 12.5–13 nA (6–8%) is visible, which can be attributed to few long-lasting adsorption events. The histogram for the negative voltage (-200 mV), depicted by the red line, shows a peak at -10 nA (21%) and a broad distribution between -9 and -12 nA (15–25%), which can be explained by adsorption of the proteasome inside the pit and random motion, leading to an increased noise level. The inset shows the same histogram of the current-time trace with a relative conductance blockade scale. Similar behavior is found for other voltages: Figure 5.24 shows all-point histograms from reversible proteasome trapping events at -100 mV (black curve), -200 mV (red curve) and -300 mV (green curve). For -100 mV, the maximum conductance blockade is at 7% and also blockades up to 20% are observed. At -300 mV, a broad distribution between 11 and 27% indicates an increased tendency of sealing leakage currents around the proteasome molecule.

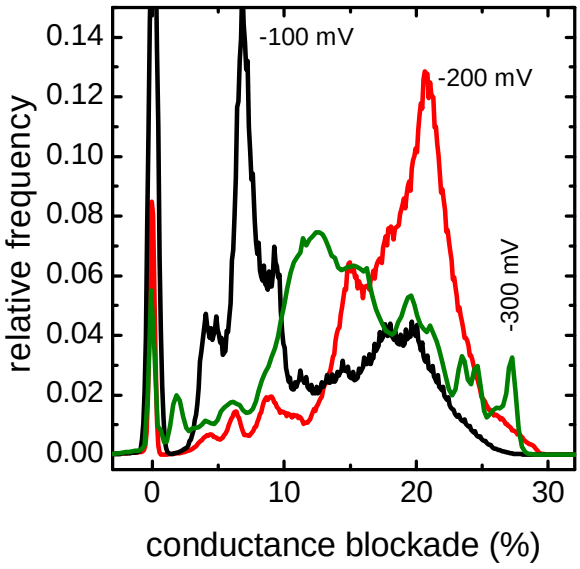

Figure 5.24: Conductance blockade histograms (all-point histograms) of reversible proteasome trapping at different negative potentials: -100 mV (black), -200 mV (red), -300 mV (green).

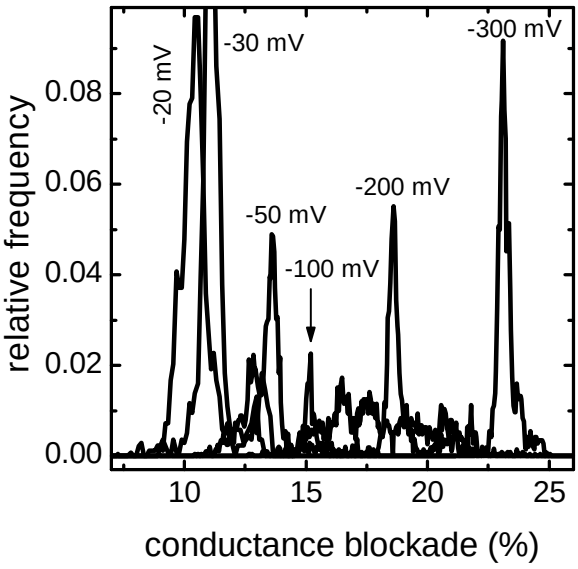

Figure 5.25: Conductance blockade histograms of a single proteasome trapping event for increasing trapping potential.

Figure 5.25 illustrates the pore conductance at different trapping voltages of the same proteasome molecule. Starting with an empty pore at +200 mV (no histogram shown), the potential was set to -20 mV and the pore got blocked by a proteasome molecule. The conductance blockade histogram of this state is shown as the leftmost peak, labelled '-20 mV' in Fig. 5.25. With the same molecule still present in the pit-pore, we increased the potential stepwise up to -300 mV (steps: -30, -50, -100, -200 mV) and measured the pore conductance at each voltage. The conductance blockade histograms summarized in Fig 5.25 show apparent shifts towards increasing conductance blockades with increasing potential from 10% (-20 mV) to 24% (-300 mV), which

is well comparable to the reversible trapping histograms shown in Fig. 5.24. We attribute the decreasing conductance with increasing applied potential to an increasing electroosmotic force, pushing the proteasome towards the bottom of the conical pit, thereby reducing leakage current around the molecule.

Estimation of conductance blockades

At a first glance, the small conductance blockades of only 20–30% might seem too small for full blockage of the pore by a proteasome molecule. We therefore simulated the pit pore device according to the drawing in Fig. 5.21. We call the conical part of the pore "pit" with small diameter at the bottom $\mathrm{D_{pit}}$, length $\mathrm{L_{pit}}$ and resistance $\mathrm{R_{pit}}$. The narrow constriction of the pore is assumed to be cylindrical with diameter $\mathrm{D_{pore}}$, length $\mathrm{L_{pore}} = 50\ \mathrm{nm} - \mathrm{L_{pit}}$ and resistance $\mathrm{R_{pore}}$. We also included the access resistance as described in chapter 3.5 and the proteasome dimensions are increased by 0.5 nm to account for the hydration shell. The channel of the proteasome itself is modelled as a simple cylindrical pore with diameter $\mathrm{d_{prot}}$, length $\mathrm{L_{prot}}$ and resistance $\mathrm{R_{prot}}$.

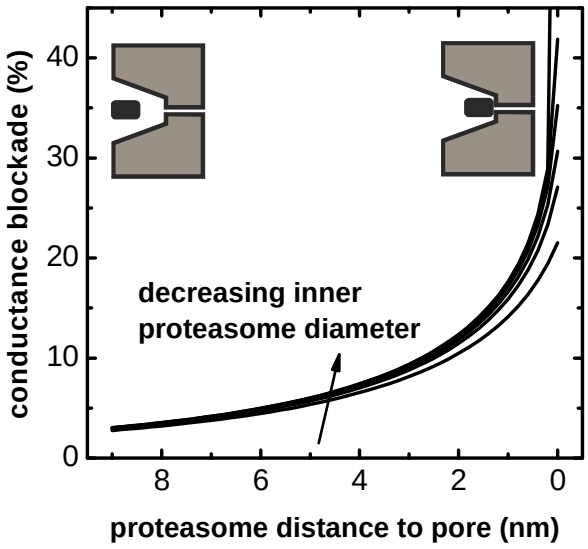

Figure 5.26: Simulation of conductance blockade in a pit-pore. The schematic drawings depict the proteasome position at 0 and 9 nm. Proteasome channel diameter: 3.0, 2.0, 1.5, 1.0, 0.5, 0.0 nm.

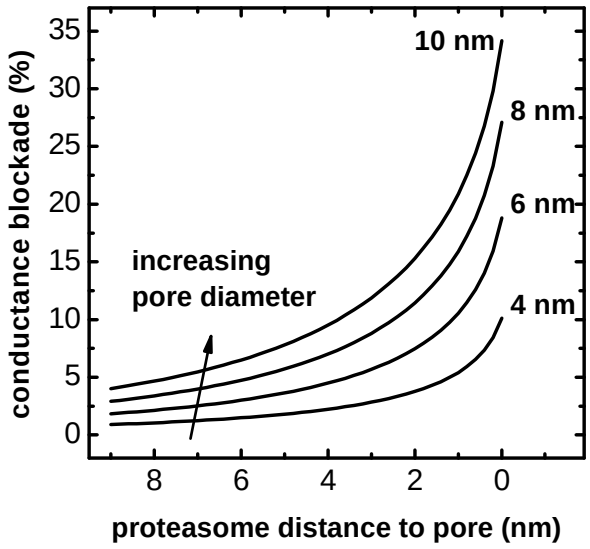

Figure 5.27: Position dependent conductance blockade for different diameters of the small Si_3N_4 pore (4–10 nm).

Figure 5.26 shows the expected conductance blockade in dependence of the proteasome position inside the nanopore with $\mathrm{L_{pit}} = 25$ nm, $\mathrm{D_{pit}} = 12$ nm and $\mathrm{D_{pore}} = 8$ nm. The position scale shows the distance between proteasome and bottom of the conical pit in nm. The different curves correspond to different diameters of the proteasome channel, namely 0, 0.5, 1.0, 1.5, 2.0 and 3.0 nm. As expected, if the proteasome wouldn't contain any channel, the conductance blockade

rises up to 100% at 0 nm proteasome to pore distance (upper curve), which is not visible in the figure. For reasonable effective proteasome channel diameters between 0.5 and 2 nm, the conductance blockade shows noteworthy deviations only for a protein to pore distance smaller than 1 nm.
Changing the diameter of the small Si_3N_4 pore shows a much larger effect on the conductance blockade (Fig. 5.27). Here, the proteasome channel diameter is fixed at 2 nm and the pit length at 25 nm. By increasing $\mathrm{D_{pore}}$ from 4 to 10 nm, the conductance blockade increases by 20% at a distance of 1 nm from the bottom. This behavior is easily understood if we consider the pit-pore as a system of two individual resistors in series. The overall resistance is dominated by the largest resistance. If the cylindrical pore is very small and thus its resistance very high, changes in the small pit resistance due to a proteasome molecule do not alter the total resistance much and vice versa. It is therefore preferable to fabricate pores just small enough to hinder proteasome translocation, but not smaller, in order to increase the proteasome signal.

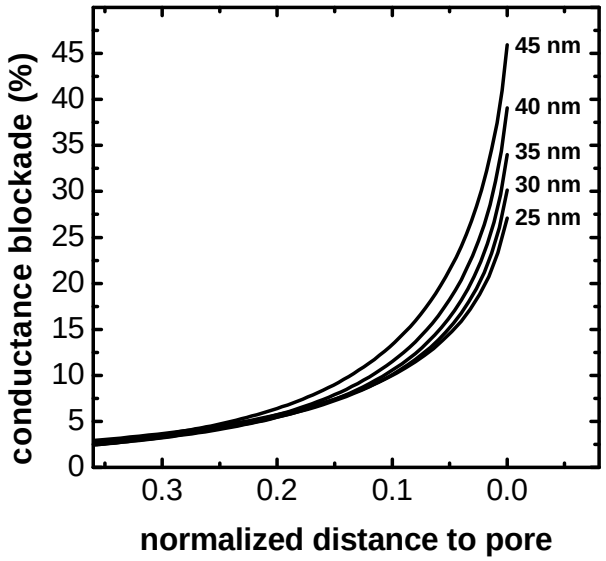

Figure 5.28: Position dependent conductance blockade for different pit lengths, as indicated. The total thickness of the pit-pore device is always 50 nm. The normalized distance to pore $\overline{D}_{p-p}$ is defined by the distance between proteasome and pore D_{p-p} and the pit length L_{pit} as follows: $\overline{D}_{p-p} = \frac{D_{p-p}}{L_{pit}}$.

The length of the pit may also vary, and this is simulated in Fig. 5.28. Here the distance to the pore is normalized to the pit length. Like before, at position 0 the proteasome is situated at the bottom of the pit for all $\mathrm{L_{pit}}$. The pit length is given at the right side in Figure 5.28. For proteasome to pore distances larger than $\sim 0.3 L_{pit}$, the conductance blockade is almost independent of the pit length. For example, if a proteasome molecule is 13.5 nm in front of the pore in a 45 nm long pit, it gives almost the same small conductance blockade as if the molecule would be 7.5 nm in front of the pore in a 25 nm long pit. This is the result of a decreasing influence of $\mathrm{R_{pore}}$ if the pit length is increasing. Furthermore, with increasing pit length the resistance at the pit entrance decreases, as the diameter gets wider. Thus, the conductance blockade rises only slowly with the

position of the proteasome inside the pit. Only several nanometers before the pore, the change in $\mathrm{R_{pit}}$ influences the overall resistance and thus the conductance blockade considerably. Here, the conductance blockade increases with increasing pit length due to the increasing influence of $\mathrm{R_{pit}}$. Assuming a position of the proteasome near the pit bottom, it is thus preferable to fabricate long pits and short pores. Then the pit resistance gains influence on the overall pit–pore resistance, thus increasing the proteasome blockade signal.

In the last three paragraphs it was shown that the expected conductance blockade for a trapped proteasome is between 25 and 35% for a pit length of 25–35 nm, a pit diameter of 12 nm, a small pore diameter of 6–10 nm and a proteasome channel diameter of 2 nm, which is in very good agreement with the measured data. Here, the dimensions of the pit-pore geometry are chosen in a range as determined by our fabricated pit-pore devices. We therefore assume that the proteasome enters the pit and is situated at a close distance to the bottom, if the applied potential is high enough.

5.3.2. Proteasomal peptide breakdown

The universal aim of this work is to watch a single proteasome during its natural function, the degradation of polypeptides to short peptide molecules. A widely used substrate to determine proteasome activity is Suc-LLVY-AMC, a short peptide (Suc - Leu - Leu - Val - Tyr) bound to the dye 7-amino-4-methylcoumarin (AMC). The dye absorbs light at 353 nm and emits at 442 nm. If it is bound to the peptide, the emitted energy is quenched. Upon degradation by the proteasome, the dye is released and emission can be detected by a spectrometer. The speed of degradation follows the Michaelis-Menten kinetic and the time needed to degrade one peptide is given by the catalytic constant k_{cat}. The proteasomal breakdown is determined by the concentration of proteasome (enzyme, E), peptide (substrate, S) and the enzyme-substrate complex (ES) which finally reacts to free enzyme and the product (P). The reaction can be described by

$$\mathrm{E} + \mathrm{S} \underset{\mathrm{k_{-1}}}{\overset{\mathrm{k_1}}{\rightleftharpoons}} \mathrm{ES} \xrightarrow{\mathrm{k_2}} \mathrm{E} + \mathrm{P}$$

From this reaction scheme, the Michaelis-Menten equation can be derived as:

$$V_0 = \frac{V_{max}[\mathrm{S}]}{K_m + [\mathrm{S}]} \tag{5.2}$$

Here, $V_0([\mathrm{S}])$ is the initial rate, V_{max} the maximum rate and K_m the Michaelis constant defined as $K_m = (k_2 + k_{-1})/k_1$. If substrate is present in excess, the rate limiting step of substrate degradation is determined by k_2, which then equals the catalytic constant, $k_2 \equiv k_{cat}$. In this case, the Michaelis constant K_m equals the dissociation constant of the ES complex.
Several publications report on degradation of Suc-LLVY-AMC or similar substrates, but the reported enzymatic activity varies strongly within these publications[3,23,29,97,113,137]. As can be seen in Tab. 5.4, the first two publications used natural proteasome from *Thermoplasma acidophilum*. They differ by a factor of 3 in V_{max} (the value given by Seemueller has to be multiplied by 14 because it is given for a single active site[97]), which can not be explained by the temperature difference of 5 °C. In the other four publications, recombinant protein from *E-coli* (Akopian, Thess, Felderer) and *Methanosarcina thermophila* (Zwickl) is used. Here the reported values vary by a factor of 12. The most detailed work is the publication of Akopian and the dissertation of Felderer, which also come up with quite similar results (but at a 5 °C difference in temperature).
To estimate the time a single proteasome needs to degrade one peptide, we therefore use a value of $k_{cat} \approx 0.3$ 1/s, which corresponds to a time of roughly 3 seconds for degradation at 55–60 °C. At lower temperatures, the speed of degradation drops rapidly. From the graph published by Dahlmann et al., we can extract an enzymatic activity of 2.88 µmol/h/mg at 47 °C and 0.42 µmol/h/mg at 24 °C. Compared to the value of 6.12 µmol/h/mg at 55 °C, this is 2 and 15 times slower, respectively. At room temperature, we would thus expect a degradation time of at least 45 seconds or longer.

As will be shown in the next section, a trapped proteasome molecule generates abrupt conductance changes on a timescale of minutes, which we attribute to changes in position inside the pit. It would therefore be favorable to examine proteasome molecules at temperatures of 50–60°C, where the peptide degradation time is much smaller than the timescale of the spontaneous conductance changes.

Table 5.4: Enzymatic activities of proteasome reported in literature.

Publication	Buffer	T (°C)	K_m (µM)	k_{cat} (1/s)	V_{max} $\left(\frac{\mu mol}{h \cdot mg}\right)$
Dahlmann1992 (nat.)	20 mM Tris 1 mM NaN3 pH8.0	55	–	–	6.12
Seemueller1995 (nat.)	20 mM Tris 1 mM NaN3 1 mM EDTA pH7.5	60	85±14	0.03*	0.15*
Akopian1997 (rec.)	50 mM Tris pH7.5	55	39	0.3	1.68
Zwickl1999 (rec.)	50 mM Tris 10 mM MgCl 1 mM DTT 1 mM ATP pH7.5	60	–	0.15	0.77
Thess2002 (rec.)	50 mM Tris 1.25% DMSO pH7.5	60	–	1.8	9.5
Felderer2006 (rec.)	20 mM HEPES 150 mM NaCl DMSO pH7.5	60	32	0.32	1.64

* Value for a single active site.

Peptide breakdown at 25°C

Peptide breakdown at room temperature is expected to be extremely slow, on a timescale of tens of seconds to minutes, due to the thermophilic nature of the proteasome host. However, we observed an effect on the conductance after trapping a proteasome and adding peptide substrate. During the reversible trapping experiments shown in Fig. 5.22, we also added Suc-LLVY-AMC. As shown in Fig. 5.29 a), after addition of 10 nM peptide, conductance blockades up to 30% can be observed in a third peak (red line), where previously without the substrate only 20% and two peaks were observed (black line). Also the peaks at 15 and 20% are shifted to the right by approximately 3%. A further increase of peptide concentration to 1000 nM did not result in a further increase of the conductance blockade, Fig. 5.29 b), which indicates that the observed conductance change is not caused by diluting the ionic concentration. The third peak, which appeared after addition of the substrate molecules could be explained by a reorientation of the proteasome inside the pit. The shift of 3% to the right would then be caused by substrate molecules, blocking part of the proteasome channel.

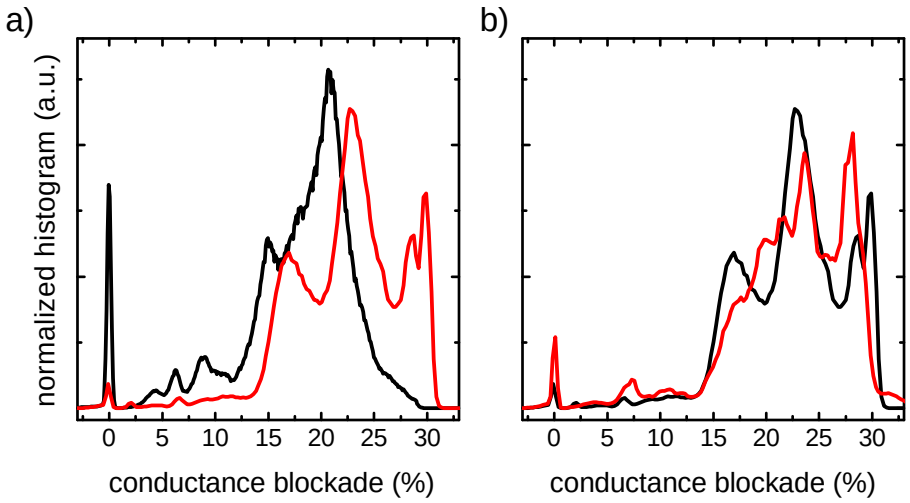

Figure 5.29: a) Reversible proteasome trapping at -200 mV (black) and after addition of 10 nM Suc-LLVY-AMC (red). **b)** Reversible proteasome trapping at -200 mV in the presence of 10 nM Suc-LLVY-AMC (black) and after addition of 1000 nM Suc-LLVY-AMC (red).

Another hint that the observed conductance changes are not due to changes in electrolyte conductance or clogging can be seen in Fig. 5.30, which was recorded with a different pit-pore and in continuous current recording. Part a) shows the current-time trace of the trapped proteasome at -250 mV. In part b), 50 pM peptide is added to the chamber, and after one minute a spontaneous conductance decrease is observed. Further increasing the peptide concentration to 1 nM and 100 nM did not change the current level significantly over minutes.

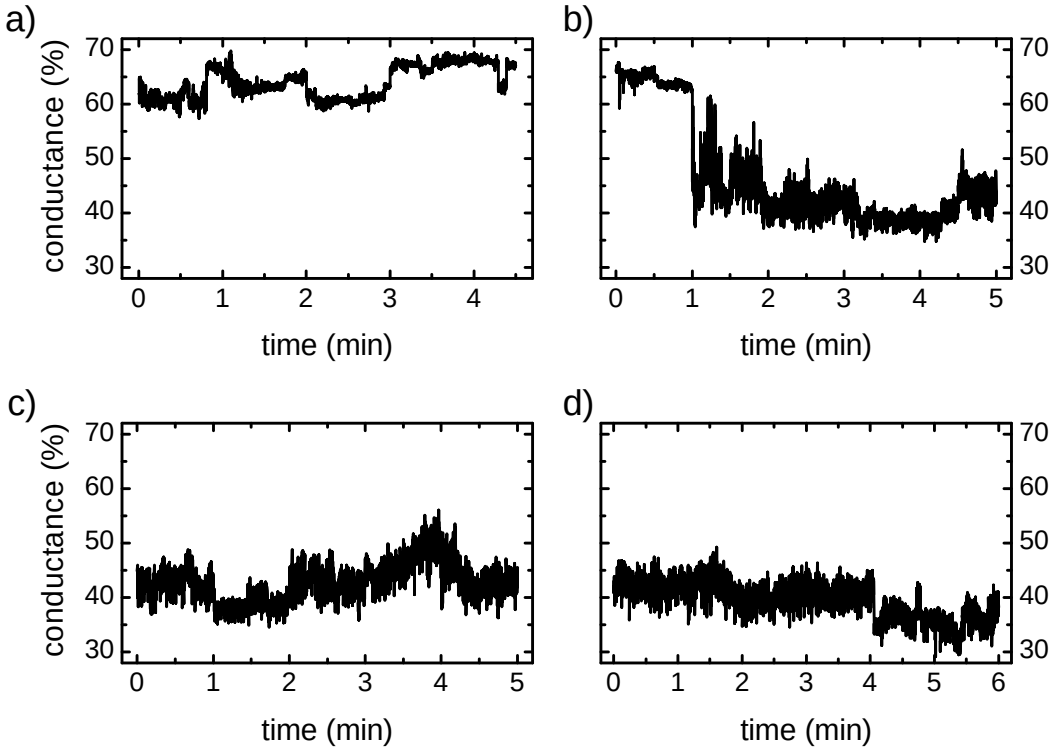

Figure 5.30: a) Proteasome trapping at -250 mV decreases the conductance to ∼65% of the initial conductance value. **b)** After adding 50 pM Suc-LLVY-AMC, the conductance decreases to 40%. **c)** 1 nM Suc-LLVY-AMC, no further conductance decrease. **d)** After adding 100 nM Suc-LLVY-AMC, no further conductance decrease.

Several other measurements in continuous current recording show similar behavior upon addition of Suc-LLVY-AMC. In part a) of Fig. 5.31, which was obtained with a different pit-pore, the conductance blockade after addition of proteasome is shown. Similar to the results in the previous section, the conductance decreases to 60–65% of the open pit-pore conductance. In part b), the addition of 100 nM Suc-LLVY-AMC is followed by a decrease in conductance to 52–57%. In a second experiment with the same chip, Fig. 5.31 part c) and d), we get the same conductance blockade due to proteasome trapping, and also a slight conductance blockade due to peptide of 3%, which is smaller than in part b). These differences in the peptide induced conductance change might be explained by different orientations of the proteasome inside the pit. If its orientation deviates from the ideal, axial parallel orientation to the pore, changes in proteasome channel conductance have a smaller impact on the overall conductance, i.e. if the proteasome channel would be oriented horizontally inside the pit, ionic current flow through the proteasome channel would not contribute to the overall conductance and hence no channel blockage signal could be observed.

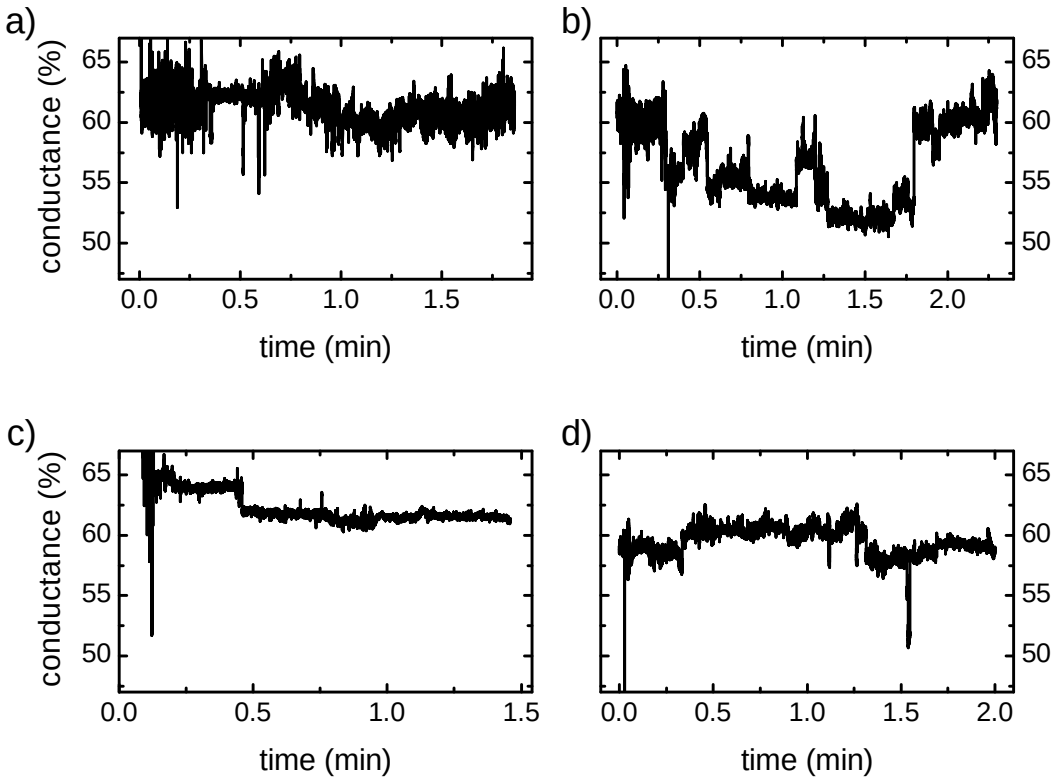

Figure 5.31: a) After adding proteasome molecules to the solution, the conductance decreases to 60% at -150 mV. **b)** After adding 100 nM Suc-LLVY-AMC, again a slight decrease in conductance can be observed. **c)** After releasing the proteasome and subsequent trapping at -150 mV, a similar blockade as in a) is observed. **d)** In the presence of 100 nM Suc-LLVY-AMC.

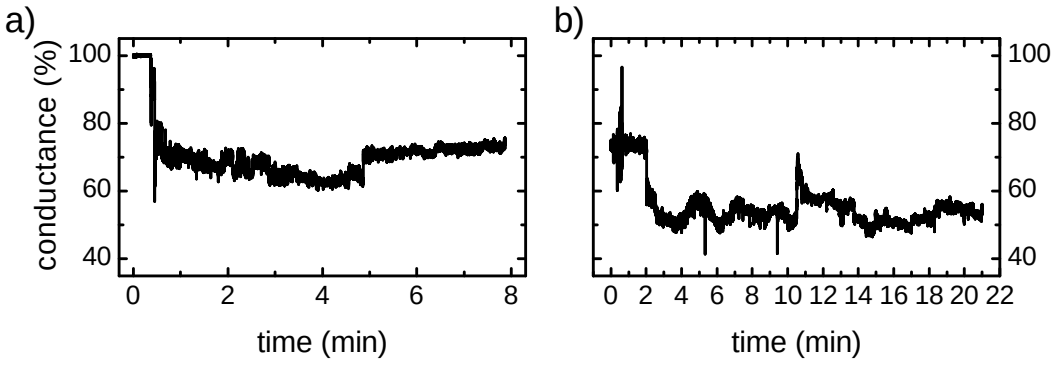

Figure 5.32: a) Proteasome trapping at -200 mV. Stable conductance over 40 minutes (not shown in figure). **b)** Addition of 10 pM Suc-LLVY-AMC and subsequent conductance decrease.

Similar behaviour is found for the same chip 4 weeks later, Fig. 5.32. Due to a trapped proteasome, the conductance decreases to 65–70%. After the addition of peptide, the conductance decreases further to 50–60% between part a) and b).

It is difficult to estimate the conductance blockade of the proteasome channel caused by peptides, because the channel has a nontrivial shape and effects of surface conduction are probably involved due to the small length scale of 2–6 nm. Moreover, the exact position of Suc-LLVY-AMC inside the proteasome is unclear and changes in proteasome conformation might further complicate the problem[107]. Therefore, we only make a crude estimation of the expected, peptide induced conductance change. It is based on a cylindrical proteasome channel geometry with a length of 16 nm and a diameter of 2.4 nm, which is 0.2 nm wider than the smallest constriction in the real proteasome. The pit has a small diameter of 12 nm and a length of 30 nm. The pore has a diameter of 8 nm and a length of 20 nm. The opening angle is assumed to be 16°. Figure 5.33 shows two curves of the calculated conductance change. The upper one shows the best case without leakage currents, where the proteasome is situated tightly at the pore. Here, depending on the blocked volume of the proteasome channel, a maximum conductance blockade of 11% can occur for an 80% blockage of channel volume.

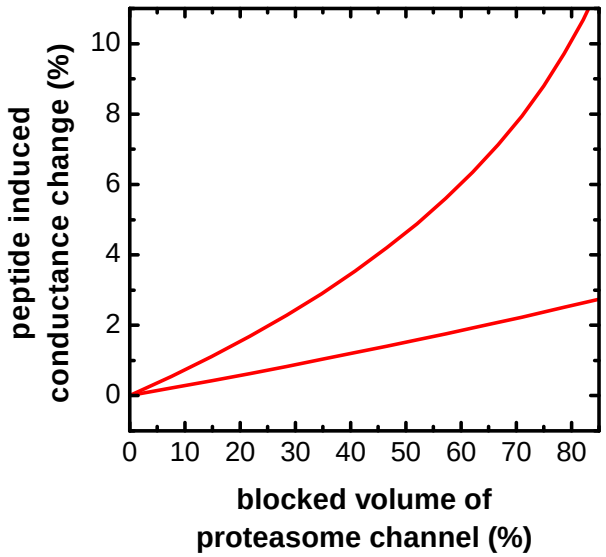

Figure 5.33: Estimation of peptide induced conductance blockade of trapped proteasome. Upper curve shows best case, without leakage currents, lower curve shows conductance blockade for a proteasome to pore distance of 1 nm. Based on $D_{pit} = 12\,nm, L_{pit} = 30\,nm, D_{pore} = 8\,nm, L_{pore} = 20\,nm, \alpha = 16°$

The lower curve represents the more realistic case of a proteasome to pore distance of 1 nm, which results in leakage currents around the proteasome, thus decreasing the peptide signal. Here, a maximum conductance blockade of ∼3% is expected, if the peptide would occupy 80% of the channel volume. However, if we assume a length of ∼3 nm for the length of Suc-LLVY-

AMC and a diameter of 0.6 nm, only 1.2% of channel volume would be blocked by a single peptide. The resulting conductance blockade would be only 0.2%, which is not detectable. The weak point of this calculation is the channel profile.

As shown in Fig. 5.34, the proteasomal channel consists of two ante-chamber (AC) and one central chamber (CC), which are connected by small constrictions. Probably, the proteasome conductance is for the most part determined by the small constrictions at the entrance, exit and between the central- and ante-chamber. If all constrictions would be blocked by a single peptide, the volume blockage would be $\sim$10%. The resulting conductance blockade of $\sim$1% is in the range of the smallest experimentally observed blockades of 3%. However, the large blockades of 10–30% can not be explained with this model. Two possible explanations for the large conductance blockade are incorporation of multiple peptides, and conformational changes upon incorporation of peptide which decrease the channel conductance. At least for eucaryotic proteasome, conformational changes are also proposed in literature[107]. Incorporation of several peptides at the same time could also be possible, as the proteasome has 14 active sites in the central chamber[96]. Due to the variety of parameters which influence the peptide induced conductance blockade, it is very difficult to interpret the available experimental data in detail. Further experiments, i.e. with peptides of different size, are necessary to interpret the observed conductance blockades in a more comprehensive way. Nonetheless, the experiments at room temperature already show that trapping of a single proteasome molecule is possible and that the ionic current through the trapped proteasome is sensitive to addition of peptide substrate, which potentially binds inside the proteasomal channel.

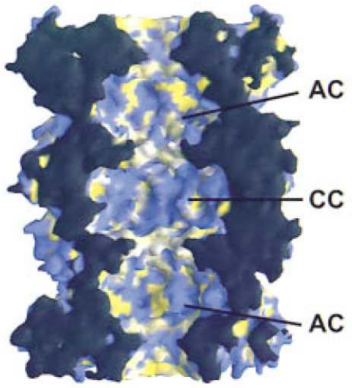

Figure 5.34: Cut-open view of a proteasome molecule. From Baumeister et al.[8]

Proteasome trapping at high temperatures

To increase the temperature of our measurement cell, we used a Julabo heating circulator which was connected to a copper block, and placed the block beneath the inner Faraday cage of our setup. The inner Faraday cage and all water lines were thermally isolated to ensure temperature stability and minimize heating of the headstage. In order to prevent evaporation of liquid from the measurement chamber, we used the pressure chamber described in chapter 4 which is tightly sealed. Temperature was controlled manually by a thermo-couple inside the measurement chamber. As shown in Fig. 5.35 a), the open pore current increases with increasing temperature, which is related to a decreasing viscosity of the solution. Based on the slope of the linear fit in Fig. 5.35 a, $(\mathrm{I(T)} = -1.2 - 0.18 \cdot \mathrm{T})$, we normalized the current in all following graphs to a temperature of 26 °C by multiplying with the measured open pore current at 26 °C (-10.9 nA) and dividing by the calculated open pore current at the particular temperature. It follows that changes in current are now related to changes in pore geometry and proteasome position or conformation. As shown in Fig. 5.35 b), the ionic current standard deviation does not increase with temperature. This seems surprising because thermal and capacitive noise both depend on temperature[103,114,117], but we usually observe also high 1/f-noise in nanopores, which dominates the other noise sources.

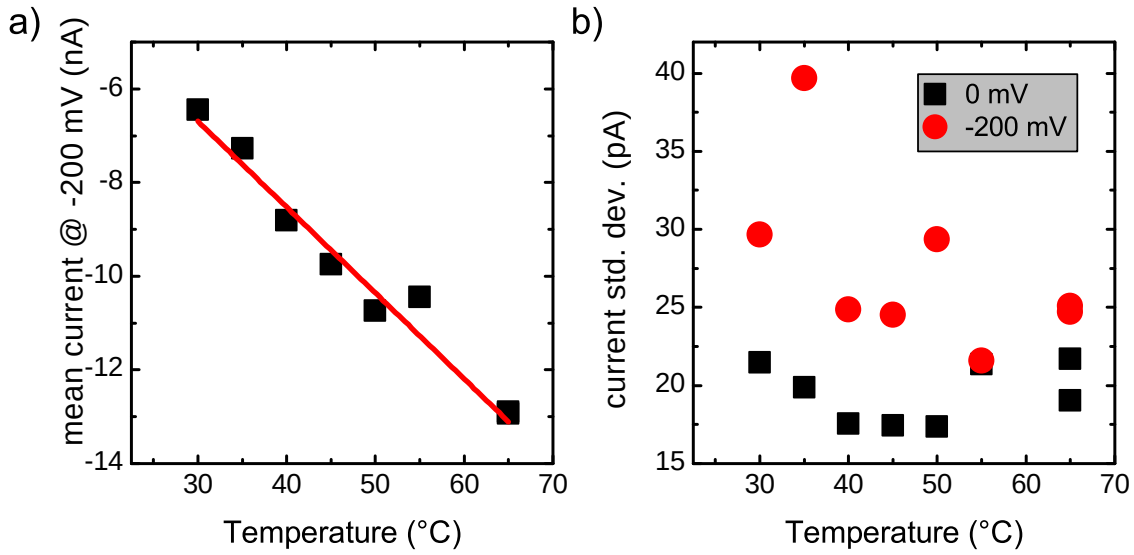

Figure 5.35: a) Temperature dependence of open pore current. Red line depicts a linear fit, the point at 55°C was excluded for fitting. Buffer: 600 mM KCl, 20 mM Tris-HCl, pH 7.2. **b)** Temperature dependent standard deviation of open pore current.

Figure 5.36 shows current-time traces of a trapped proteasome (without peptide) at different temperatures. A molecule was trapped at room temperature (26 °C). After changing the buffer to remove proteasome in solution, the current blockade is still preserved, indicating the tight

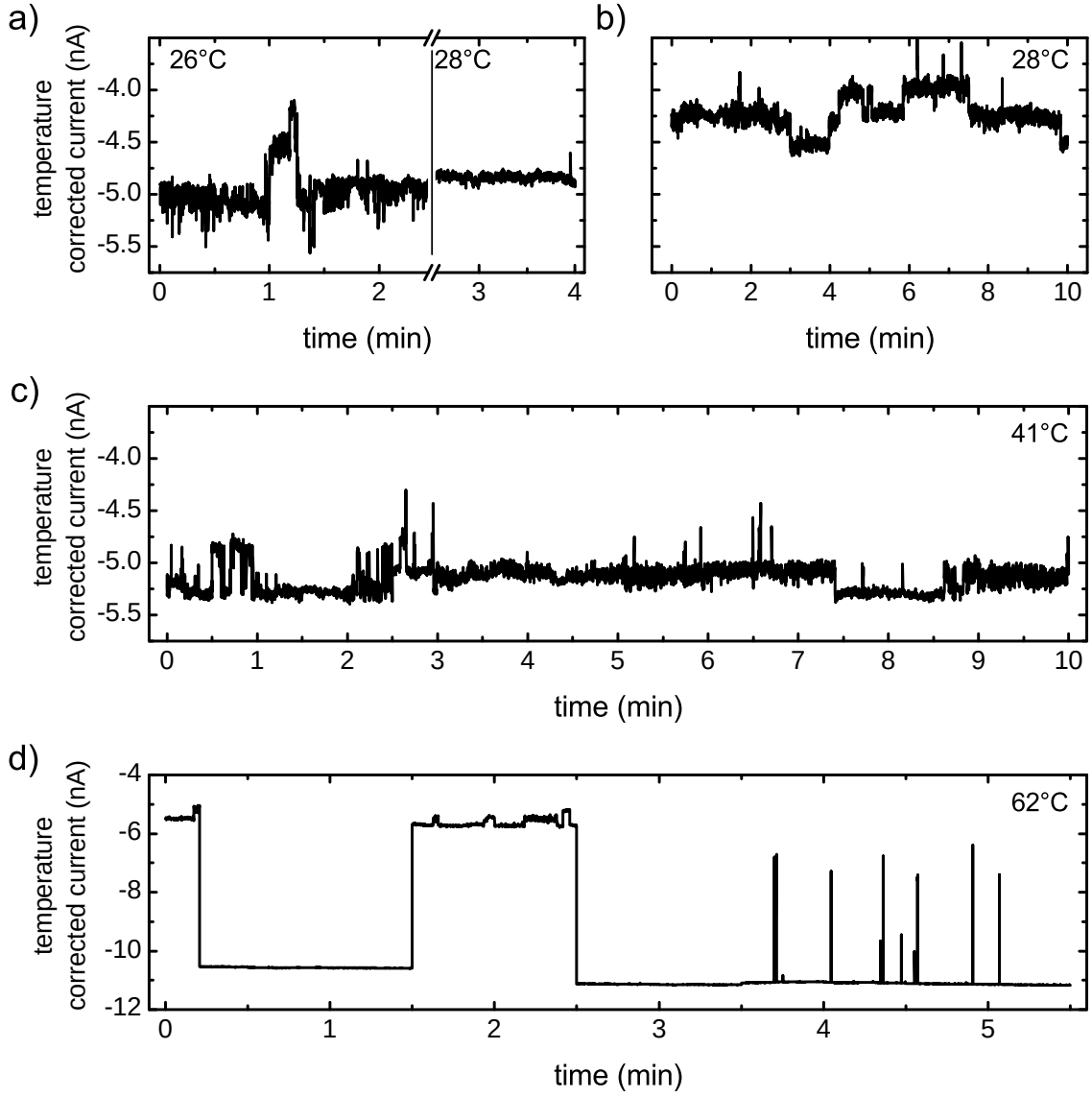

Figure 5.36: Current-time traces of a trapped proteasome at increasing temperatures and -250 mV. **a)** A single proteasome was trapped at 26 °C. At the vertical line, the buffer was changed to remove proteasome in solution. The temperature was increased to 28 °C and the voltage was held constant at -250 mV for 1h. Afterwards, the proteasome is in a stable position (2.5–4 minutes) **b)** Stepwise current fluctuations of 7–8% around -4.25 nA indicate movement of the proteasome or conformational changes. **c)** At 41 °C the baseline shifted to higher currents. **d)** T = 62 °C. A sudden increase in current to -11.1 nA indicates broadening of the pore and loss of the trapping capability. The initial open pore current was 10.9 nA.

anchoring of the proteasome inside the pit pore, even in the absence of an electric field. The buffer exchange is indicated by a vertical line in Fig. 5.36 a). Temperature was then increased to 28 °C and the voltage was set to -250 mV during the experiment. Fig. 5.36 b) shows stepwise fluctuations in current of approximately 5–7% and several short spikes of current blockades. At this point, we can only speculate about the causes, which could be fluctuations of the proteasome position inside the pore, or conformational changes of the proteasome channel. Upon increasing temperature to 41 °C, the same behavior with long lasting steps and short spikes is observed (Fig. 5.36 c)). Furthermore, the current increased from 4.5 to 5.2 nA. As we eliminated the influence of temperature on solution conductivity, this increase can only be caused by either a larger distance of the proteasome from the pit bottom, or by a change in the Si_3N_4 pore geometry. The latter is the most likely due to the observation at 62 °C, shown in Fig. 5.36 d). A sudden increase in current from -5.5 to -10.5 nA indicates loss of the proteasome through the nanopore. After more than 1 minute, another proteasome is captured and blocks the pore for 1 minute (-6 nA). The repeated current increase to -11 nA indicates loss of the proteasome and an increased pore diameter. The open pore current then increases further to -11.2 nA and only transient events are observed which show the characteristic blockade levels and which are thus attributed to proteasome translocations. Due to this unexpected increase in pore diameter, the pit–pore is now not capable anymore of trapping proteasome molecules.
The same behavior was found in a second experiment, Fig. 5.37. During the first 2 minutes shown in Fig. 5.37 a), the initial open pore current is -2.4 nA at a temperature of -50 °C, until a proteasome molecule is trapped. The current is thus blocked to -1.0 nA. The ionic current is then stable for 20 minutes. After exchanging the buffer and an equilibration time of 10 minutes, the ionic current rose to -14 nA, indicating degradation of the pit pore membrane.
A widening of the pore diameter is in fact always found in Si_3N_4 nanopore experiments, but usually on a much slower time scale (see for example Fig. 4.9, where the baseline current at 150 mV increased within 5 days from $\sim$5 to $\sim$8 nA). It seems that the thin membrane of the pit pore device paired with elevated temperatures is much more sensitive to membrane degradation than usual membranes at room temperature. Unfortunately, we could not solve this problem in the time frame of this thesis. A solution to this problem could either be a different material system, which is stable at elevated temperatures, or the use of proteasome molecules from organisms which live at ambient conditions and have their optimum working temperature at 37 °C.

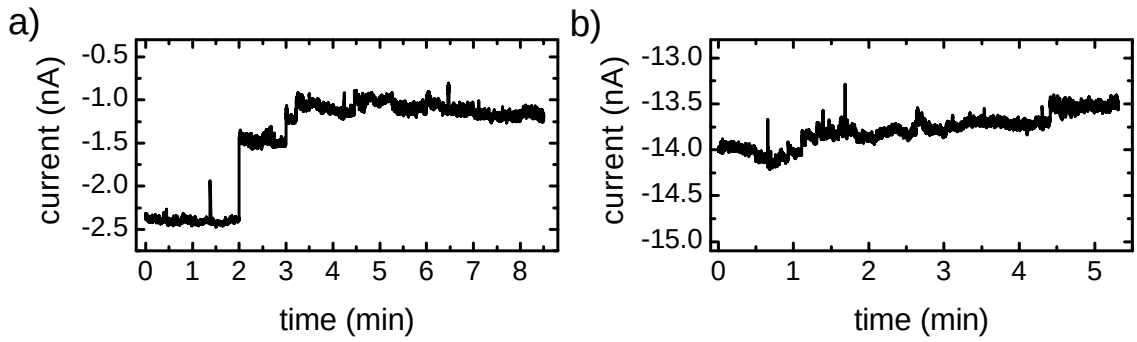

Figure 5.37: Current-time traces of a trapped proteasome at 50 °C and -200 mV. **a)** A single proteasome is trapped after 2 minutes. **b)** After a buffer exchange and equilibration for 10 minutes, the current jumped from -2 to -14 nA, indicating degradation of the pit pore membrane.

5.3.3. Conclusion

The experiments show that proteasome molecules can be reversibly trapped in a solid-state pit-pore device. Albeit the proteasome orientation inside the pit can not be unambiguously identified, we attribute the different conductance states observed in the reversible trapping experiments to different proteasome orientations and positions inside the pit. Due to the good agreement between experimental and simulated conductance states, we propose a more or less uniaxial orientation of protein and pit-pore. This is also supported by the pit geometry itself, which impedes a transverse proteasome orientation at the bottom of the pit due to the small pit diameter. Due to the lack of stability of the Si_3N_4 pores at temperatures above 50 °C, proteasomal peptide breakdown in real time could not be observed. However, the conductance decrease in the trapped state upon addition of peptide substrate suggests an observable effect of proteasome occupation by Suc-LLVY-AMC at room temperature. Further experiments should be carried out with mammalian or yeast proteasome to avoid excessive heating of the membrane. To increase the proteasome signal, the TEM milled pore should be as large as possible but as small as necessary to prevent the proteasome from passing the pore. The pit depth should be between 30–40 nm to increase the proteasome signal while simultaneously ensuring stability of the pore against degradation.

6. An Entropically Driven Nanoplug

6.1. Introduction

Solid-state nanopores might be used as partition and gate to control chemical reactions on a nanochip. It is of great interest to control the pore permeability, i.e. to switch between an open and closed state. The presented nanoplug shows a possibility to do this without continuous application of an external voltage. It utilizes the coiling entropy of a large DNA strand. The plug consists of a spherical nanoparticle, to which a large (48.5 kbp) DNA strand as electrophoretic handle is attached. Upon application of an appropriate voltage across the nanopore, the DNA is dragged along the electric field and through the nanopore. Provided that the attached nanoparticle is larger than the pore, the nanoparticle will clog the pore from one side of the membrane, while the attached DNA strand is situated mostly on the opposite membrane side. The pore is now in a closed state, which is shown schematically in Fig. 6.1. Without applied external potential, the system is determined by the Brownian motion of DNA and bead. The coiled DNA acts as entropy barrier for the nanoparticle, which has to be overcome by the thermal motion of the particle in order to diffuse away from the pore. After a certain time τ_{plug}, the particle has pulled the DNA completely through the pore which is then again in an open state. To close the pore again, a potential has to be applied to trap another particle-DNA conjugate for pore clogging.

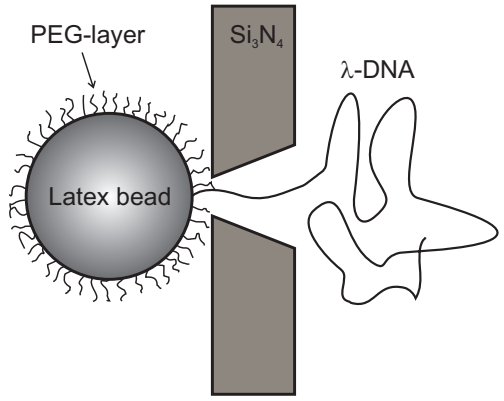

Figure 6.1: Schematic drawing of a nanoplug. Membrane thickness is 50 nm, bead diameter 70 nm, contour length of λ-DNA 16.5 µm.

6.2. Characterization of latex beads

As the size of the bead is a crucial factor for pore clogging, we characterized them first in solution by dynamic light scattering (DLS). Here, the average diameter turned out to be 70 ± 10 nm, which exceeds the nominal diameter of 50 ± 13 nm by 40%. In order to exclude effects from particle coagulation, we also examined particle size by TEM. To this end, a 120 pM bead solution was dried out on a common TEM copper grid. Figure 6.2 shows exemplary beads and sizes.

The average bead size turned out to be 70 ± 10 nm, which is much larger than the manufacturer specification of 50 ± 13 nm. This discrepancy explains the result of DLS measurement. However, the exact bead diameter is not important for the proof-of-principle experiments, as long as the particles are not too small to plug the pore. Furthermore, with the combination of TEM and DLS measurements, we can exclude particle coagulation, which is important for the following work.

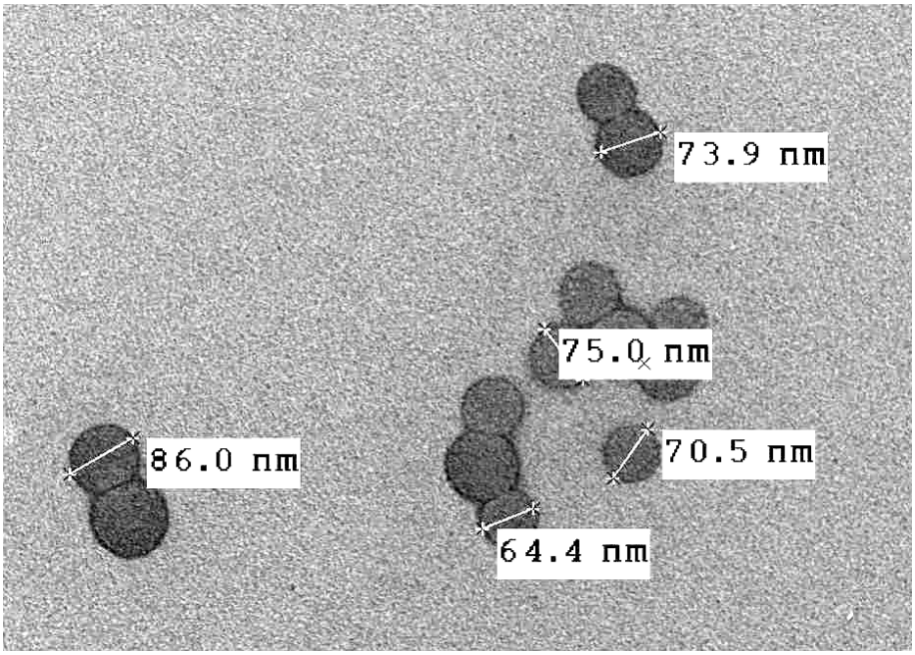

Figure 6.2: TEM micrograph of latex beads. Nominal diameter: 50 nm, real diameter: 70 nm.

6.3. DNA-Bead conjugation

Carboxylate-modified and streptavidin labeled latex beads with a nominal diameter of 50 nm were purchased from Sigma-Aldrich. λ-DNA was purchased from Fermentas. If a later cleaving of DNA on certain positions is desired, the methylation free (dam-) variant of DNA has to be used. In order to couple DNA to the bead, a biotin label has to be attached to one end of the DNA, which can then bind to streptavidin. For this purpose we used the protocol given in detail in a blog (http://biocurious.com/2006/01/14/labeling-l-dna) and in a short way in the work of Zimmerman et al.[135]. We use the polymerase Klenow fragment (exo-) to attach nucleotides (dNTP) and biotin-11-dUTP to one end of the DNA. Excess nucleotides can be removed with a 3 kDa spinfilter. To remove also the polymerases, the modified DNA was cleaned with a Wizard® SV Gel and PCR Clean-Up System (A9281, Promega). This step was necessary in order to avoid clogging of the pore with polymerase enzymes. The cleaned DNA-biotin solution

was then mixed with the streptavidin coated latex beads and equilibrated at least 24 h at room temperature. The bead concentration was chosen at least three times the DNA concentration to ensure that only one DNA strand is attached to a bead. In order to reduce repulsion effects, salt concentration was adjustet to 1 M KCl. After this conjugation step, a tenfold excess of PEG-biotin (polyethyleneglycol, $M_w = 2000$) was added to the DNA-bead mixture and equilibrated for another 24 h. This step was necessary to avoid sticking of the bead at the nanopore entrance.

6.4. Measurement instrumentation & experiments

Simple DC current measurements are not appropriate to measure the presence of the nanoplug in the pore, as this would disturb the entropic nature of the system. We therefore used the Lock-In extension of the HEKA EPC-8 amplifier, to test the pore resistance without applying an effective force. We applied a sinusoid signal with 5 mV amplitude and a frequency of 800 Hz. The Lock-In extension is a software based tool which analyzes the measured current in response to an applied AC voltage. It calculates two conductance values, GS and GM, according to an equivalent circuit of serial resistance (GS) and a capacitance in parallel to a second resistance (GM). This circuit describes a simple membrane with a pore of conductance GM and the access resistance of the measurement cell (GS) between electrode and pore. Inherent to the calculation, only for nonzero voltages both values can be calculated. At zero offset potential, only GM is calculated. However, if the Lock-In is properly calibrated, GM(0 mV) is the correct pore resistance. For nonzero voltages, we calculate $R_{pore} = 1/GM + 1/GS$ as the total pore resistance. In this way, slow fluctuations which occur in GM and inversely in GS can be compensated.

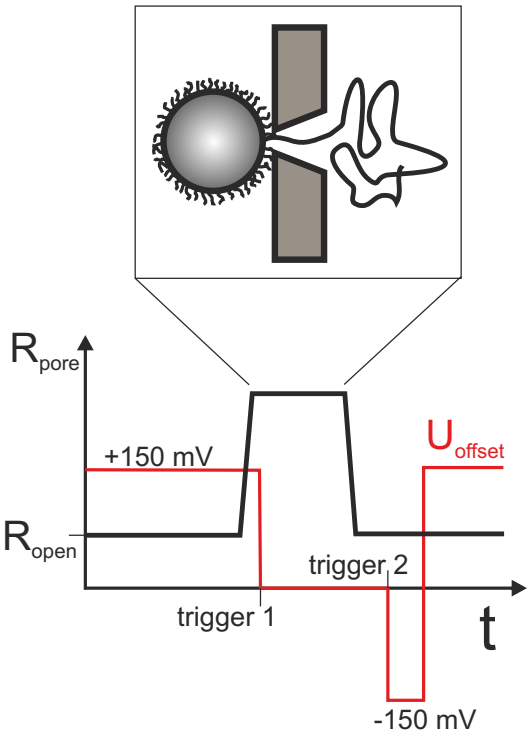

Figure 6.3: Schematic drawing of the automated trapping procedure.

With a custom measurement protocol, the DNA-bead could be trapped and released automatically. This process is drawn schematically in Fig. 6.3: An offset voltage of +150 to +200 mV was applied and the pore resistance was read out every 55 ms. The AC signal for the Lock-In measurement was applied for only 5 ms to disturb the nanoplug–pore system as less as possible. Once a change in resistance occurred due to pore clogging, a predefined trigger switched the offset voltage to 0 mV, leaving the AC Lock-In measurement (every 55 ms for 5 ms) running. With a second trigger, the measure-

ment was terminated if the open pore resistance was reached and a negative voltage was applied for 5 seconds to remove eventually sticky DNA conjugates. A new measurement was thereafter initialized at positive applied potential and trapping of a new bead could start again.

Figure 6.4 a) shows 6 trapping events, recorded at +200 mV. All curves begin with the open pore resistance $\mathrm{R_{open}} = 21$–22 MΩ and then show a sudden increase to $\mathrm{R_{blocked}} = 22.5$–$29$ MΩ. Why some of the curves show apparently different pore resistance values in the closed state (i.e. the red one) remains unclear. For evaluation of the resistance increase due to trapping, we take the last measured value of every curve before switching off the potential. The different open pore resistances at the beginning of each curve can be traced back to a long term drift in the Lock-In circuit. They are of minor relevance, as we only evaluate relative resistance changes, $\Delta\mathrm{R_{trap}} = \mathrm{R_{blocked}} - \mathrm{R_{open}}$, and may be eliminated by frequent calibration of the Lock-In circuit. In Fig. 6.4 b), the voltage is switched at an instance from +200 mV to 0 mV. Approximately 100 ms are lost during switching voltages due to the control software. However, we see clear steps from high to low pore resistance values on a timescale of 2 – 17 seconds. Again we note different open pore resistances and even differences in subsequent trap and release events (same color in Fig. 6.4 a) and b). This shift is also attributed to different behavior of the Lock-In amplifier at 200 and 0 mV, respectively.

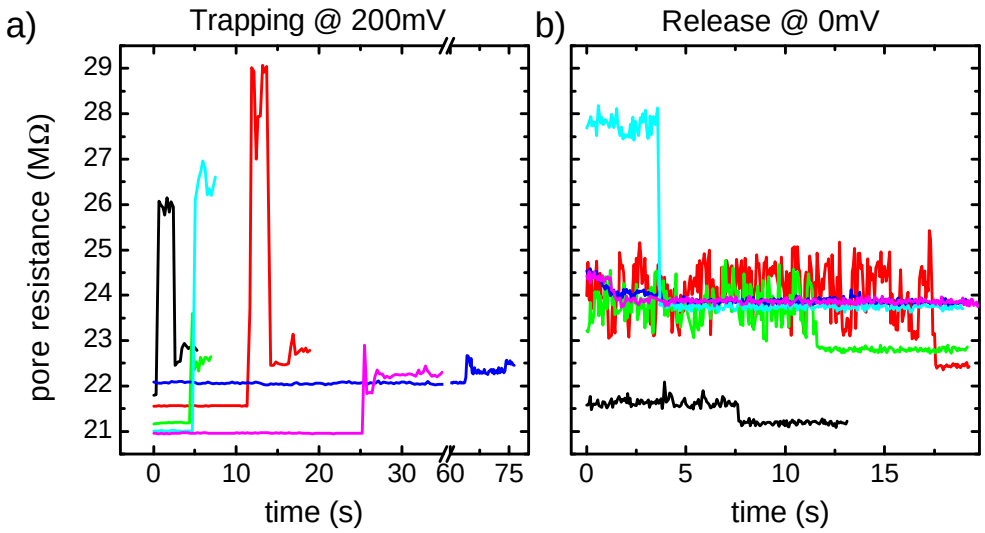

Figure 6.4: a) Various capture events of nanoplugs. The open pore resistance is characterized by low noise amplitude. **b)** Corresponding release events to the capture shown on the left.

However, we may not decide about open and blocked state on basis of the absolute resistance, but on the noise which is generated by random motion of the nanoplug in the pore. $\mathrm{R_{open}}$ is characterized by a low noise value compared to the blocked state. This can be seen more clearly in Fig. 6.5. The black and red trace depict $\mathrm{R_{open}}$ over time for two independent measurements.

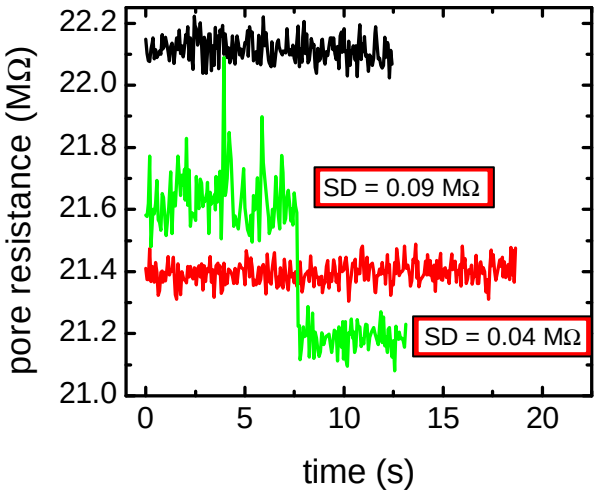

Figure 6.5: Resistance noise of open pore (black and red trace) and blocked pore which gets open (green trace) due to a nanoplug release event. The resistance standard deviation approximately doubles for the blocked state.

Even if they are shifted by 0.7 MΩ, they show the same standard deviation of 40 kΩ. The green trace shows a step, which is due to a nanoplug release event. The part between 0 and 7.5 s shows a standard deviation of 90 kΩ and after the step between 7.5 and 12 s a standard deviation of 35 kΩ. We therefore state that the pore resistance fluctuations, more precisely the standard deviation, is a good indicator of an empty or occupied pore, regardless of the absolute resistance value. For the data shown in Fig. 6.4, the average resistance step due to trapping is 1.8 ± 1.7 MΩ and the step due to release of the nanoplug is 1.4 ± 1.2 MΩ. The slightly larger value for the trapping can be explained by the different applied voltage. While trapping happens at +200 mV, the bead is pushed against the pore, which minimizes ionic currents around the bead. Upon release at 0 mV, the bead has probably moved away slightly from the pore due to the lack of electric force. Therefore we expect for all experiments $\Delta R_{trap} > \Delta R_{release}$.

Unfortunately, only 20% of trapping events are followed by step-like release events. Most often, no step is observed but only the open pore resistance, indicating that no DNA was attached to the bead. In a control experiment, we trapped beads without DNA to ensure that long lasting blockades during release are due to DNA and not due to sticky beads. This is shown in Fig. 6.6. The left side shows different trapping events of latex beads (600 pM) at +200 mV. The average resistance increase is $\sim 8 \pm 2$ MΩ. The variance in onset of pore blockage resembles the equilibrium constant of the trapping process k_{on}, which is determined by particle concentration and applied voltage. After switching the applied potential to 0 mV, only the open pore resistance is measured, without any glance of pore blockage. This shows that beads without attached DNA diffuse away from the pore in less than ∼100 ms, which is the approximate time the system needs to switch from +200 mV to 0 mV. This is in accordance with the expected bead diffusion time. We determined the diffusivity of the beads by DLS to be ~ 3 µm^2 s^{-1}. The diffusion time for a distance of 100 nm (where we expect no influence on the pore resistance) is therefore ∼3 ms, which is far beyond the time resolution of the system.
Obviously, the resistance increase for the beads without DNA (8 MΩ) seems to be much larger than for the previously shown bead-DNA conjugate (1 MΩ). We explain this effect by a different degree of PEGylation for the two measurements. While we usually incubate the DNA-bead PEG mixture for at least 24 h, incubation time for the bead-only measurement was only 1 h. The large PEG molecules (MW 2000) act usually as spacer between bead and pore surface. Therefore, with a complete PEG layer around the bead, it can not approach the pore opening as close as

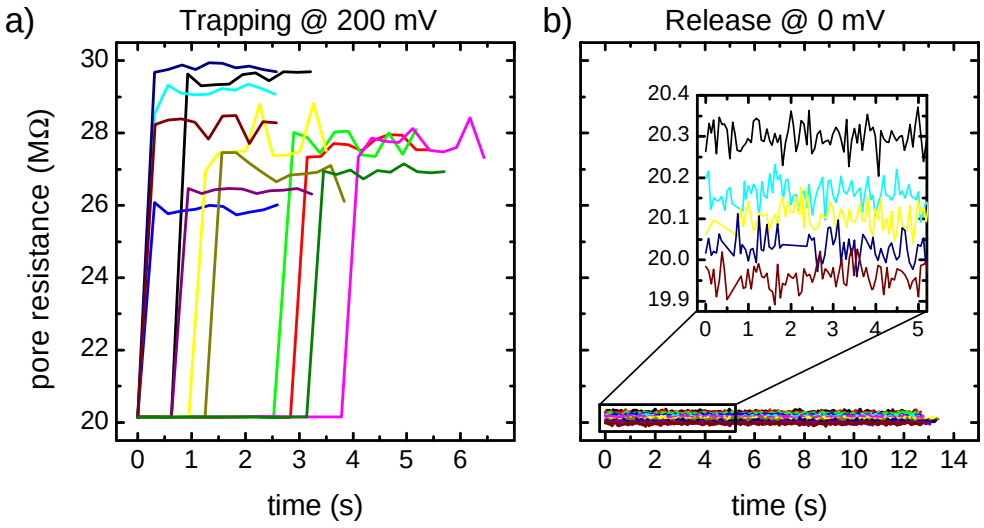

Figure 6.6: a) Trapping of latex beads without attached DNA. $R_{open} = 20$ MΩ. Different onsets of pore blockage resemble k_{on} of the capture process, which is low due to the high dilution of beads (600 pM). **b)** Release of beads at zero voltage. No blocked state is observed, diffusion of beads away from the pore is faster than the time resolution of the system.

without PEG. Moreover, the PEG layer is accessible to ions in solution. Together, both effects increase the ionic current around the PEGylated sphere and reduce the conductance blockade during trapping. Figure 6.7 shows histograms of the resistance change for DNA-bead conjugates with 24 h PEG incubation time (red) and for beads with PEG incubation time of 1 h (green). Clearly, the 1 h incubation leads to four times larger resistance changes than the 24 h incubation. This shows that the beads with 1 h incubation time approach the pore much more closely than the 24 h incubation beads. The PEG layer is only sparsely developed in the first case and we see the necessity to incubate the bead-PEG mixture over a long period of time, i.e. 24 h if we want to prevent sticking of the bead to the pore. The fact that we did not observe sticking of the beads without DNA can be explained by the smaller electrophoretic force, if no DNA is present. The spacing effect of PEGylation is even larger than suggested by Fig. 6.7. The presence of DNA for the red data increases the resistance change by ∼0.8 MΩ, as determined by free DNA translocations.

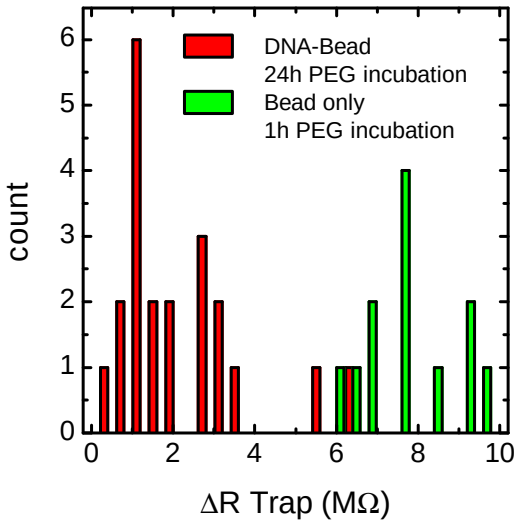

Figure 6.7: Resistance increase for trapping events of PEGylated DNA-beads (red) and sparsely PEGylated latex beads (green).

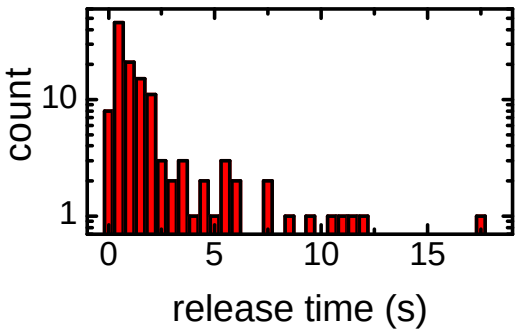

Figure 6.8: Release time histogram of all recorded release events from four different pores.

Finally, we summarize evaluable release events from four different pores with diameters between 20 and 30 nm. Fig. 6.8 shows a release time histogram for all events with a maximum at 0.5 s. Only few events were observed above 8 s.
Figure 6.9 shows scatter plots of release time and resistance change of the individual pores. Red lines indicate the resistance range of observed blockades caused by free DNA molecules. This range is in good agreement with the observed release events, which indicates that the resistance change due to the nanoplug originates from the presence of a single DNA molecule inside the pore. In all experiments, the majority of release events lasted between 0.5 and 2 s. Only in Fig. 6.9 b), a second cluster around 6 s appears, whose origin is unclear. We can exclude the presence of two DNA molecules in the pore, as this would lead to a larger $\Delta R_{release}$. The presence

of λ-DNA duplexes is also very unlikely, because the single strand overhangs of λ-DNA should be filled up with nucleotides. However, we can not exclude that duplexes form very rapidly after the DNA sample was heated up to 70°C and during the biotinylation, before all overhangs could be filled up. If this would be the case, DNA of double length could increase the release time.

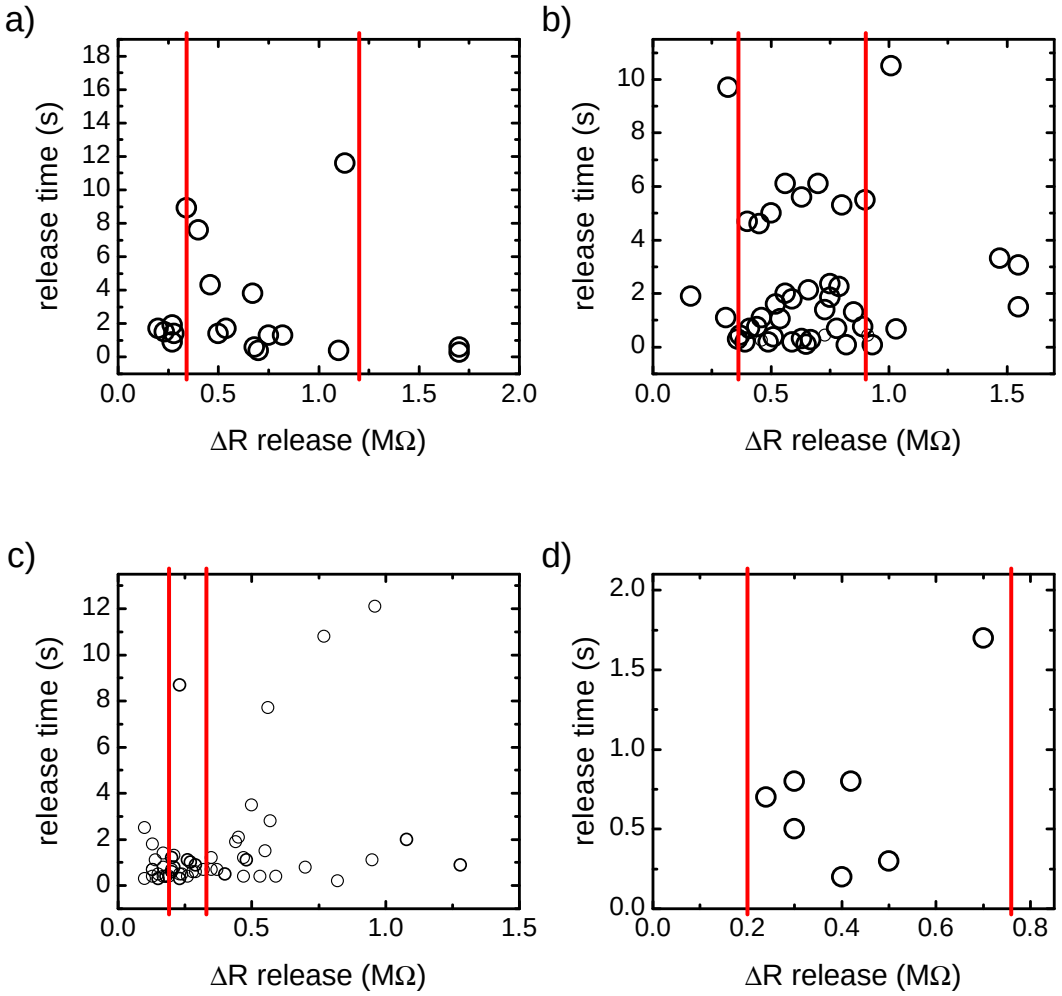

Figure 6.9: a)–d) Release time and corresponding resistance drop of 4 different pores. Red lines indicate resistance range of observed free DNA translocations. Pore diameter calculated from open pore resistance: a: 16 nm, b: 18 nm, c: 22 nm, d: 15 nm.

Figure 6.10 summarizes release events from different pores. Therefore, the resistance change is normalized to the area defined by the calculated pore diameter. Figure 6.10 b) shows the release time histogram. The most probable release time is at 1–1.5 s, and a second and third population can be suspected around 6 s and at 11 s, though the few events hamper a meaningful interpretation. The release time should of course be influenced by the pore diameter, but for the small

range of 15–22 nm, we could not detect significant differences. Similar experiments on DNA diffusion have been performed by Pedone and Langecker[87]. They investigated the escape of λ-DNA through a 30 nm wide pore from a small cavity and observed escape times in the range of $\sim$10 seconds. Figure 6.10 c) shows the resistance drop histogram of release events. Most events are at 60 – 300 MΩ nm^2. The broad distribution is attributed to the large fluctuation of ionic current during the blocked state and to the variety of fluctuations between different release events. This is illustrated for example in Fig, 6.4 b), red and black line. The physical nature of these fluctuations are typically interactions between DNA and the Si_3N_4 surface. As we have also learned from the previous studies on protein translocations, these surface interactions result in a broad distribution of translocation times.

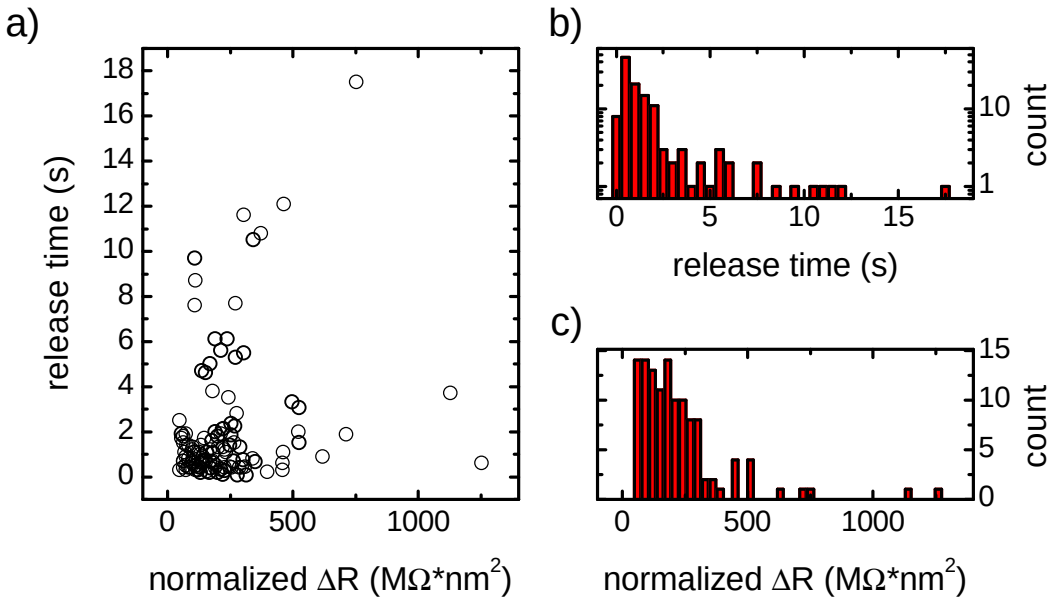

Figure 6.10: a) Release time vs. normalized resistance drop for 4 different pores. Resistance drop is normalized to the pore area, according to the calculated pore diameters. **b)** Histogram of release times. **c)** Histogram of normalized current drop.

6.5. Conclusion

We showed that single nanoparticle-DNA conjugates can be trapped in solid-state nanopores, thereby blocking part of the ionic current through the pore. Without external electric forces, the conjugate is released from the trapped state by diffusion on a timescale of seconds. The potential application of the nanoplug to prevent other macromolecules from crossing the pore is difficult to prove, as current blockades from single molecules will not be visible in the large noise signal in the blocked state and, more important, with the presented Lock-In measurement technique time resolution is limited to 50–100 ms, which is too slow to detect single molecule translocations happening on a timescale of $\sim$0.1–1 ms. To increase the blocking time of the conjugate, nanopores with diameter smaller than 10 nm should be used. Then the entropy barrier for DNA to escape the pore would increase and thus slow down the escape of the conjugate. It would thus be possible to inspect influences of DNA length on trapping time to characterize the system in a more fundamental way.

7. Outlook

Electroosmotic Flow

Chapter 4 shows the importance of electroosmotic effects in protein sensing. Neglecting it might lead to false conclusions about the translocation process. For our experiments on EOF, we used approximately cylindrical pores and calculations are based on a cylindrical pore shape. However, we have seen for the Proteasome translocations, that EOF also acts in conical pores. It would therefore be interesting to determine the zeta potential and magnitude of EOF in conical pores and check if the pore shape influences the magnitude of EOF.

Obviously, the most elegant way would be to control EOF externally. We made first experiments connecting a metallized pore to a third electrode, but we had to struggle with leakage currents between the gold surface and the two Ag/AgCl electrodes. Immobilization of a self-assembled monolayer reduced this effect partly, but was still not sufficient to control the Debye layer polarity inside the pore. Other groups reported on the control of protein translocation through embedded electrode devices, where the electrodes are separated from solution by oxide or metal-oxide layers[51,52,76]. However, direct observation of EOF or measurements of zeta potential in such embedded electrode devices are still missing. Another way of avoiding leakage currents could be the covering with a lipid bilayer, as demonstrated by Meyer et al. for Si_3N_4 nanopores[133]. Experiments would have to proof if these bilayers build a tight seal and eliminate leakage current or not.

Proteasome Trapping

The pit-pore structure turned out to be appropriate for trapping single proteasome molecules. However, the instability of the membrane at temperatures above 50°C precluded real-time observation of peptide breakdown. To circumvent this problem, one could try to fabricate a similar pit-pore structure with a different material system and test its stability at elevated temperatures. One could for example think of fabricating a conical pore in a solid-state material and cover the small opening with a layer of graphene. As shown by several groups recently, nanopores can be structured in graphene layers with nanometer precision[35,71,94] and covered with a layer of titanium dioxide[71] to improve insulation. The only problem with the large solid-state pore fabricated by e-beam lithography is, that the small opening faces towards the etch pit of the silicon substrate, which precludes adhesion of a graphene layer on the small opening of the conical pore. However, this problem could be solved by fabricating nanopores with the track etching technique, as demonstrated by Vlassiouk et al.[118]. With this technique, the narrow opening of

the conical pore is situated at the top layer of the nanopore chip and hence enables adhesion of a graphene layer.

Another strategy would be the use of proteasome from an organism, which is active at lower temperatures than proteasome from a thermophilic organism. Therefore, mammalian proteasome could be used or proteasome from yeast[31], because proteins from simple organisms are generally more stable. In this case, heating of the measurement cell to 25–35°C would probably be sufficient to observe a proteolytic activity on the timescale of seconds and the Si_3N_4 membrane is stable at least over several hours at this temperature.

A. Appendix I

A.1. Effect of electroosmotic flow on streptavidin translocations

Similar results as the ones reported in Chap. 4 for avidin are obtained for a different protein, streptavidin. Its shape and size is similar to avidin, but it shows different charging states with pH. It carries a positive charge of +20 mV at pH 4, a negative charge of -13 mV at pH 8 and is approximately charge neutral at the intermediate pH 6. At pH 10, streptavidin carries a negative charge of -18 mV, but due to the low event rate of 0.1 s^{-1} (see Tab. A.1), we did not consider it for further evaluation. Figure A.1 shows the equivalent experimental situations to the ones shown in Fig. 4.8 at pH 4, 6 and 8. At pH 4, the positively charged protein traverses the pore towards the positively charged electrode. At pH 8, despite a very small event rate, the negatively charged protein traverses the pore towards the negatively charged electrode. Both situations can only be explained by considering the EOF, dragging the molecules against the electric field through the pore. At the intermediate pH 6, streptavidin is close to its isoelectric point. Again, the EOF enhances (-150 mV) or weakens (+150 mV) the diffusion of proteins through the pore.

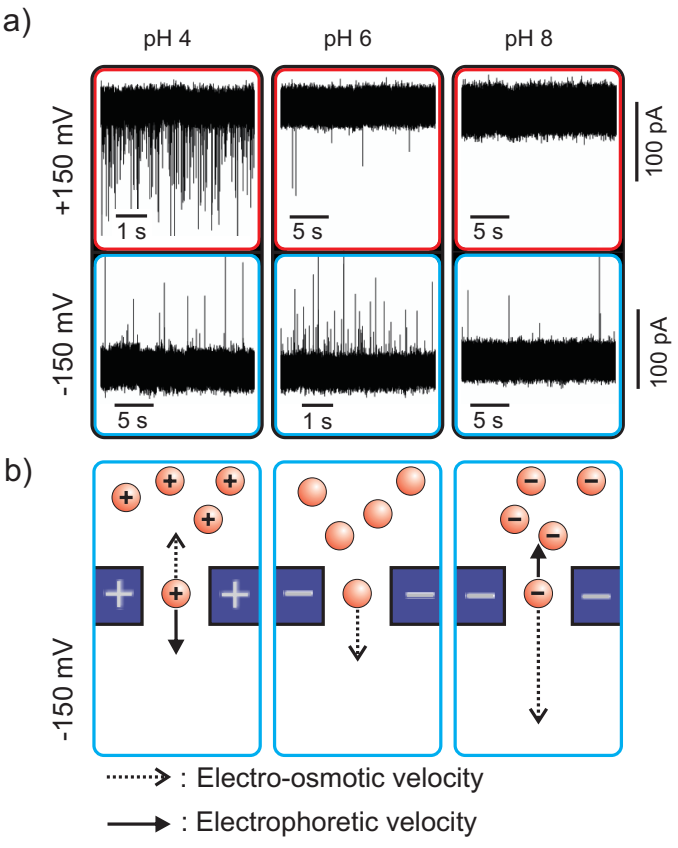

Figure A.1: pH dependent translocation of streptavidin.

In contrast to avidin, we observe only a single regime in the time distribution histograms, Fig. A.2. The translocation times are between 50 and 70 µs. Comparing pH 8 and 6, we observe an increase in translocation time by 15%, and between pH 6 and 4 an increase by 9%. This correlates with the decrease in $\Delta\zeta$ at least qualitatively. Table A.1 summarizes the evaluation of streptavidin translocations.

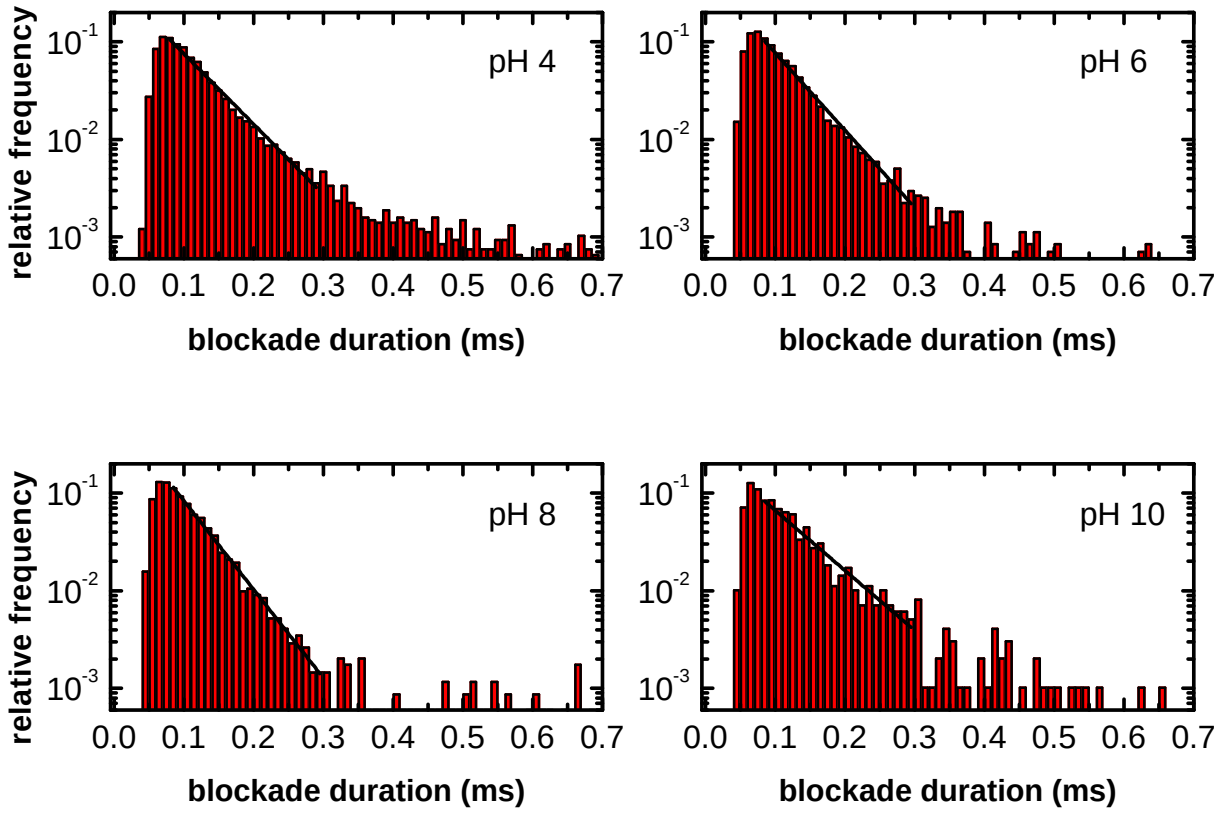

Figure A.2: Time constants of streptavidin translocation events for different pH values at -150 mV. Black lines indicate linear fits in semi-log scale. Results are summarized in Tab. A.1.

For the voltage dependent event rate, shown in Fig. A.3, we observe the same effect as previously mentioned for avidin (Fig. 4.13). We show only the situation at pH 4 and 6, because the event rate at the other pH values was much lower and is thus difficult to compare. At pH 4 the event rate decreases with increasing potential from -50 mV on, whereas at pH 6, the rate decreases from -100 mV on and is roughly a factor of 5 larger than at pH 4. This can be attributed to the different protein-pore interaction. Whereas we observe a strong repulsive behavior at pH 4, where protein and pore are positively charged, the pore gets negatively charged at pH 6 and the protein is roughly neutral, potentially favoring transient adsorption.

Table A.1: Protein (streptavidin) and pore zeta potentials and translocation event rates.

		pH 4	pH 6	pH 8	pH 10
zeta potentials (at high ionic strength)					
ζ_{protein} (mV)[1]		10 ± 3	0 ± 3	-6 ± 3	-18 ± 3
ζ_{pore} (mV)[2]		8 ± 2	-9 ± 2	-21 ± 2	-22 ± 2
$\Delta\zeta$ (mV)		$\sim$2	$\sim$9	$\sim$15	$\sim$4
protein–pore interaction		rep.	rep./attr.	rep.	rep.
event rate (s^{-1})	trans = -150 mV	0.7	12	0.4	0.1
	trans = +150 mV	36	0.5	0	0
τ_1 (µs)		60	55	50	70

[1] 50% low ionc strength value. [2] Measured in 400 mM KCl solution.

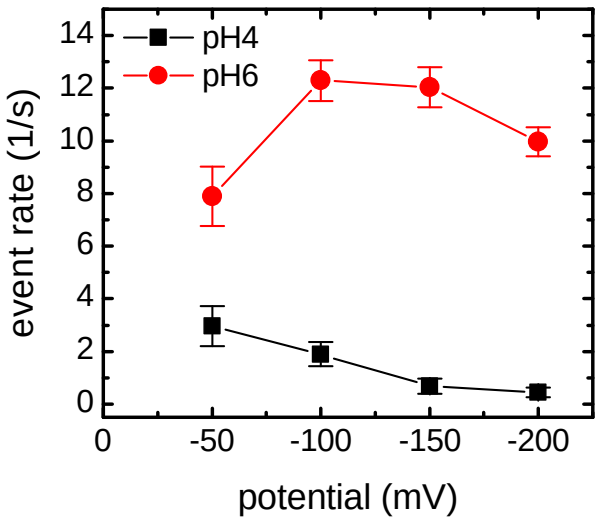

Figure A.3: Potential dependent event rate of streptavidin translocation experiments at different pH. Avidin concentration: 40 nM (pH 4, pH 6), 800 nM (pH 8, pH 10).

B. Appendix II

The protein translocations presented in chapter 4 were analyzed with a matlab routine as previously described[85]. Here, a moving average baseline was created and each point of the trace was checked for crossing a predefined threshold, which then marked the onset of a blockade event. This method is especially suited for signals with small signal-to-noise ratio and for signals with a large amount of 1/f-noise, when a global threshold would lead to many missed events. The drawback is the long processing time, because we loop through every single data point of the trace. The usual computing time on our Dell workstation was ∼30–60 s for a 30 s trace. For analysis of proteasome translocations presented in chapter 5 we take a different approach to minimize computation time. Due to the excellent signal to noise ratio, we could apply a global threshold for peak detection. Together with the use of vectorized calculations, detection of the relevant data is done in a fraction of time. The relevant data is peak on- and off-set, and all further calculations, i.e. level detection, can be restricted to this part. Complete analysis of a 30 s trace can now be performed in ∼2–6 s, which is an enormous saving of time.

B.1. Data evaluation with Matlab

Not every code line will be described here, but only the basic concept and structure of the code, so it will be easier for others to use or modify it. A convention which has evolved since we developed matlab scripts for evaluation of current blockades is to name current blockades "peaks", no matter if the blockade is upward or downward with respect to the baseline. Two matlab script files (m-files) are needed to evaluate multiple data files, which have to be available in matlab binary format. The first one, ExecFindPeakProt_xx, (xx is the version number) is used to loop through the raw data files. It detects all binary *.mat files in a destination folder and opens only one file at a time for evaluation. Evaluation results are then stored in variables which are extended with results from the remaining data files in subsequent evaluation runs. Usually, the variables which contain the collected results have an 'All' in their file name, for example `PeaksOnlyAll`, which contains the data points of current blockades only, separated by small fractions of the baseline. After all data files have been evaluated, statistical calculations are carried out, and color map plots and histograms are created. Finally, all data is stored in arrays and the arrays are stored in a single structure, called Savelist. In a structure, arrays of arbitrary dimension can be saved and exported for further use of the evaluation results with other programs like Origin™.
The second m-file is 'FindPeakProt_xx.m', which handles only one raw data file at a time, called 'DataArray'. For a 30 s trace with a sample time of 4 µs, this array contains 7.5 million data

points. As we evaluate signals with high S/N-ratio and straight baseline, we can use a global threshold to minimize the data for evaluation:

```
Peaks = find(DataArray < I_base - 7*Standard_dev);
```

Here, `Standard_dev` is the baseline standard deviation, determined by a script without the contribution of the blockade events. The '7' is a parameter which has to be chosen by the user and which determines the threshold below the baseline (`I_base`) for peak detection. This is shown for an exemplary peak in Fig. B.1.

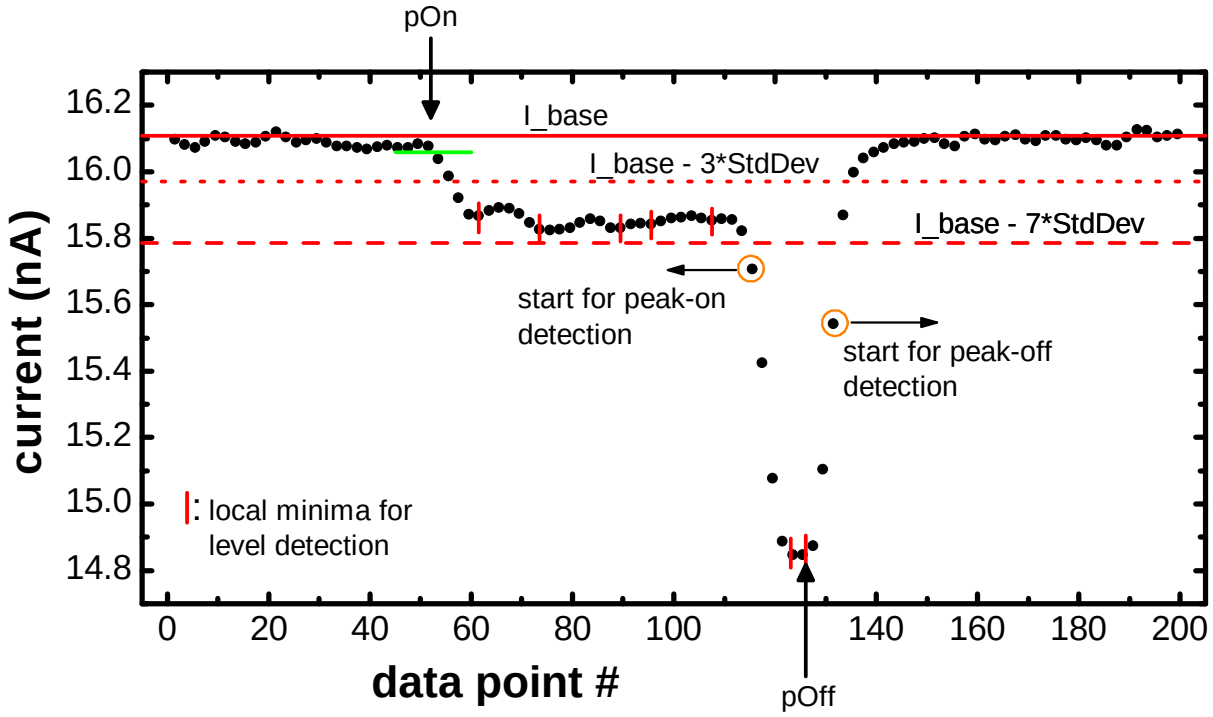

Figure B.1: Exemplary current blockade (peak) to illustrate peak and level detection. The original data is down-sampled by a factor of 2 to improve visibility of individual data points.

The red, straight line is the global baseline, and the red, dashed line is seven times the baselines' standard deviation apart. The array `Peaks` contains the index of data points in `DataArray` from below this dashed line. In a next step, we detect the transition between one peak and the next. Because the `find` routine from matlab does not copy the data values into `Peaks`, but gives indices to the data points in `DataArray`, transitions between peaks in `Peaks` are characterized by skips in the index increment. Within a peak, the index increment is always 1, but between two peaks the index increment is >1, because there are always baseline data points between two peaks. At each index irregularity in `Peaks` we can now start the detection of *Peak-Off* for the one peak and *Peak-On* for the subsequent peak, as depicted in Fig. B.1. This is done by:

```
2  while DataArray(pOff) < I_base - 3*Standard_dev;
           pOff = pOff + 1;
```

```
 4  end;

 6  PeakBaseline(numPeak,2) = mean(DataArray(pOff:pOff + buffer));

 8  while DataArray(pOff) >= DataArray(pOff-1);
          pOff = pOff - 1;
10  end;

12  PeakData(numPeak,2) = pOff;
    ...
14  numPeak = numPeak+1;
    pOn = Peaks(i+1);
16  while DataArray(pOn) <  mean(DataArray(pOff+10:pOff+210)) - ...
     Standard_dev;
          pOn = pOn - 1;
18  end;

20  PeakData(numPeak,1) = pOn;
    PeakBaseline(numPeak,1) = mean(DataArray(pOn - buffer:pOn));
```

Here, `pOff` and `pOn` are positions in `DataArray` and `numPeak` is a counter for the peak which is processed. `PeakBaseline` collects the baseline values for each peak to calculate its correct height. Even if we use a global baseline to define the threshold for peak detection, we calculate a local baseline for each peak to balance drift effects. The calculated baseline is an average over a number of data points defined by `buffer`, usually set to 200. Two baseline values are calculated for each peak, one to the left of `pOn` and one to the right of `pOff`, and the mean value between the two is taken for all further calculations.
After the baseline at the pOff–side is calculated in line 6, the following while-loop at line 8 corrects peak-off for the filter risetime. Due to delay introduced by the Bessel-filter, the current blockade does not end when it reaches the baseline, but when the current begins to decrease from the blocked level to the baseline. In most cases, this point can be approximated with the last minimum of the blockade below the baseline, as indicated with the arrow in Fig. B.1. The while-loop at line 2 is also necessary, because it can happen that another blockade level lies above the peak detection threshold. If we would only decrement the initial `pOff` until the last minimum, some peaks would misleadingly end at the wrong position. For detection of peak-on, we align the threshold with respect to the formerly detected peak-off (line 16). The threshold is depicted in Fig. B.1 as green line, and `pOn` is the data point above this line. This procedure is necessary because proteasome translocations often produce very long and small blockade levels at the beginning, when the molecule hits the rim of the pore entrance. Therefore, averaging over data points directly left to the initial `pOn` could lead to a wrong onset, which is actually the first blockade level.
Now that we have detected peak-on, peak-off and the baseline for each blockade event, we can continue with detection of the intrinsic level structure. In order to save processing time, we concentrate on local minima for level detection: in Fig. B.1, local minima between peak-on and peak-Off are drawn as vertical red lines. Obviously, this peak has two levels. The first level contains 5 minima and the second level contains two minima. The characteristic feature of the

local minima is, that minima within one level have very similar current values, and minima of different levels show a larger distance on the current-axis. We therefore can check subsequent minima, starting with peak-on and the first minima, for their current spacing `DiffMinima`[1]:

```
22  DiffMinima(1,1) = DataArray(PeakMinima(numPeak,1)) - DataArray(...
     PeakData(numPeak,1));
    DiffMinima(2:end,1) = DataArray(PeakMinima(numPeak,2:lastElem)) - ...
     DataArray(PeakMinima(numPeak,1:(lastElem -1)));
24  ...
    LevelMinima(:,1) = find(abs(DiffMinima) < pLvlMin *10e-12);
26  if size(LevelMinima,1) > 0;
            LevelMinima(:,2) = PeakMinima(numPeak, LevelMinima(:,1));
28  end;
```

`PeakMinima` is a formerly calculated $m \times n$ array which contains the minima–positions for the m'th peak in the m'th row and the column number n is given by the peak with the most minima (n minima). `LevelMinima` contains the indices of `DiffMinima` where the values are smaller than `pLvlMin*10e-12` and who therefore belong to the same level. `pLvlMin` is a user-defined parameter to adjust the allowed deviation between subsequent minima of the same level. It depends on the filter frequency and the level spacing. For the data shown in chapter 5.2.1 where the filter was set to 100 kHz, we used `pLvlMin = 10`. The position of minima on the same level is assigned to the second column of `LevelMinima` in line 30.
The next step is the evaluation of `LevelMinima`. For the exemplary peak shown in Fig. B.1, this is not very complicated. We check if there are subsequent indices in LevelMinima incremented by 1, which are part of a level. We then calculate the average and standard deviation between the first and last minima of this level and define the level off-set as the point where the blockade crosses a defined threshold below the average, depending on the standard deviation. However, level structure can be quite diverse and problems arise when a level consists of a single minima. This happens especially when a small filter, e.g. 10 kHz, is used. The single minima are not detected in line 25, and special care must be taken to evaluate them in a meaningful manner. (The irregularities in blockade fine structure necessitates many code lines and loops. A detailed explanation is beyond the scope of this Appendix.) After all levels are characterized, we do a second "clean-up" run to eliminate unnecessary levels. Unnecessary means, that two subsequent levels have the same or similar blockade height or are of length zero. This can happen in the former level detection routine.
To prevent falsely interpreted blockades from being processed further, we now check each blockade for the plausibility of evaluation. Therefore, the area of the computed blockade shape is compared with the area of the actual blockade. In the following evaluation, we use only the "good blockades", whose ratio between calculated and real blockade area is between 0.8 and 1.5. The only figure that is independent of the goodness of level evaluation is the event duration, because the internal level structure does not influence determination of peak-on and peak-off, as shown in line 2–18. The event duration is therefore calculated over all events. Based on the ratio between calculated and real blockade area, our method of event evaluation has a typical yield of 75–90% "good blockades", i.e. blockades that are described sufficiently accurate by our evaluation. Most

[1]Note that the vectorized form in line 23 is much fast than a for-loop which compares minima i with i+1.

problems arise from short peaks, where the calculated area depends critically on pOn and pOff. The following is a list of Savelist entries that are exported for characterization of translocation behavior. It is created in the form `Savelist.Name = variable`. The short description below each variable clarifies the meaning:

`PeakScatterMaxH`

1st column: event duration [µs]. 2nd column: maximum blockade height [%]. For scatter plots.

`PeakScatterMaxColor`

1st column: binned event duration [µs]. 2nd column: binned maximum blockade height [%]. 3rd column: number of events. For color map plots. Binning is performed with the script `ColormapLin(ScatterPlotData, bin time, bin blockade height)`.

`PeakScatterSum`

1st column: event duration [µs]. 2nd column: mean blockade height [pA], calculated by dividing the blocked charge (PeakSum) by the event duration. For scatter plots, e.g. Fig. 5.6.

`LevelScatter`

1st column: level duration [µs]. 2nd column: level blockade height related to the baseline [%]. For scatter plots.

`LevelScatterColor`

1st column: binned level duration [µs]. 2nd column: binned level blockade height related to the baseline [%]. 3rd column: number of levels. For scatter plots, i.e. Fig. 5.8. Binning is performed with the script `ColormapLin(ScatterPlotData, bin time, bin blockade height)`.

`LevelScatterRel`

1st column: level duration [µs]. 2nd column: level blockade height related to subsequent level [%]. For scatter plots.

`LevelScatterPos`

1st column: level duration [µs]. 2nd column: level blockade height related to the baseline [%]. For scatter plots. Only events with increasing level blockades are considered for evaluation.

`LevelScatterNegOnce`

1st column: level duration [µs]. 2nd column: level blockade height related to the baseline [%]. For scatter plots. Only events with increasing level blockades and a maximum of one decreasing blockade are considered for evaluation.

`LevelScatterNegTwice`

1st column: level duration [µs]. 2nd column: level blockade height related to the baseline [%]. For scatter plots. Only events with increasing level blockades and a maximum of two decreasing blockades are considered for evaluation.

`LevelScatterShortPeaks`

1st column: level duration [µs]. 2nd column: level blockade height related to the baseline [%]. For scatter plots. Only events with a single minimum (no level) are considered for evaluation.

`ProbOfLevel`

1st column: number of levels that a certain event consists of. 2nd column: probability that an event consists of X number–of–levels. [%].

`LevelPercent`

1st column, line 1: fraction of short peaks (only one minimum). Line 2: fraction of events with only increasing blockades. Line 3: fraction of events with a maximum of one decreasing level blockade. Line 4: fraction of events with a maximum of two decreasing level blockades. Line 5: fraction of events where the maximum blockade is the first or second level. Line 6: fraction of events with decreasing level blockades only. Line 7: fraction of events that can not be attributed to one of the aforementioned categories. All fractions in [%].

`PeakWidthOnly`

1st column: event duration of all detected events, independent of the goodness of level evaluation [µs].

`PeakSumStat`

1st column: average ratio of calculated and real peak area (blocked charge) for all peaks (events) in a raw data file. 2nd column: standard deviation of average values from first column. 3rd column: average ratio of calculated and real peak area for all evaluated peaks. 4th column: standard deviation of all average values, refers to column 3.

`PercentGoodPeaks`

The fraction of peaks that are used for level characterization [%].

C. Appendix III

C.1. Protocols

C.1.1. Optical lithography

- Clean wafer with aceton and isopropanol.
- Protect one side with photo resist S1818 by painting it with a Q-Tip, dry on hotplate at 120°C for 10 minutes.
- Spin photo resist Shipley S1805 at 10000 rpm for 40 seconds.
- Softbake in oven at 90°C for 15 minutes.
- Align wafer in mask aligner, exposure time 4 seconds.
- Develop wafer for 35 seconds, rinse with water, dry with nitrogen.
- Hardbake in oven at 120°C for 30 minutes.
- Reactive ion etching, depends on etch-system, etch 50 nm Si_3N_4 and 10 nm SiO_2.
- Clean chips with aceton and Q-Tip, especially the protected side, this will be the side for e-beam lithography. Rinse with isopropanol, dry with nitrogen.

C.1.2. Electron beam lithography

- Take care that there are no photo resist residues on the wafer surface.
- Dilute e-beam resist ZEP520 with Anisol 1:1.4, be careful not to produce air bubbles.
- Spin ZEP at 4000 rpm for 90 seconds.
- Hotplate at 180°C for 3 minutes.
- Make small scratch on one side of the wafer for later adjustments in the SEM.
- SEM operation: 30 keV, Aperture 10 µm, Dot Dose 0.025 fAs, minimal Dose for full exposure 18 - 20.

  Developing:

- Put wafer in Amylacetate for 60 s under gentle stirring.
- Put wafer in MIBK for 10 s under gentle stirring.
- Blow-dry with nitrogen.
- Reactive Ion Etching. Parameters depend on etch system.
- Remove ZEP: Put in NMP for 20–30 min and wipe resist gently with a Q-Tip.
- Rinse with isopropanol and blow-dry with nitrogen.

C.1.3. DNA-bead conjugation

In a first step, dam- λ-DNA (methylation free) has to be labeled with biotin-11-dUTP.

- Heat up λ-DNA to 70°C for 10 min to break up circular DNA strands, then cool down to RT.
- Add Klenow fragment exo-, dATP, dGTP and biotin-dUTP.
- Incubate 2h @ 37°C.
- Elute excess biotin-dUTP with 3kDa Spinfilter.
- Add dNTP's and Klenow fragement exo-.
- Incubate 30-40 min @ 37°C.
- Purify modified DNA with Wizard® SV Gel and PCR Clean-Up System (A9281, Promega)

The biotinylated DNA can now be coupled to streptavidin coated beads. To avoid binding of multiple DNA molecules to one bead, we mix DNA:bead approximately 1:3. After DNA-bead conjugation, we saturated the streptavidin molecules on the bead with PEG. A typical mixture consists of:

- 10 nM DNA
- 30 nM beads
- 1 M KCl
- 20 mM Tris pH9
- incubate $\sim$24 h
- add PEG-Biotin (MW2000) to final concentration of $\sim$300 nM
- incubate $\sim$24 h

C.1.4. KCl conductance

The conductance of potassium chloride solution is necessay for many calculations related to nanopore experiments. It can be interpolated with a linear fit between 100 mM and 1 M, as shown in Fig. C.1. Data points depict measured values of KCl solution with Tris buffer in concentration of 10–50 mM and different pH values.

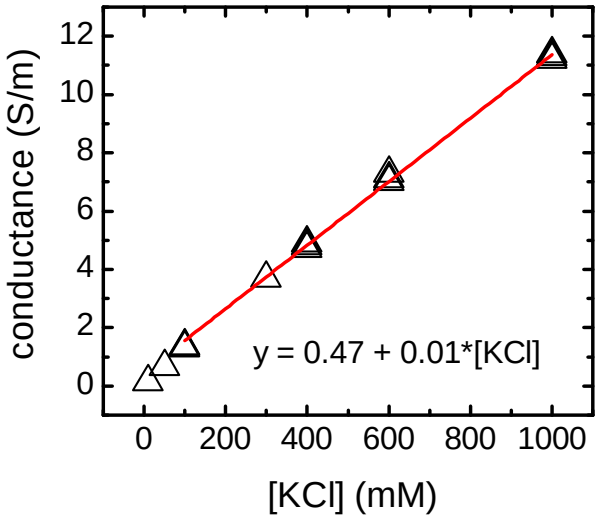

Figure C.1: Conductance of aqueous KCl solution at 25°C. Red line depicts a linear fit between 0.1 M and 1 M KCl.

Bibliography

[1] **Adamczyk, Z. and Van De Ven, T. G. M.** (**1981**). "Deposition of brownian particles onto cylindrical collectors." *Journal of Colloid and Interface Science*, 84(2): 497–518.

[2] **Ai, Y., Zhang, M., Joo, S. W., Cheney, M. A., and Qian, S.** (**2010**). "Effects of Electroosmotic Flow on Ionic Current Rectification in Conical Nanopores." *The Journal of Physical Chemistry C*, 114(9): 3883–3890.

[3] **Akopian, T. N., Kisselev, A. F., and Goldberg, A. L.** (**1997**). "Processive Degradation of Proteins and Other Catalytic Properties of the Proteasome from Thermoplasma acidophilum." *Journal of Biological Chemistry*, 272(3): 1791–1798.

[4] **Apel, P.** (**2001**). "Track etching technique in membrane technology." *Radiation Measurements*, 34(1-6): 559–566.

[5] **Apel, P. Y., Korchev, Y. E., Siwy, Z., Spohr, R., and Yoshida, M.** (**2001**). "Diode-like single-ion track membrane prepared by electro-stopping." *Nuclear Instruments and Methods in Physics Research Section B: Beam Interactions with Materials and Atoms*, 184(3): 337–346.

[6] **Arai, T. and Norde, W.** (**1990**). "The behavior of some model proteins at solid-liquid interfaces 1. Adsorption from single protein solutions." *Colloids and Surfaces*, 51(0): 1–15.

[7] **Balme, S., Janot, J.-M., Berardo, L., Henn, F., Bonhenry, D., Kraszewski, S., Picaud, F., and Ramseyer, C.** (**2011**). "New Bioinspired Membrane Made of a Biological Ion Channel Confined into the Cylindrical Nanopore of a Solid-State Polymer." *Nano Letters*, 11(2): 712–716.

[8] **Baumeister, W., Walz, J., Zuhl, F., and Seemüller, E.** (**1998**). *The Proteasome : Paradigm Of A Self-Compartmentalizing Protease*, volume 92. Cell Press, Cambridge, MA, ETATS-UNIS.

[9] **Bell, N. A. W., Engst, C. R., Ablay, M., Divitini, G., Ducati, C., Liedl, T., and Keyser, U. F.** (**2012**). "DNA Origami Nanopores." *Nano Letters*, 12(1): 512–517.

[10] **Borissenko, L. and Groll, M.** (**2007**). "20S Proteasome and Its Inhibitors: Crystallographic Knowledge for Drug Development." *Chemical Reviews*, 107(3): 687–717.

[11] **Bousse, L., Hafeman, D., and Tran, N.** (**1990**). "Time-dependence of the chemical response of silicon nitride surfaces." *Sensors and Actuators B: Chemical*, 1(1-6): 361–367.

[12] **Bousse, L., Mostarshed, S., Van Der Shoot, B., de Rooij, N. F., Gimmel, P., and Göpel, W.** (**1991**). "Zeta potential measurements of Ta2O5 and SiO2 thin films." *Journal of Colloid and Interface Science*, 147(1).

[13] **Bousse, L. J. and Mostarshed, S.** (**1991**). "The zeta potential of silicon nitride thin films." *J. Electroanal. Chem.*, 302: 269–274.

[14] **Bousse, L. J., Mostarshed, S., and Hafeman, D.** (**1991**). "Combined measurement of surface potential and zeta potential at insulator/electrolyte interfaces." In "Solid-State Sensors and Actuators, 1991. Digest of Technical Papers, TRANSDUCERS '91., 1991 International Conference on," pages 502–505.

[15] **Branton, D., Deamer, D. W., Marziali, A., Bayley, H., Benner, S. A., Butler, T., Di Ventra, M., Garaj, S., Hibbs, A., Huang, X., Jovanovich, S. B., Krstic, P. S., Lindsay, S., Ling, X. S., Mastrangelo, C. H., Meller, A., Oliver, J. S., Pershin, Y. V., Ramsey, J. M., Riehn, R., Soni, G. V., Tabard-Cossa, V., Wanunu, M., Wiggin, M., and Schloss, J. A.** (**2008**). "The potential and challenges of nanopore sequencing." *Nat Biotech*, 26(10): 1146–1153.

[16] **Bruus, H.** (**2008**). *Theoretical microfluidics*, volume 18. Oxford University Press.

[17] **Burgreen, D. and Nakache, F. R.** (**1964**). "Electrokinetic Flow in Ultrafine Capillary Slits1." *The Journal of Physical Chemistry*, 68(5): 1084–1091.

[18] **Chen, D., Frezza, M., Schmitt, S., Kanwar, J., and P. Dou, Q.** (**2011**). "Bortezomib as the First Proteasome Inhibitor Anticancer Drug: Current Status and Future Perspectives." *Current Cancer Drug Targets*, 11(3): 239–253.

[19] **Chen, P. and et al.** (**2009**). "Fast single-step fabrication of nanopores." *NANOTECHNOLOGY*, 20(1): 015 302.

[20] **Chen, P., Gu, J., Brandin, E., Kim, Y. R., Wang, Q., and Branton, D.** (**2004**). "Probing Single DNA Molecule Transport Using Fabricated Nanopores." *Nano Lett.*, 4(11): 2293–2298.

[21] **Chih Jen, L. and et al.** (**2006**). "Fabrication of symmetric sub-5 nm nanopores using focused ion and electron beams." *NANOTECHNOLOGY*, 17(13): 3264.

[22] **Coulter, W. H.** (**1953**). "U.S. Patent No. 2,656,508."

[23] **Dahlmann, B., Kuehn, L., Grziwa, A., Zwickl, P., and Baumeister, W.** (**1992**). "Biochemical properties of the proteasome from Thermoplasma acidophilum." *European Journal of Biochemistry*, 208(3): 789–797.

[24] **Danelon, C., Santschi, C., Brugger, J., and Vogel, H.** (**2006**). "Fabrication and Functionalization of Nanochannels by Electron-Beam-Induced Silicon Oxide DepositionÂ ." *Langmuir*, 22(25): 10 711–10 715.

[25] **Dekker, C.** (**2007**). "Solid-state nanopores." *Nature Nanotechnology*, 2(4): 209.

[26] **DeSorbo, W.** (**1979**). "Ultraviolet effects and aging effects on etching characteristics of fission tracks in polycarbonate film." *Nuclear Tracks*, 3(1-2): 13–32.

[27] **Drews, O., Wildgruber, R., Zong, C., Sukop, U., Nissum, M., Weber, G., Gomes, A. V., and Ping, P.** (**2007**). "Mammalian Proteasome Subpopulations with Distinct Molecular Compositions and Proteolytic Activities." *Molecular & Cellular Proteomics*, 6(11): 2021–2031.

[28] **Evans, E. and Ritchie, K.** (**1997**). "Dynamic strength of molecular adhesion bonds." *Biophysical Journal*, 72(4): 1541–1555.

[29] **Felderer, K. C.** (**2006**). *Untersuchungen zur Substrattranslokation in das 20S-Proteasom aus Thermoplasma acidophilum*. Ph.D. thesis, Technische Universität München.

[30] **Firnkes, M., Pedone, D., Knezevic, J., Döblinger, M., and Rant, U.** (**2010**). "Electrically Facilitated Translocations of Proteins through Silicon Nitride Nanopores: Conjoint and Competitive Action of Diffusion, Electrophoresis, and Electroosmosis." *Nano Letters*, 10(6): 2162–2167.

[31] **Fischer, M., Hilt, W., Richter-Ruoff, B., Gonen, H., Ciechanover, A., and Wolf, D. H.** (**1994**). "The 26S proteasome of the yeast Saccharomyces cerevisiae." *FEBS Letters*, 355(1): 69–75.

[32] **Fleischer, R. L., Price, P., and Walker, R.** (**1975**). *Nuclear tracks in solids: principles and applications*. Univ. of California Press, Berkeley.

[33] **Fologea, D., Ledden, B., McNabb, D. S., and Li, J.** (**2007**). "Electrical characterization of protein molecules by a solid-state nanopore." *Applied Physics Letters*, 91: 053 901.

[34] **Freedman, K. J., Jürgens, M., Prabhu, A., Ahn, C. W., Jemth, P., Edel, J. B., and Kim, M. J.** (**2011**). "Chemical, Thermal, and Electric Field Induced Unfolding of Single Protein Molecules Studied Using Nanopores." *Analytical Chemistry*, 83(13): 5137–5144.

[35] **Garaj, S., Hubbard, W., Reina, A., Kong, J., Branton, D., and Golovchenko, J. A.** (**2010**). "Graphene as a subnanometre trans-electrode membrane." *Nature*, 467(7312): 190–193.

[36] **Green, N. M.** (**1963**). "AVIDIN. 4. Stability at extremes of pH and dissociation into sub-units by guanidine hydrochloride." *Biochem. J.*, 89: 609–620.

[37] **Gregg, E. C. and Steidley, K. D.** (**1965**). "Electrical Counting and Sizing of Mammalian Cells in Suspension." *Biophysical Journal*, 5(4): 393–405.

[38] **Gu, L. Q., Cheley, S., and Bayley, H.** (**2003**). "Electroosmotic enhancement of the binding of a neutral molecule to a transmembrane pore." *Proceedings of the National Academy of Sciences*, 100(26): 15 498.

[39] **Gustafsson, J., Mikkola, P., Jokinen, M., and Rosenholm, J. B.** (**2000**). "The influence of pH and NaCl on the zeta potential and rheology of anatase dispersions." *Colloids and Surfaces A: Physicochemical and Engineering Aspects*, 175(3): 349–359.

[40] **Hall, A. R., Scott, A., Rotem, D., Mehta, K. K., Bayley, H., and Dekker, C.** (**2010**). "Hybrid pore formation by directed insertion of [alpha]-haemolysin into solid-state nanopores." *Nat Nano*, 5(12): 874–877.

[41] **Hall, J. E.** (**1975**). "Access resistance of a small circular pore." *The Journal of general physiology*, 66(4): 531–2.

[42] **Han, A., Creus, M., Schuermann, G., Linder, V., Ward, T., de Rooij, N., and Staufer, U.** (**2008**). "Label-Free Detection of Single Protein Molecules and Protein-Protein Interactions Using Synthetic Nanopores." *Anal. Chem.*, 80(12): 4651–4658.

[43] **Han, A., Schrmann, G., Mondin, G., Bitterli, R. A., Hegelbach, N. G., de Rooij, N. F., and Staufer, U.** (**2006**). "Sensing protein molecules using nanofabricated pores." *Applied Physics Letters*, 88: 093 901.

[44] **Harame, D. L., Bousse, L. J., Shott, J. D., and Meindl, J. D.** (**1987**). "Ion-sensing devices with silicon nitride and borosilicate glass insulators." *Electron Devices, IEEE Transactions on*, 34(8): 1700–1707.

[45] **He, Y., Gillespie, D., Boda, D., Vlassiouk, I., Eisenberg, R. S., and Siwy, Z. S.** (**2009**). "Tuning Transport Properties of Nanofluidic Devices with Local Charge Inversion." *Journal of the American Chemical Society*, 131(14): 5194–5202.

[46] **Howorka, S. and Siwy, Z.** (**2009**). "Nanopore analytics: sensing of single molecules." *Chemical Society Reviews*, 38(8): 2360–2384.

[47] **Hunter, R.** (**1981**). *Zeta Potential in Colloid Science*. Academic Pr.

[48] **Jin, P., Mukaibo, H., Horne, L. P., Bishop, G. W., and Martin, C. R.** (**2010**). "Electroosmotic Flow Rectification in Pyramidal-Pore Mica Membranes." *Journal of the American Chemical Society*, 132(7): 2118–2119.

[49] **Jovanovic-Talisman, T., Tetenbaum-Novatt, J., McKenney, A. S., Zilman, A., Peters, R., Rout, M. P., and Chait, B. T.** (**2009**). "Artificial nanopores that mimic the transport selectivity of the nuclear pore complex." *Nature*, 457(7232): 1023–1027.

[50] **Jubery, T. Z., Prabhu, A. S., Kim, M. J., and Dutta, P.** (**2012**). "Modeling and simulation of nanoparticle separation through a solid-state nanopore." *Electrophoresis*, 33(2): 325–333.

[51] **Karnik, R., Castelino, K., and Majumdar, A.** (**2006**). "Field-effect control of protein transport in a nanofluidic transistor circuit." *Applied Physics Letters*, 88(12): 123 114–3.

[52] **Karnik, R., Fan, R., Yue, M., Li, D., Yang, P., and Majumdar, A.** (**2005**). "Electrostatic Control of Ions and Molecules in Nanofluidic Transistors." *Nano Letters*, 5(5): 943–948.

[53] **Keyser, U. F., Dorp, S. v., and Lemay, S. G.** (**2010**). "Tether forces in DNA electrophoresis." *Chemical Society Reviews*, 39: 939–947.

[54] **Kim, M. J., Wanunu, M., Bell, D. C., and Meller, A.** (**2006**). "Rapid fabrication of uniformly sized nanopores and nanopore arrays for parallel DNA analysis." *Adv. Mater*, 18: 3149–3153.

[55] **King, T. L., Gatimu, E. N., and Bohn, P. W.** (**2009**). "Single nanopore transport of synthetic and biological polyelectrolytes in three-dimensional hybrid microfluidic/nanofluidic devices." *Biomicrofluidics*, 3(1): 012 004–11.

[56] **Kirby, B. J. and Hasselbrink, E. F.** (**2004**). "Zeta potential of microfluidic substrates: 1. Theory, experimental techniques, and effects on separations." *Electrophoresis*, 25(2): 187–202.

[57] **Kisselev, A., v.Â d.Â Linden, W. A., and Overkleeft, H.** (**2012**). "Proteasome Inhibitors: An Expanding Army Attacking a Unique Target." *Chemistry & Biology*, 19(1): 99–115.

[58] **Knezevic, J.** (**2012**). *Protein Analysis with switchDNA Biosensor*. Ph.d. thesis, Technische Universität München.

[59] **Kowalczyk, S. W., Kapinos, L., Blosser, T. R., Magalhaes, T., van Nies, P., LimRoderick, Y. H., and Dekker, C.** (**2011**). "Single-molecule transport across an individual biomimetic nuclear pore complex." *Nat Nano*, 6(7): 433–438.

[60] **Li, J., Gershow, M., Stein, D., Brandin, E., and Golovchenko, J. A.** (**2003**). "DNA molecules and configurations in a solid-state nanopore microscope." *Nature Materials*, 2: 611–615.

[61] **Li, J., Stein, D., McMullan, C., Branton, D., Aziz, M., and Golovchenko, J.** (**2001**). "Ion-beam sculpting at nanometre length scales." *Nature*, 412(6843): 166–169.

[62] **Li, N., Yu, S., Harrell, C. C., and Martin, C. R.** (**2004**). "Conical Nanopore Membranes. Preparation and Transport Properties." *Analytical Chemistry*, 76(7): 2025–2030.

[63] **Limpert, E., Stahel, W. A., and Abbt, M.** (**2001**). "Log-normal Distributions across the Sciences: Keys and Clues." *BioScience*, 51(5): 341–352.

[64] **Lin, G., Li, D., de Carvalho, L. P. S., Deng, H., Tao, H., Vogt, G., Wu, K., Schneider, J., Chidawanyika, T., Warren, J. D., Li, H., and Nathan, C.** (**2009**). "Inhibitors selective for mycobacterial versus human proteasomes." *Nature*, 461(7264): 621–626.

[65] **Lobry, L. and Ostrowsky, N.** (**1996**). "Diffusion of Brownian particles trapped between two walls: Theory and dynamic-light-scattering measurements." *Physical Review B*, 53(18): 12 050.

[66] **Löwe, J., Stock, D., Jap, B., Zwickl, P., Baumeister, W., and Huber, R.** (**1995**). "Crystal structure of the 20S proteasome from the archaeon T. acidophilum at 3.4 A resolution." *Science*, 268(5210): 533–539.

[67] **Lyklema, J.** (**2001**). "Surface conduction." *Journal of Physics: Condensed Matter*, 13(21): 5027.

[68] **Lyklema, J. and Minor, M.** (**1998**). "On surface conduction and its role in electrokinetics." *Colloids and Surfaces A: Physicochemical and Engineering Aspects*, 140(1-3): 33–41.

[69] **Martin, C. R., Nishizawa, M., Jirage, K., and Kang, M.** (**2001**). "Investigations of the Transport Properties of Gold Nanotubule Membranes." *The Journal of Physical Chemistry B*, 105(10): 1925–1934.

[70] **Maxwell, J. C.** (**1904**). "A Treatise on Electricity and Magnetism." In "A Treatise on Electricity and Magnetism," volume Vol. 1, page 440. Clarendon Press, Oxford, (3rd edn) edition.

[71] **Merchant, C. A., Healy, K., Wanunu, M., Ray, V., Peterman, N., Bartel, J., Fischbein, M. D., Venta, K., Luo, Z., Johnson, A. T. C., and Drndić, M.** (**2010**). "DNA Translocation through Graphene Nanopores." *Nano Letters*, 10(8): 2915–2921.

[72] **Mikolajick, T., Kühnhold, R., Schnupp, R., and Ryssel, H.** (**1999**). "The influence of surface oxidation on the pH-sensing properties of silicon nitride." *Sensors and Actuators B: Chemical*, 58(1-3): 450–455.

[73] **Miller, S., Young, V., and Martin, C.** (**2001**). "Electroosmotic Flow in Template-Prepared Carbon Nanotube Membranes." *Journal of the American Chemical Society*, 123(49): 12 335–12 342.

[74] **Mitsui, T., Stein, D., Kim, Y.-R., Hoogerheide, D., and Golovchenko, J. A.** (**2006**). "Nanoscale Volcanoes: Accretion of Matter at Ion-Sculpted Nanopores." *Physical Review Letters*, 96(3): 036 102.

[75] **Movileanu, L.** (**2009**). "Interrogating single proteins through nanopores: challenges and opportunities." *Trends in Biotechnology*, 27(6).

[76] **Nam, S.-W., Rooks, M. J., Kim, K.-B., and Rossnagel, S. M.** (**2009**). "Ionic Field Effect Transistors with Sub-10 nm Multiple Nanopores." *Nano Letters*, 9(5): 2044–2048.

[77] **Niedzwiecki, D. J., Grazul, J., and Movileanu, L.** (**2010**). "Single-Molecule Observation of Protein Adsorption onto an Inorganic Surface." *Journal of the American Chemical Society*, 132(31): 10 816–10 822.

[78] **Nitsche, J. M. and Balgi, G.** (**1994**). "Hindered Brownian Diffusion of Spherical Solutes within Circular Cylindrical Pores." *Industrial & Engineering Chemistry Research*, 33(9): 2242–2247.

[79] **Obi, I., Ichikawa, Y., Kakutani, T., and Senda, M.** (**1989**). "Electrophoresis, Zeta potential and Surface Charges of Barley Mesophyll Protoplasts." *Plant Cell Physiol.*, 30(1): 129–135.

[80] **Ocola, L. E. and Stein, A.** (**2006**). "Effect of cold development on improvement in electron-beam nanopatterning resolution and line roughness." volume 24, pages 3061–3065. AVS.

[81] **Ohshima, H.** (**1994**). "A simple expression for Henry's function for the retardation effect in electrophoresis of spherical colloidal particles." *Journal of Colloid and Interface Science*, 168(1): 269–271.

[82] **Ott, D. E., Coren, L. V., Sowder, R. C., Adams, J., and Schubert, U.** (**2003**). "Retroviruses Have Differing Requirements for Proteasome Function in the Budding Process." *Journal of Virology*, 77(6): 3384–3393.

[83] **Oukhaled, A., Cressiot, B., Bacri, L., Pastoriza-Gallego, M., Betton, J.-M., Bourhis, E., Jede, R., Gierak, J., Auvray, L., and Pelta, J.** (**2011**). "Dynamics of Completely Unfolded and Native Proteins through Solid-State Nanopores as a Function of Electric Driving Force." *ACS Nano*, 5(5): 3628–3638.

[84] **Oukhaled, G., Mathé, J., Biance, A. L., Bacri, L., Betton, J. M., Lairez, D., Pelta, J., and Auvray, L.** (**2007**). "Unfolding of Proteins and Long Transient Conformations Detected by Single Nanopore Recording." *Physical Review Letters*, 98(15): 158 101.

[85] **Pedone, D.** (**2011**). *Nanopore analytics - Electro-optical studies on single molecules*. Ph.D. thesis, Technische Universität München.

[86] **Pedone, D., Firnkes, M., and Rant, U.** (**2009**). "Data Analysis of Translocation Events in Nanopore Experiments." *Analytical Chemistry*, 81(23): 9689–9694.

[87] **Pedone, D., Langecker, M., Abstreiter, G., and Rant, U.** (**2011**). "A Pore–Cavity–Pore Device to Trap and Investigate Single Nanoparticles and DNA Molecules in a Femtoliter Compartment: Confined Diffusion and Narrow Escape." *Nano Letters*, 11(4): 1561–1567.

[88] **Pralle, A., Florin, E. L., Stelzer, E. H. K., and Hörber, J. K. H.** (**1998**). "Local viscosity probed by photonic force microscopy." *Applied Physics A: Materials Science & Processing*, 66: 71–73.

[89] **Princiotta, M. F., Finzi, D., Qian, S.-B., Gibbs, J., Schuchmann, S., Buttgereit, F., Bennink, J. R., and Yewdell, J. W.** (**2003**). "Quantitating Protein Synthesis, Degradation, and Endogenous Antigen Processing." *Immunity*, 18(3): 343–354.

[90] **Radu, I. S. and et al.** (**2010**). "Evidence that small proteins translocate through silicon nitride pores in a folded conformation." *Journal of Physics: Condensed Matter*, 22(45): 454 133.

[91] **Rhee, M. and Burns, M.** (**2007**). "Nanopore sequencing technology: nanopore preparations." *Trends in Biotechnology*, 25(4): 174–181.

[92] **Rice, C. L. and Whitehead, R.** (**1965**). "Electrokinetic Flow in a Narrow Cylindrical Capillary." *The Journal of Physical Chemistry*, 69(11): 4017–4024.

[93] **Sakmann, B. and Neher, E.** (**1995**). *Single-Channel Recording*. Plenum Press, New York, second edition edition.

[94] **Schneider, G. F., Kowalczyk, S. W., Calado, V. E., Pandraud, G., Zandbergen, H. W., Vandersypen, L. M. K., and Dekker, C.** (**2010**). "DNA Translocation through Graphene Nanopores." *Nano Letters*, 10(8): 3163–3167.

[95] **Schoch, R. B., Han, J., and Renaud, P.** (**2008**). "Transport phenomena in nanofluidics." *Reviews of Modern Physics*, 80(3): 839–883.

[96] **Seemueller, E., Lupas, A., Stock, D., Lowe, J., Huber, R., and Baumeister, W.** (**1995**). "Proteasome from Thermoplasma acidophilum: a threonine protease." *Science*, 268(5210): 579–582.

[97] **Seemueller, E., Lupas, A., Zuehl, F., Zwickl, P., and Baumeister, W.** (**1995**). "The proteasome from Thermoplasma acidophilum is neither a cysteine nor a serine protease." *FEBS Letters*, 359(2-3): 173–178.

[98] **Seidel, H., Csepregi, L., Heuberger, A., and Baumgartel, H.** (**1990**). "Anisotropic Etching of Crystalline Silicon in Alkaline Solutions." *Journal of The Electrochemical Society*, 137(11): 3612–3626.

[99] **Sexton, L. T., Horne, L. P., Sherrill, S. A., Bishop, G. W., Baker, L. A., and Martin, C. R.** (**2007**). "Resistive-pulse studies of proteins and protein/antibody complexes using a conical nanotube sensor." *J. Am. Chem. Soc*, 129(43): 13 144–13 152.

[100] **Sexton, L. T., Mukaibo, H., Katira, P., Hess, H., Sherrill, S. A., Horne, L. P., and Martin, C. R.** (**2010**). "An Adsorption-Based Model for Pulse Duration in Resistive-Pulse Protein Sensing." *Journal of the American Chemical Society*, 132(19): 6755–6763.

[101] **Siwy, Z., Apel, P., Baur, D., Dobrev, D. D., Korchev, Y. E., Neumann, R., Spohr, R., Trautmann, C., and Voss, K.-O.** (**2003**). "Preparation of synthetic nanopores with transport properties analogous to biological channels." *Surface Science*, 532-535(0): 1061–1066.

[102] **Siwy, Z., Trofin, L., Kohli, P., Baker, L. A., Trautmann, C., and Martin, C. R.** (**2005**). "Protein Biosensors Based on Biofunctionalized Conical Gold Nanotubes." *Journal of the American Chemical Society*, 127(14): 5000–5001.

[103] **Smeets, R. M. M., Keyser, U. F., Dekker, N. H., and Dekker, C.** (**2008**). "Noise in solid-state nanopores." *Proceedings of the National Academy of Sciences*, 105(2): 417.

[104] **Smeets, R. M. M., Keyser, U. F., Wu, M. Y., Dekker, N. H., and Dekker, C.** (**2006**). "Nanobubbles in Solid-State Nanopores." *Phys. Rev. Lett.*, 97(8): 088 101–4.

[105] **Smolyanitsky, A. and Saraniti, M.** (**2009**). "Silicon nanopores as bioelectronic devices: a simulation study." *Journal of Computational Electronics*, 8(2): 90–97.

[106] **Squires, T. M. and Quake, S. R.** (**2005**). "Microfluidics: Fluid physics at the nanoliter scale." *Reviews of Modern Physics*, 77(3): 977–1026.

[107] **Stein, R. L., Melandri, F., and Dick, L.** (**1996**). "Kinetic Characterization of the Chymotryptic Activity of the 20S Proteasome." *Biochemistry*, 35(13): 3899–3908.

[108] **Storm, A. J., Chen, J. H., Ling, X. S., Zandbergen, H. W., and Dekker, C.** (**2003**). "Fabrication of solid-state nanopores with single-nanometre precision." *Nature Materials*, 2(8): 537–540.

[109] **Strunz, T., Oroszlan, K., Schumakovitch, I., Güntherodt, H. J., and Hegner, M.** (**2000**). "Model Energy Landscapes and the Force-Induced Dissociation of Ligand-Receptor Bonds." *Biophysical Journal*, 79(3): 1206–1212.

[110] **Tabard-Cossa, V., Trivedi, D., Wiggin, M., Jetha, N., Nahid, and Marziali, A.** (**2007**). "Noise analysis and reduction in solid-state nanopores." *NANOTECHNOLOGY*, 18(30): 305 505.

[111] **Talaga, D. S. and Li, J.** (**2009**). "Single-Molecule Protein Unfolding in Solid State Nanopores." *J. Am. Chem. Soc*, 131(26): 9287–9297.

[112] **Tangsuphoom, T. N. and Coupland, J. N.** (**2008**). "Effect of pH and Ionic Strength on the Physicochemical Properties of Coconut Milk Emulsions." *Journal of Food Science*, 73(6): E274–E280.

[113] **Thess, A., Hutschenreiter, S., Hofmann, M., Tampé, R., Baumeister, W., and Guckenberger, R.** (**2002**). "Specific Orientation and Two-dimensional Crystallization of the Proteasome at Metal-chelating Lipid Interfaces." *Journal of Biological Chemistry*, 277(39): 36 321–36 328.

[114] **Uram, J., Ke, K., and Mayer, M.** (**2008**). "Noise and Bandwidth of Current Recordings from Submicrometer Pores and Nanopores." *ACS Nano*, 2(5): 857–872.

[115] **van der Heyden, F. H. J., Stein, D., and Dekker, C.** (**2005**). "Streaming Currents in a Single Nanofluidic Channel." *Physical Review Letters*, 95(11): 116 104.

[116] **van Dorp, S., Keyser, U. F., Dekker, N. H., Dekker, C., and Lemay, S. G.** (**2009**). "Origin of the electrophoretic force on DNA in solid-state nanopores." *Nat Phys*, 5(5): 347–351.

[117] **Verveen, A. A. and DeFelice, L. J.** (**1974**). "Membrane noise." *Progress in Biophysics and Molecular Biology*, 28.

[118] **Vlassiouk, I., Kozel, T. R., and Siwy, Z. S.** (**2009**). "Biosensing with Nanofluidic Diodes." *Journal of the American Chemical Society*, 131(23): 8211–8220.

[119] **Vlassiouk, I., Smirnov, S., and Siwy, Z.** (**2008**). "Ionic selectivity of single nanochannels." *Nano Letters*, 8(7): 1978.

[120] **Wang, H., Laws, G. M., Milicic, S., Boland, P., Handugan, A., Pratt, M., Eschrich, T., Myhajlenko, S., Allgair, J. A., and Bunday, B.** (**2007**). "Low temperature ZEP-520A development process for enhanced critical dimension realization in reactive ion etch etched polysilicon." *Journal of Vacuum Science & Technology B: Microelectronics and Nanometer Structures*, 25(1): 102–105.

[121] **Wanunu, M. and Meller, A.** (**2007**). "Chemically modified solid-state nanopores." *Nano Letters*, 7(6): 1580–1585.

[122] **Wanunu, M., Morrison, W., Rabin, Y., Grosberg, A. Y., and Meller, A.** (**2009**). "Electrostatic focusing of unlabelled DNA into nanoscale pores using a salt gradient." *Nat Nano*, 5(2): 160–165.

[123] **Warszynski, P.** (**2000**). "Coupling of hydrodynamic and electric interactions in adsorption of colloidal particles." *Advances in Colloid and Interface Science*, 84(1-3): 47–142.

[124] **Wei, R., Gatterdam, V., Wieneke, R., Tampé, R., and Rant, U.** (**2012**). "Stochastic sensing of proteins with receptor-modified solid-state nanopores." *Nat Nano*, 7(4): 257–263.

[125] **Wei, R., Martin, T. G., Rant, U., and Dietz, H.** (**2012**). "DNA Origami Gatekeepers for Solid-State Nanopores." *Angewandte Chemie International Edition*, pages n/a–n/a.

[126] **Wei, R., Pedone, D., Zürner, A., Döblinger, M., and Rant, U.** (**2010**). "Fabrication of Metallized Nanopores in Silicon Nitride Membranes for Single-Molecule Sensing." *Small*, 6(13): 1406–1414.

[127] **Wenzel, T., Eckerskorn, C., Lottspeich, F., and Baumeister, W.** (**1994**). "Existence of a molecular ruler in proteasomes suggested by analysis of degradation products." *FEBS Letters*, 349(2): 205–209.

[128] **Werner, C., Körber, H., Zimmermann, R., Dukhin, S., and Jacobasch, H.-J.** (**1998**). "Extended Electrokinetic Characterization of Flat Solid Surfaces." *Journal of Colloid and Interface Science*, 208(1): 329–346.

[129] **Wong, C. T. A. and Muthukumar, M.** (**2007**). "Polymer capture by electro-osmotic flow of oppositely charged nanopores." *The Journal of Chemical Physics*, 126(16): 164 903–6.

[130] **Wu, M. Y., Krapf, D., Zandbergen, M., Zandbergen, H., and Batson, P. E.** (**2005**). "Formation of nanopores in a SiN/ SiO membrane with an electron beam." *Applied Physics Letters*, 87: 113 106.

[131] **Xie, P., Xiong, Q., Fang, Y., Qing, Q., and Lieber, C. M.** (**2012**). "Local electrical potential detection of DNA by nanowire-nanopore sensors." *Nat Nano*, 7(2): 119–125.

[132] **Yusko, E. C., An, R., and Mayer, M.** (**2010**). "Electroosmotic Flow Can Generate Ion Current Rectification in Nano- and Micropores." *ACS Nano*, 4(1): 477–487.

[133] **Yusko, E. C., Johnson, J. M., Majd, S., Prangkio, P., Rollings, R. C., Li, J., Yang, J., and Mayer, M.** (**2011**). "Controlling protein translocation through nanopores with bio-inspired fluid walls." *Nat Nano*, 6(4): 253–260.

[134] **Zhang, W. M., Li, J., Cao, L. X., Wang, Y. G., Guo, W., Liu, K. X., and Xue, J. M.** (**2008**). "Fabrication of nanoporous silicon dioxide/silicon nitride membranes using etched ion track technique." *Nuclear Instruments and Methods in Physics Research Section B: Beam Interactions with Materials and Atoms*, 266(12-13): 3166–3169.

[135] **Zimmermann, R. M. and Cox, E. C.** (**1994**). "DNA stretching on functionalized gold surfaces." *Nucleic Acids Research*, 22(3): 492–497.

[136] **Zwickl, P., Grziwa, A., Puehler, G., Dahlmann, B., Lottspeich, F., and Baumeister, W.** (**1992**). "Primary structure of the Thermoplasma proteasome and its implications for the structure, function, and evolution of the multicatalytic proteinase." *Biochemistry*, 31(4): 964–972.

[137] **Zwickl, P., Ng, D., Woo, K. M., Klenk, H.-P., and Goldberg, A. L.** (**1999**). "An Archaebacterial ATPase, Homologous to ATPases in the Eukaryotic 26S Proteasome, Activates Protein Breakdown by 20S Proteasomes." *Journal of Biological Chemistry*, 274(37): 26 008–26 014.

Acknowledgements

Finally I would like to thank all members of the Schottky Institut, for a great time and a cooperative working atmosphere. Many people helped me with a lot of things. Especially, I would like to thank:

Prof. Dr. Gerhard Abstreiter
For an excellent scientific infrastructure and the opportunity to use it in an uncomplicated way. For me the Schottky Institute and its working atmosphere is one of the best research facilities I can think of.

Dr. Ulrich Rant
For his support, confidence and the opportunity to work in his group. His motivation and positive attitude in all discussions were very important and inspiring for me.

Dr. Daniel Pedone
For being an example and motivator for my scientific work, for conversations and support not only in science but also during my transition to industry, and for lots of suggestions for improvement of this thesis.

Shan, Martin and Alexandra
My co-workers and fellow sufferers in the nanopore group for many discussions and help whenever necessary. For proofreading, for programming an excellent Labview measurement program and just for good company on conferences and in the lab. I wish you all the best for the future!

Makiko, Paul and Thomas
My office mates, for giving me a good time with a lot of fun and help, not only in the container office, but also in the lab. Dry ice rocks!

Jelena, Simone, Vale, Vera, Alex, Andi, Christian, Frank, Markus, Ralf, Sachsi, Wolfi
The other members of the biogroup, who helped me with a lot of things, too many to mention them all; and for good stories and conversations during the coffee break and in the lab.

Anna Cattani-Scholz
For her support and all chemical discussions.

Markus Döblinger, LMU München, Chemistry Department
For fabricating nanopores and 'pit-pore' structures with a TEM.

Christian Grunwald, Alexander Kleefen and Prof. Dr. Robert Tampé, Institute of Biochemistry, Goethe-Universität Frankfurt a.M.
For providing proteasome molecules, help with the handling and other biology related questions.

Tobias Gründl and all other E26 members
For repairing the geriatric PECVD and helping me with the cleanroom equipment.

Peter Weiser
For help and maintainance of the e-beam lithography system.

Claudia Paulus
For lithography masks and for managing UT and keeping it in excellent condition.

Fritz Sedlmeir, Ade Ziegltrum
For building my numerous measurement cells and help in the workshop.

Irmgard Neuner
For help with all administrative issues.

Prof. Vogl and the Admin-group
For maintaining a reliable and stable Windows network.

Marianne Hanzlik, Andreas Kastenmüller
For help and the opportunity to use the TEM in the TUM chemistry department.

Thomas Martin, Prof. Hendrik Dietz
For help and the opportunity to use the TEM in the ZNN.

The TUM **Institute for Advanced Study** for funding my position.

The **International Graduate School of Science and Engineering** for managing the graduate program and for unforgetable parties in Raitenhaslach.

My parents and my family
For their tremendous support and belief in me. It is great to know that you are always there for me and that I can rely on you.

Angelika
How lucky I am that I have met you! Without your presence in my life, this work would be nothing to me. Thank you for your support beyond university and for the great time we spent together, which gave me the endurance to finish this work.

In der Schriftenreihe des Walter Schottky Instituts der Technischen Universität München sind bisher folgende Bände erschienen:

Vol. 1
Cornelia Engel
Si/SiGe basierende Phototransistoren
131 Seiten
ISBN 3-932749-01-4

Vol. 2
Peter Schittenhelm
Selbst-Organisation und Selbst-Ordnung in Si/SiGe-Heterostrukturen
151 Seiten
ISBN 3-932749-02-2

Vol. 3
Andreas Nutsch
Selektive Epitaxie von (GaIn)(AsP) Schichtstrukturen
129 Seiten
ISBN 3-932749-03-0

Vol. 4
Peter Baumgartner
Optische und elektronische Eigenschaften lasergeschriebener GaAs-Nanostrukturen
180 Seiten
ISBN 3-932749-04-9

Vol. 5
Walter Franz Rieger
Untersuchung der elektronischen und strukturellen Eigenschaften von GaNAlN und deren Legierungen
158 Seiten
ISBN 3-932749-05-7

Vol. 6
Markus Hauser
Oberflächenemittierende Laserdioden mit Mehrfachepitaxie
148 Seiten
ISBN 3-932749-06-5

Vol. 7
Markus Sexl
Verspannte und gitterrelaxierte In(GaAl)As Heterostrukturen
144 Seiten
ISBN 3-932749-07-3

Vol. 8
Christian Obermüller
Photolumineszenszspektroskopie mit optischen Nahfeldmethoden an GaAs-Nanostrukturen
140 Seiten
ISBN 3-932749-08-1

Vol. 9
Edilson Silveira
Inelastische Lichtstreuung an niedrig-dimensionalen Halbleiterstrukturen
104 Seiten
ISBN 3-932749-09-X

Vol. 10
Eberhard Christian Rohrer
Photoleitungs-Spektroskopie von Diamant
153 Seiten
ISBN 3-932749-10-03

Vol. 11
Thomas Wimbauer
Magnetische Resonanz-Untersuchungen an modernen Halbleitermaterialien
125 Seiten
ISBN 3-932749-11-1

Vol. 12
Herbert Verhoeven
Thermische Eigenschaften von CVD-Diamantschichten
154 Seiten
ISBN 3-932749-12-X

Vol. 13
Hans-Christoph Ostendorf
Trennung von Volumen- und Oberflächenrekombination in Silizium
128 Seiten
ISBN 3-932749-13-8

Vol. 14
Martin Städele
Dichtefunktionaltheorie mit exaktem Austausch für Halbleiter
202 Seiten
ISBN 3-932749-14-6

Vol. 15
Helmut Angerer
Herstellung von Gruppe III-Nitriden mit Molekularstrahlepitaxie
144 Seiten
ISBN 3-932749-15-4

Vol. 16
Wolfgang Heller
Spektroskopie einzelner Quantenpunkte in magnetischen und elektrischen Feldern
128 Seiten
ISBN 3-932749-16-2

Vol. 17
Molela Moukara
Pseudopotentiale mit exaktem Austausch
117 Seiten
ISBN 3-932749-17-0

Vol. 18
Ralph Oberhuber
Elektronische Struktur und Transport in verspannten Halbleiterschichtsystemen
110 Seiten
ISBN 3-932749-18-9

Vol. 19
Reiner Pech
High-Energy Boron-Implantation into Different Silicon Substrates
158 Seiten
ISBN 3-932749-19-7

Vol. 20
Christoph Martin Engelhardt
Zyklotronresonanz zweidimensionaler Ladungsträgersysteme in Halbleitern, Effekte der Elektron-Elektron-Wechselwirkung und Lokalisierung
317 Seiten
ISBN 3-932749-20-0

Vol. 21
Eduard Neufeld
Erbium-dotierte Si/SiGe-Lichtemitter und -Wellenleiter
136 Seiten
ISBN 3-932749-21-9

Vol. 22
Gert Schedelbeck
Optische Eigenschaften von Halbleiternanostrukturen hergestellt durch Überwachsen von Spaltflächen
154 Seiten
ISBN 3-932749-22-7

Vol. 23
Jürgen Zimmer
Optoelektronisches Verhalten von Dünnschichtbauelementen aus amorphem und mikrokristallinem Silizium
171 Seiten
ISBN 3-932749-23-5

Vol. 24
Berthold Schmidt
Leistungsoptimierung abstimmbarer InGaAsP/InP Halbleiterlaser
85 Seiten
ISBN 3-932749-24-3

Vol. 25
Jianhong Zhu
Ordering of self-assembled Ge and SiGe nanostructures on vicinal Si surfaces
120 Seiten
ISBN 3-932749-25-1

Vol. 26
Gerhard Groos
Herstellung und Charakterisierung von Silizium-Nanostrukturen
168 Seiten
ISBN 3-932749-26-X

Vol. 27
Uwe Hansen
Theorie der Reaktionskinetik an Festkörperoberflächen
119 Seiten
ISBN 3-932749-27-8

Vol. 28
Roman Dimitrov
Herstellung und Charakterisierung von AlGaN/GaN-Transistoren
196 Seiten
ISBN 3-932749-28-6

Vol. 29
Martin Eickhoff
Piezowiderstandsmechanismen in Halbleitern mit großer Bandlücke
151 Seiten
ISBN 3-932749-29-4

Vol. 30
Nikolai Wieser
Ramanspektroskopie an Gruppe III-Nitriden
161 Seiten
ISBN 3-932749-30-8

Vol. 31
Rainer Janssen
Strukturelle und elektronische Eigenschaften amorpher Silizium-Suboxide
275 Seiten
ISBN 3-932749-31-6

Vol. 32
Martin W. Bayerl
Magnetic resonance investigations of group III-nitrides
155 Seiten
ISBN 3-932749-32-4

Vol. 33
Martin Rother
Elektronische Eigenschaften von Halbleiternanostrukturen hergestellt durch Überwachsen von Spaltflächen
196 Seiten
ISBN 3-932749-33-2

Vol. 34
Frank Findeis
Optical spectroscopy on single self-assembled quantum dots
156 Seiten
ISBN 3-932749-34-0

Vol. 35
Markus Ortsiefer
Langwellige Vertikalresonator-Laser-dioden im Materialsystem InGaAlAs/InP
152 Seiten
ISBN 3-932749-35-9

Vol. 36
Roland Zeisel
Optoelectronic properties of defects in diamond and AlGaN alloys
140 Seiten
ISBN 3-932749-36-7

Vol. 37
Liwen Chu
Inter- und Intraband Spektroskopie an selbstorganisierten In(Ga)As/GaAs Quantenpunkten
124 Seiten
ISBN 3-932749-37-5

Vol. 38
Christian Alexander Miesner
Intra-Valenzbandspektroskopie an SiGe-Nanostrukturen in Si
100 Seiten
ISBN 3-932749-38-3

Vol. 39
Szabolcs Kátai
Investigation of the nucleation process of chemical vapour deposited diamond films
178 Seiten
ISBN 3-932749-39-1

Vol. 40
Markus Arzberger
Wachstum, Eigenschaften und Anwendungen selbstorganisierter InAs-Quantenpunkte
236 Seiten
ISBN 3-932749-40-5

Vol. 41
Markus Oliver Markmann
Optische Eigenschaften von Erbium in $Si/Si_{1-x}C_x$, $Si/Si_{1-x}Ge_x$ und Si/SiO_x Heterostrukturen
182 Seiten
ISBN 3-932749-41-3

Vol. 42
Rainer Alexander Deutschmann
Two dimensional electron systems in atomically precise periodic potential
210 Seiten
ISBN 3-932749-42-1

Vol. 43
Uwe Karrer
Schottky-Dioden auf Galliumnitrid: Eigenschaften und Anwendungen in der Sensorik
182 Seiten
ISBN 3-932749-43-X

Vol. 44
Günther Anton Johann Vogg
Epitaxial thin films of Si and Ge based Zintl phases and sheet polymers
169 Seiten
ISBN 3-932749-44-8

Vol. 45
Christian Strahberger
Vertikaler Transport und extreme Magnetfelder in Halbleitern
167 Seiten
ISBN 3-932749-45-6

Vol. 46
Jan Schalwig
Feldeffekt-Gassensoren und ihre Anwendung in Abgasnachbehandlungssystemen
125 Seiten
ISBN 3-932749-46-4

Vol. 47
Christopher Eisele
Novel absorber structures for Si-based thin film solar cells
126 Seiten
ISBN 3-932749-47-2

Vol. 48
Stefan Hackenbuchner
Elektronische Struktur von Halbleiter-Nanobauelementen im thermodynamischen Nichtgleichgewicht
213 Seiten
ISBN 3-932749-48-0

Vol. 49
Andreas Sticht
Herstellung und Charakterisierung von dünnen Silizium/Siliziumoxid-Schichtsystemen
166 Seiten
ISBN 3-932749-49-9

Vol. 50
Giuseppe Scarpa
Design and fabrication of Quantum Cascade Lasers
193 Seiten
ISBN 3-932749-50-2

Vol. 51
Jörg Frankenberger
Optische Untersuchungen an zweidimensionalen Ladungsträgersystemen
158 Seiten
ISBN 3-932749-51-0

Vol. 52
Doris Heinrich
Wavelength selective optically induced charge storage in self-assembled semiconductor quantum dots
144 Seiten
ISBN 3-932749-52-9

Vol. 53
Nicolaus Ulbrich
Entwurf und Charakterisierung von Quanten-Kaskadenlasern und Quantenpunktkaskaden
133 Seiten
ISBN 3-932749-53-7

Vol. 54
Lutz Carsten Görgens
Analyse stickstoffhaltiger III-V Halbleiter-Heterosysteme mit hochenergetischen schweren Ionen
116 Seiten
ISBN 3-932749-54-5

Vol. 55
Andreas Janotta
Doping, light-induced modification and biocompatibility of amorphous silicon suboxides
180 Seiten
ISBN 3-932749-55-3

Vol. 56
Sebastian Tobias Benedikt Gönnenwein
Two-dimensional electron gases and ferromagnetic semiconductors: materials for spintronics
198 Seiten
ISBN 3-932749-56-1

Vol. 57
Evelin Beham
Photostromspektroskopie an einzelnen Quantenpunkten
186 Seiten
ISBN 3-932749-57-X

Vol. 58
Po-Wen Chiu
Towards carbon nanotube-based molecular electronics
116 Seiten
ISBN 3-932749-58-8

Vol. 59
Tobias Graf
Spin-spin interactions of localized electronic states in semiconductors
194 Seiten
ISBN 3-932749-59-6

Vol. 60
Stefan Klein
Microcrystalline silicon prepared by hot wire CVD: preparation and characterisation of material and solar cells
157 Seiten
ISBN 3-932749-60-X

Vol. 61
Markus Krach
Frequenzverdreifacher mit Anti-Seriellem Schottky-Varaktor für den Terahertzbereich
156 Seiten
ISBN 3-932749-61-8

Vol. 62
Ralph Thomas Neuberger
AlGaN/GaN-Heterostrukturen als chemische Sensoren in korrosiven Medien
153 Seiten
ISBN 3-932749-62-6

Vol. 63
Sonia Perna
Wasserstoff-Passivierung von trikristallinem Silizium durch hydrogenisiertes Siliziumnitrid
136 Seiten
ISBN 3-932749-63-4

Vol. 64
Oliver Schumann
Einfluss von Stickstoff auf das Wachstum und die Eigenschaften von InAs-Quantenpunkten
148 Seiten
ISBN 3-932749-64-2

Vol. 65
Gerhard Rösel
Entwicklung und Charakterisierung von Typ-II-Heterostrukturen für die Abstimmregion in abstimmbaren Laserdioden
101 Seiten
ISBN 3-932749-65-0

Vol. 66
Angela Link
Zweidimensionale Elektronen- und Löcher-Gase in GaN/AlGaN Heterostrukturen
156 Seiten
ISBN 3-932749-66-9

Vol. 67
Matthias Sabathil
Opto-electronic and quantum transport properties of semiconductor nanostructures
156 Seiten
ISBN 3-932749-67-7

Vol. 68
Frank Fischer
Growth and electronic properties of two-dimensional systems on (110) oriented GaAs
139 Seiten
ISBN 3-932749-68-5

Vol. 69
Robert Shau
Langwellige oberflächenemittierende Laserdioden mit hoher Ausgangsleistung und Modulationsbandbreite
198 Seiten
ISBN 3-932749-69-3

Vol. 70
Andrea Baumer
Structural and electronic properties of hydrosilylated silicon surfaces
163 Seiten
ISBN 3-932749-70-7

Vol. 71
Andreas Florian Kreß
Manipulation of the Light-Matter-Interaction in Photonic Crystal Nanocavities
185 Seiten
ISBN 3-932749-71-5

Vol. 72
Markus Grau
Molekularstrahlepitaktische Herstellung von antimonidischen Laserdioden für die Gassensorik
138 Seiten
ISBN 3-932749-72-3

Vol. 73
Karin Buchholz
Microprocessing of silicon on insulator substrates and biofunctionalisation of silicon dioxide surfaces for sensing applications in fluids
170 Seiten
ISBN 3-932749-73-1

Vol. 74
Dominique Bougeard
Spektroskopische Charakterisierung von Germanium-Quantenpunkten in Silizium
154 Seiten
ISBN 3-932749-74-X

Vol. 75
Jochen Bauer
Untersuchungen zum kontrollierten Wachstum von InAs-Nanostrukturen auf Spaltflächen
140 Seiten
ISBN 3-932749-75-8

Vol. 76
Ingo Bormann
Intersubband Spektroskopie an Silizium-Germanium Quantenkaskadenstrukturen
124 Seiten
ISBN 3-932749-76-6

Vol. 77
Hubert Johannes Krenner
Coherent quantum coupling of excitons in single quantum dots and quantum dot molecules
160 Seiten
ISBN 3-932749-77-4

Vol. 78
Ulrich Rant
Electrical manipulation of DNA-layers on gold surfaces
249 Seiten
ISBN 3-932749-78-2

Vol. 79
René Todt
Widely tunable laser diodes with distributed feedback
152 Seiten
ISBN 3-932749-79-0

Vol. 80
Miroslav Kroutvar
Charge and spin storage in quantum dots
150 Seiten
ISBN 3-932749-80-4

Vol. 81
Markus Maute
Mikromechanisch abstimmbare Laser-Dioden mit Vertikalresonator
170 Seiten
ISBN 3-932749-81-2

Vol. 82
Frank Ertl
Anisotrope Quanten-Hall-Systeme, Vertikale Ultrakurzkanal- und Tunneltransistoren
170 Seiten
ISBN 3-932749-82-0

Vol. 83
Sebastian M. Luber
III-V semiconductor structures for biosensor and molecular electronics applications
212 Seiten
ISBN 978-3-932749-83-4

Vol. 84
Claudio Ronald Miskys
New substrates for epitaxy of group III nitride semiconductors: challenges and potential
207 Seiten
ISBN 978-3-932749-84-1

Vol. 85
Sebastian Friedrich Roth
n- and p-type transport in (110) GaAs substrates, single- and double-cleave structures
138 Seiten
ISBN 978-3-932749-85-8

Vol. 86
Mario Gjukic
Metal-induced crystallization of silicon-germanium alloys
309 Seiten
ISBN 978-3-932749-86-5

Vol. 87
Tobias Zibold
Semiconductor based quantum information devices: Theory and simulations
151 Seiten
ISBN 978-3-932749-87-2

Vol. 88
Thomas Jacke
Weit abstimmbare Laserdiode mit vertikal integriertem Mach-Zehnder-Interferometer
165 Seiten
ISBN 978-3-932749-88-9

Vol. 89
Nenad Ocelić
Quantitative near-field phonon-polariton spectroscopy
174 Seiten
ISBN 978-3-932749-89-6

Vol. 90
Kenji Arinaga
Control and manipulation of DNA on gold and its application for biosensing
111 Seiten
ISBN 978-3-932749-90-2

Vol. 91
Hans-Gregor Hübl
Coherent manipulation and electrical detection of phosphorus donor spins in silicon
162 Seiten
ISBN 978-3-932749-91-9

Vol. 92
Andrea Friedrich
Quanten-Kaskaden-Laser ohne Injektorbereiche
140 Seiten
ISBN 978-3-932749-92-6

Vol. 93
Oliver Dier
Das Materialsystem (AlGaIn) (AsSb): Eigenschaften und Eignung für GaSb-basierte Vertikalresonator-Laserdioden
174 Seiten
ISBN 978-3-932749-93-3

Vol. 94
Georg Steinhoff
Group III-nitrides for bio- and electrochemical sensors
197 Seiten
ISBN 978-3-932749-94-0

Vol. 95
Stefan Harrer
Next-generation nanoimprint lithography: Innovative approaches towards improving flexibility and resolution of nanofabrication in the sub-15-nm region
161 Seiten
ISBN 978-3-932749-95-7

Vol. 96
Stefan Ahlers
Magnetic and electrical properties of epitaxial GeMn
184 Seiten
ISBN 978-3-932749-96-0

Vol. 97
Emanuele Uccelli
Guided self-assembly of InAs quantum dots arrays on (110) surfaces
172 Seiten
ISBN 978-3-932749-97-1

Vol. 98
Shavaji Dasgupta
Growth optimization and characterization of high mobility two-dimensional electron systems in AlAs quantum wells
152 Seiten
ISBN 978-3-932749-98-8

Vol. 99
Werner Hofmann
InP-based long-wavelength VCSELs and VCSEL arrays for high-speed optical communication
142 Seiten
ISBN 978-3-932749-99-5

Vol. 100
Robert Lechner
Silicon nanocrystal films for electronic applications
227 Seiten
ISBN 978-3-941650-00-8

Vol. 101
Nebile Işık
Investigation of Landau level spin reversal in (110) oriented p-type GaAs quantum wells
114 Seiten
ISBN 978-3-941650-01-5

Vol. 102
Andreas Florian Härtl
Novel concepts for biosensors using diamond-based field effect transistors
255 Seiten
ISBN 978-3-941650-02-2

Vol. 103
Felix Florian Georg Hofbauer
Realization of electrically tunable single quantum dot nanocavities
160 Seiten
ISBN 978-3-941650-03-9

Vol. 104
Dominic F. Dorfner
Novel photonic biosensing based on silicon nanostructures
169 Seiten
ISBN 978-3-941650-04-6

Vol. 105
Till Andlauer
Optoelectronic and spin-related properties of semiconductor nanostructures in magnetic fields
157 Seiten
ISBN 978-3-941650-05-3

Vol. 106
Christoph Bihler
Magnetic semiconductors
190 Seiten
ISBN 978-3-941650-06-0

Vol. 107
Michael Huber
Tunnel-Spektroskopie im Quanten-Hall-Regime
164 Seiten
ISBN 978-3-941650-07-7

Vol. 108
Philipp Achatz
Metal-insulator transition and super-Conductivity in heavily boron-doped diamond and related materials
151 Seiten
ISBN 978-3-941650-08-4

Vol. 109
Sebastian Strobel
Nanoscale contacts to organic molecules based on layered semiconductor substrates
140 Seiten
ISBN 978-3-941650-09-1

Vol. 110
Ying Xiang
Semiconductor nanowires and templates for electronic applications
152 Seiten
ISBN 978-3-941650-10-7

Vol. 111
Michael Kaniber
Non-classical light generation in photonic crystal nanostructures
177 Seiten
ISBN 978-3-941650-11-4

Vol. 112
Martin Hermann
Epitaktische AlN-Schichten auf Saphir und Diamant
216 Seiten
ISBN 978-3-941650-12-1

Vol. 113
Dominik Heiss
Spin storage in quantum dot ensembles and single quantum dots
196 Seiten
ISBN 978-3-941650-13-8

Vol. 114
Tillmann Christoph Kubis
Quantum transport in semiconductor nanostructures
253 Seiten
ISBN 978-3-941650-14-5

Vol. 115
Lucia Steinke
Magnetotransport of coupled quantum Hall edges in a bent quantum well
194 Seiten
ISBN 978-3-941650-15-2

Vol. 116
Christian Lauer
Antimonid-basierte Vertikalresonator-Laserdioden für Wellenlängen oberhalb 2 μm
180 Seiten
ISBN 978-3-941650-16-9

Vol. 117
Simone Maria Kaniber
Optoelektronische Phänomene in hybriden Schaltkreisen aus Kohlenstoffnanoröhren und dem Photosystem I
136 Seiten
ISBN 978-3-941650-17-6

Vol. 118
Martin Heiß
Growth and properties of low-dimensional III-V semiconductor nanowire heterostructures
172 Seiten
ISBN 978-3-941650-18-3

Vol. 119
Sandro Francesco Tedde
Design, fabrication and characterization of organic photodiodes for industrial and medical applications
277 Seiten
ISBN 978-3-941650-19-0

Vol. 120
Danche Spirkoska Jovanov
Fundamental properties of self-catalyzed GaAs nanowires and related heterostructures
200 Seiten
ISBN 978-3-941650-20-6

Vol. 121
Jürgen Sailer
Materials and devices for quantum Information processing in Si/SiGe
158 Seiten
ISBN 978-3-941650-21-3

Vol. 122
Ilaria Zardo
Growth and raman spectroscopy studies of gold-free catalyzed semiconductor nanowires
184 Seiten
ISBN 978-3-941650-22-0

Vol. 123
Andre Rainer Stegner
Shallow dopants in nanostructured and in isotopically engineered silicon
185 Seiten
ISBN 978-3-941650-23-7

Vol. 124
Andreas J. Huber
Nanoscale surface-polariton spectroscopy by mid- and far-infrared near-field microscopy
144 Seiten
ISBN 978-3-941650-24-4

Vol. 125
Marco Andreas Höb
Funktionalisierung von Gruppe IV-Halbleitern
186 Seiten
ISBN 978-3-941650-25-1

Vol. 126
Daniel Claudio Pedone
Nanopore analytics – electro-optical studies on single molecules
114 Seiten
ISBN 978-3-941650-26-8

Vol. 127
Casimir Richard Simeon Katz
Multi-alloy structures for injectorless Quantum Cascade Lasers
131 Seiten
ISBN 978-3-941650-27-5

Vol. 128
Barbara Annemarie Kathrin Baur
Functionalization of group III-nitrides for biosensor applications
215 Seiten
ISBN 978-3-941650-28-2

Vol. 129
Arne Laucht
Semiconductor quantum optics with tailored photonic nanostructures
232 Seiten
ISBN 978-3-941650-29-9

Vol. 130
Jia Chen
Compact laser-spectroscopic gas sensors using Vertical-Cavity Surface-Emitting Lasers
150 Seiten
ISBN 978-3-941650-30-5

Vol. 131
Hans Leonhard Prechtel
Ultrafast Photocurrents and Terahertz Radiation in Gallium Arsenide and Carbon Based Nanostructures
160 Seiten
ISBN 978-3-941650-31-2

Vol. 132
Roland Enzmann
Technologieentwicklung für eine Einzelphotonenquelle
142 Seiten
ISBN 978-3-941650-32-9

Vol. 133
Alexander Bachmann
Antimonide-Based Vertical-Cavity Surface-Emitting Lasers
144 Seiten
ISBN 978-3-941650-33-6

Vol. 134
Markus Andreas Mangold
Two-Dimensional Gold Nanoparticle Arrays – A Platform for Molecular Optoelectronics
140 Seiten
ISBN 978-3-941650-34-3

Vol. 135
Stefan Birner
Modeling of semiconductor nanostructures and semiconductor–electrolyte interfaces
227 Seiten
ISBN 978-3-941650-35-0

Vol. 136
Christian Claus Jäger
Polycrystalline Silicon Thin Films for Electronic Applications
202 Seiten
ISBN 978-3-941650-36-7

Vol. 137
Gunther Christian Jegert
Modeling of Leakage Currents in High-κ Dielectrics
170 Seiten
ISBN 978-3-941650-37-4

Vol. 138
Shamsul Arafin
Electrically-Pumped GaSb-Based Vertical-Cavity Surface-Emitting Lasers
126 Seiten
ISBN 978-3-941650-38-1

Vol. 139
Norman Hauke
Enhanced spontaneous emission from silicon-based photonic crystal nanostructures
208 Seiten
ISBN 978-3-941650-39-8

Vol. 140
Christoph Schindler
Quantum spin transport in semiconductor nanostructures
175 Seiten
ISBN 978-3-941650-40-4

Vol. 141
Narayan Sircar
Group IV all-semiconductor spin-tronics: Materials aspects and optical spin selection rules
163 Seiten
ISBN 978-3-941650-41-1

Vol. 142
Alaa Abdellah
Scalable Thin-Film Manufacturing Technologies for Organic Electronics
162 Seiten
ISBN 978-3-941650-42-8

Vol. 143
Roland Dietmüller
Hybrid organic-inorganic heterojunctions for photovoltaic applications
179 Seiten
ISBN 978-3-941650-43-5

Vol. 144
Simon Hertenberger
Growth and Properties of In(Ga)As Nanowires on Silicon
152 Seiten
ISBN 978-3-941650-44-2

Vol. 145
Thomas Zabel
Study on silicon-germanium nanoislands as emitters for a monolithic silicon light source
152 Seiten
ISBN 978-3-941650-45-9

Vol. 146
Thomas Eißfeller
Theory of the Electronic Structure of Quantum Dots in External Fields
146 Seiten
ISBN 978-3-941650-46-6

Vol. 147
Simon Quartus Lud
Bio-Interfacing of Diamond Surfaces for the Study of Electrochemical Electron Transfer Kinetics
261 Seiten
ISBN 978-3-941650-47-3

Vol. 148
Florian Klotz
Spin effects in self-assembled semiconductor quantum dots
198 Seiten
ISBN 978-3-941650-48-0

Vol. 149
Vase S. Jovanov
Optically Probing Spin-Spin Interactions in Individual Quantum Dot Nanostructures
152 Seiten
ISBN 978-3-941650-49-7

Vol. 150
Carola Maria Oberhüttinger
Comparison of Different Ionisation Techniques for Ion Mobility Spectrometry
172 Seiten
ISBN 978-3-941650-50-3

Vol. 151
Felix Hoehne
Electrical Detection of Hyperfine Interactions in Silicon
181 Seiten
ISBN 978-3-941650-51-0

Vol. 152
Markus Raimar Dankerl
Electronic properties of electrolyte-gated diamond FETs for bioelectronic applications
201 Seiten
ISBN 978-3-941650-52-7

Vol. 153
Peter Greck
Efficient calculation of dissipative quantum transport in semiconductor nanostructures
149 Seiten
ISBN 978-3-941650-53-4

Vol. 154
John D. Howgate
GaN Heterostructures for Biosensing and Radiation Detection
160 Seiten
ISBN 978-3-941650-54-1

Vol. 155
Sabrina Niesar
Hybrid polymer/silicon nanocrystal solar cells
190 Seiten
ISBN 978-3-941650-55-8

Vol. 156
Tobias Walter Antesberger
Novel thin film concepts for photovoltaic applications
287 Seiten
ISBN 978-3-941650-56-5

Vol. 157
Thomas Andreas Wassner
Epitaxial growth and characterization of Zn(Mg)O thin films
225 Seiten
ISBN 978-3-941650-57-2

Vol. 158
Olaf Ulrich Wilhelm Weidemann
Interfaces in nitride devices
208 Seiten
ISBN 978-3-941650-58-9

Vol. 159
Matthias Firnkes
Electroosmotic Flow and Protein Trapping in Solid-State Nanopores
118 Seiten
ISBN 978-3-941650-59-6